SCALED MULTIVENT CHUGGING TEST PROGRAM
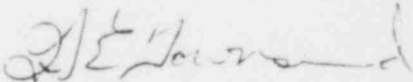
GENERAL ⬡ ELECTRIC

MARK II CONTAINMENT PROGRAM

SCALED MULTIVENT CHUGGING

TEST PROGRAM

Approved: _____
G.E. Wade, Acting Manager
Containment Design

Approved: _____
H. E. Towsend, Manager
Containment Technology

The information contained in Part A of this document was prepared for the Mark II Utility Owner's Group by Creare Inc., under contract with the General Electric Company.

GENERAL ⊛ ELECTRIC

DISCLAIMER OF RESPONSIBILITY

CONTENTS

CONTENTS (Continued)

TABLES

ILLUSTRATIONS

ILLUSTRATIONS (Continued)

ILLUSTRATIONS (Continued)

ILLUSTRATIONS (Continued)

ILLUSTRATIONS (Continued)

ILLUSTRATIONS (Continued)

PART A
SINGLE AND MULTIVENT TEST AND ANALYSIS

SUMMARY

This is the final Scaled Multivent Test Program report. In this test program
single and multivent tests were performed at several scales and over a wide
range of test conditions.

The objectives of the test program were:

a. Demonstrate that single cell chugging loads are bounding by establishing
   that multivent loads are less than single vent loads.

b. Determine the multivent effects that occur during chugging in multivent
   geometries.

c. Show that the multivent effects observed at subscale would also be
   expected to occur at full-scale.

In meeting these objectives tests were performed on single vent geometries at
four subscales and multivent geometries at two scales. The geometries tested
are summarized in Table S-1. Data from these tests were presented in earlier
data reports. In this report the data from previous tests in this program are
combined together with data from full-scale tests and theoretical analyses
to provide a unified description of chugging in single and multivent geometries
which fulfills the objectives of this program.

The five test vessels used ranged in size from 10-in to 44-in in diameter.
All geometries had the drywell-over-wetwell configuration of the Mark II plant
with straight vents. Critical dimensions such as submergence, clearance, vent
diameter, vent spacing and wetwell diameter were linearly scaled; while vent
lengths and the pool-to-vent area ratio were kept constant between geometries.
Special tests in this program, together with previous programs, provide data
on the effects of varying the dimensions. In this program chugging data

were obtained over a wide range of conditions (steam flux, air content, pressure, pool temperature) to contribute to the basic understanding of the physics of the phenomena and, hence, the effect of scale and the extension of the data to full-scale.

Extensive instrumentation, together with a 28 channel analog tape recorder and a 64 channel minicomputer-based data acquisition and reduction system, provided data on (1) pool interior and boundary pressures, (2) pool temperature distribution, (3) vent pressures, (4) water position and velocity in the vents, (5) vent, vessel and basemat accelerations, (6) and the various steady-state test conditions such as steam and air flow rates, system pressure and pool temperature and depth. Data reduction was accomplished by manually-guided computer manipulations.

The main result from the test data obtained in this program was that at test conditions representative of full scale the pool wall pressures in a multivent geometry are lower than those in the corresponding single vent geometry, i.e., single vent pool wall pressures are bounding.

The reduction in wall pressure amplitudes in a multivent geometry is due to the multivent effects where the chugs (bubble collapses) at individual vents are desynchronized and the chug strengths at individual vents varies in a multivent geometry. As expected, these multivent effects did occur in the full-scale JAERI multivent tests, therefore, the multivent pool wall pressure characteristics observed at subscale are also expected to occur at full-scale.

The single vent test data at four subscales along with full-scale single vent data show:

a. Under prototypical test conditions (full-scale values of the wetwall airspace pressure, steam mass flux, pool temperature and steam air content) the essential features of chugging are preserved between scales.

b. Chugging characteristics are dependent on system conditions and parameters such as average pool wall pressure amplitudes, and period between chugs show clear trends with system conditions that are similar at all scales, including full-scale.

The multivent test data show:

a. Multivent chugging characteristics are also dependent on system conditions and the trends of average pool wall pressure amplitudes and period between chugs with system conditions are virtually identical to those for single vent chugging.

b. Multivent pool wall pressure amplitudes are less than the corresponding single vent amplitudes.

c. The lower multivent pool wall pressures are principally due to the multivent effects where bubble collapses at individual vents are not synchronized and the strength of the bubble collapses varies from vent to vent for a given chug event in a multivent geometry. These multivent effects are observed in both subscale and full-scale (JAERI) multivent tests.

d. The multivent pool wall pressure characteristics can be predicted by acoustic analyses incorporating the observed multivent effects.

Test data gathered during this test program provide for supporting the Mark II Chugging Loads Methodology which uses full-scale single vent data to predict the Mark II chugging loads.

Table S-1

SCALED MULTIVENT TEST PROGRAM

Single Vent Test Geometries   1/10, 1/6, 1/4, 5/12 scales

Multivent Test Geometries   1/10 scale, 3, 7, 19 vents
                                       1/6 scale, 3, 7 vents

Additional Test Geometries   Effect of drywell volume
                                         Effect of pool size
                                         Effect of vent location in the pool
                                         Effect of vent length

Total Number of Test Geometries = 19

Total Number of Tests = 749

A1. INTRODUCTION

This is the final report for the Scaled Multivent Test Program. The Scaled Multivent Test Program has generated a significant data base on chugging in single and multiple vent geometries. These data have provided the trend in chugging loads with number of vents and physical insights into the chugging phenomenon in single and multivent geometries. The data base was reported on in two earlier data reports [References A1 and A2]. This final report combines and explains the data trends reported in the two earlier data reports together with data from full-scale single and multivent tests [References A3, A4, A5 and A6].

A1.1 BACKGROUND

After the initial pool swell transient from a postulated LOCA in a BWR steam with decreasing amounts of air is vented from the drywell into the wetwell of the Pressure Suppression System. The purpose of this venting is to condense the steam in the wetwell pool and limit the pressure buildup in the containment. During such steam venting condensation-driven oscillations have been observed in various experiments.

Two types of condensation-driven oscillations have been observed. The first type, called "condensation oscillation (CO), occur during the earlier portion of the blowdown. CO is characterized by fairly sinusoidal pressure oscillations in the entire drywell, vent and wetwell system. These condensation oscillations are followed by the second type of condensation-driven oscillations called "chugging". Chugging is characterized by discrete bursts of pressure oscillations in the wetwell pool with quiescent periods between them. The pressure oscillations during chugging are associated with the rapid collapse of the steam "bubble" at the vent exit and typically exhibit a pressure spike followed by a damped ringout which has predominant frequency components at the vent and pool natural frequencies.

The characterization of these condensation-driven pressure oscillations for Mark II plant structural evaluations has been the major thrust of the CO and Chugging Load Definition Programs. The full-scale single cell tests (single vent in an appropriate sized pool) [References A3, A4 and A5] provide the data base from which the Mark II CO and chugging load definitions will be developed. Since the Mark II Suppression System is a multivent geometry, it is necessary to demonstrate that the full-scale single vent data will conservatively bound the loads expected in the multivent Mark II geometry. The Scaled Multivent Test Program was performed to provide experimental configuration of the bounding nature of the single cell loads.

A1.2 TEST PROGRAM OVERVIEW

The detailed program plan and description of the Scaled Multivent Test Program are given in References A8 and A9 and briefly summarized here.

The main objectives of the Scaled Multivent Test Program were to determine multivent effects on chugging (such as trends in pool wall pressure magnitudes with number of vents), demonstrate that the multivent trends observed at sub-scale remain valid at full-scale, and provide a data base for assessment of analytical load application techniques.

These test objectives were met by including tests in single vent geometries at four scales (1/10, 1/6, 1/4 and 5/12 scale), and multivent geometries at two scales (3, 7, and 19 vents at 1/10 scale and 3 and 7 vents at 1/6 scale). Special tests were included to determine the effects of drywell volume, pool size and vent location in the pool. The testing was divided into two phases as shown in Figure A1-1.

Phase 1 included the design and construction of the test facility, the instrumentation, and the data acquisition and reduction hardware and software. After a shakedown of the complete facility, including instrumentation, data acquisition and reduction systems, tests were performed on the 14 Phase 1 geometries. Five of these geometries provided the Phase 1 portion of the baseline single and multivent test data. These five geometries included the

1, 3 and 7 vent configurations at 1/10 scale, and 1 and 3 vent configurations at 1/6 scale. The remaining geometries tested in Phase 1 provided data on the effects of drywell volume, pool size and vent location in the pool.

In Phase 2 an additional test vessel was installed in the test facility and five single and multiple vent geometries were tested. These tests included two more single vent geometries at 1/4 and 5/12 scale, a single vent geometry at 5/12 scale with an increased vent length, and two additional multivent geometries (19 vents at 1/10 scale and 7 vents at 1/6 scale). The test matrices for Phase 1 and Phase 2 covered a wide range of test parameters such as steam mass flux, pool temperature, steam air-content, and wetwell airspace pressure.

```
┌─────────────────────────────────────┐
│ ● Design & Construct Facility        │
│ ● Develop Instrumentation,           │
│   Data Acquisition & Reduction       │
│   Procedures                         │
└─────────────────────────────────────┘
                    │
                    ▼
┌─────────────────────────────────────┐        ┌──────────────────┐
│          PHASE 1 TESTS               │        │ INTERIM PHASE 1  │
│                                      │───────▶│ TEST REPORT      │
│ 14 Test Geometries:                  │        └──────────────────┘
│     1/10 scale - 1, 3, 7 Vents       │
│     1/6  scale - 1, 3  Vents         │
│   Variation of Drywell Size,         │
│   Pool Size & Vent Location          │
│   in the Pool                        │
│ Total Number of Tests = 452          │
└─────────────────────────────────────┘
                    │
                    ▼
┌─────────────────────────────────────┐        ┌──────────────────┐
│          PHASE 2 TESTS               │        │ INTERIM PHASE 2  │
│                                      │───────▶│ DATA REPORT      │
│ 5 Test Geometries:                   │        └──────────────────┘
│   1/4 scale - 1 Vent                 │
│   5/12 scale - 1 Vent (two           │
│   Vent Lengths)                      │
│   1/10 scale - 19 Vents              │
│   1/6 scale - 7 Vents                │
│ Total Number of Tests = 297          │
└─────────────────────────────────────┘
                    │
                    ▼
┌─────────────────────────────────────┐
│          FINAL REPORT                │
└─────────────────────────────────────┘
```

Phase 1 ← (brackets Phase 1 section)
Phase 2 ← (brackets Phase 2 section)

Figure A1-1. Scaled Multivent Test Program Overview

A2. TEST DESCRIPTION

This section includes a brief description of the test facility, instrumentation, data acquisition and reduction procedures. A detailed discussion is given in References A1 and A2.

A2.1 TEST FACILITY

The Scaled Multivent Test Facility is shown schematically in Figure A2-1, including a steam supply, a water supply system, an air supply system, and the five test vessels used for the single and multiple vent geometries.

Steam was provided by a 20,000 lb/hr 200 psi boiler with a full flow discharge pressure regulator and flow control valves. The steam flow rate into the drywell was measured by standard orifice meters with three meters for each test geometry to insure adequate coverage of the wide range of flows required in the test matrix. A constant steam flow was maintained independent of drywell pressure fluctuations by using a choked valve at the steam inlet to the drywell.

Cooling water was circulated through the vessel under test to maintain the desired pool temperature and vent submergence. The cooling water was pumped into the pool bottom through a distribution header and drawn out of the pool approximately 3-inches below the pool surface.

Air was provided for pressurizing the test vessels, and mixing with steam in the drywells to provide the desired steam air-content. The flow rate of air delivered to the drywell was measured with turbine meters, with three meters available to cover the full range required. The air flow rate was maintained constant independent of drywell pressure fluctuations by using a choked flow control valve at the inlet to the drywell.

A2.2 INSTRUMENTATION

The Scaled Multivent Test Facility was provided with sufficient instruments
to obtain the measurements required to meet the objectives of the test program.
These measurements were classified in two main categories, prinicpal and system.
The principal data consisted of pool wall pressures, "source" pressures, pool
temperatures, wall and vent accelerations, vent static pressure, and vent water
level. In addition to pool pressures and temperature distributions, these data
were used to determine the phasing between vents and other information to assist
in understanding chigging and multivent effects. The system data were data
needed to establish the test conditions such as steam and air flow rates to the
drywell, drywell pressures and temperatures, vent submergence, and wetwell
freespace pressure and temperature. A schematic diagram of the measurement
locations is given in Figure A2-2. The instrument specifications are given in
Table A2-1, including a cross-reference to Figure A2-2.

The detailed locations of the various instruments for a given test geometry
are given in References A1 and A2.

A2.3 DATA ACQUISITION SYSTEM AND PROCEDURES

The data acquisition system used for recording the test data is shown in
Figure A2-3. The signals from the various instruments were conditioned and
amplified to give a ±5 volt full-scale output. The slow response transducer
signals were routed directly via a 64-channel multiplexer to the A/D converter.
The fast response transducers were recorded on a 28-channel FM tape recorder.
The reproduce side of the tape recorder was connected to the multiplexer and
an oscillograph. The oscillograph output was used for visual monitoring on
the data being recorded on the FM tape recorder.

The signals from the A/D converter were fed via a microcomputer (DEC LPA11)
to a PDP 11/70 minicomputer. Once the data were on the PDP 11/70 they could
then be manipulated and displayed on both video and hardcopy terminals. The
low response transducer signals were digitized at a rate of 15 Hz in real
time, i.e., during the actual test. Key test parameters such as steam mass

flux, pool temperature, steam air-content, etc., were processed on-line during the test and displayed in engineering units at the data acquisition station. This allowed real time monitoring of the key test parameters. At the start of a typical test the test operator input the required test conditions using an analog panel display of the test conditions. The actual test conditions set were monitored using the above mentioned real time monitoring capability of the data acquisition system. After the test parameters were adjusted within specified tolerances the test was initiated.

At the start of the test, a calibration sequence was followed which, starting from zero volts, input a set of known voltages into the signal conditioning/ amplifier systems (input at the same point as the raw transducer signal). Based on this sequence the computer automatically obtained the zero offsets and gains of all the channels and flagged out any malfunctioning channels. After completing the calibration sequence test data were recorded for a duration of about 100 seconds. As explained earlier, the slow response signals were digitized and input directly to the PDP 11/70, whereas the fast response channels were recorded on the FM tape recorder. Selected fast response channels were also digitized in real time from the output side of the tape recorder. On completing data recording the time plots and mean values of the key test parameters were produced for the duration of the test. Time plots of the selected fast response channels were also produced to aid in data checking.

A2.4 DATA REDUCTION

As described previously, the signals from the slow response channels were digitized and input to the PDP 11/70 minicomputer in real time during each test. These channels were digitized at a rate of 15 Hz per channel. This digitization rate was used because the frequency response of all the slow response channels was less than 5 Hz. The data from these slow response channels, which consisted mainly of pool temperatures and system data, were reduced to engineering units and the average values over the test duration were stored for data plotting and display purposes.

The fast response channels, recorded on the FM analog tape recorder, were digitized at a convenient time after the test. The digitization rate for these fast response channels was 10,000 Hz per channel. The fast response data were then reduced to give pool wall pressure statistics and vent phasing (for 3-vent multivent geometries only). The data reduction procedures used for obtaining these are described below.

The pool wall pressure data were reduced to obtain statistics from the peak overpressures (POP), peak underpressures (PUP), and the period between chugs (t_p). A simple algorithm was developed to detect chugs and obtain the POP, PUP and the time at which the POP occurred for each chug. From these, the mean values and standard deviations for POP, PUP and t_p (time interval between successive POPs) were computed.

In addition to the pool wall pressure amplitude statistics, vent phasing information was also obtained for the 1/10 and 1/6 scale 3 vent geometries (since only a maximum of three vents were completely instrumented in a given multivent geometry, complete information for determination of phasing was available for the 3 vent geometries only). The phasing information obtained for a given "pool chug" (identified by an oscillation in the pool wall pressure) in the three vent geometries included:

a. The number of vents at which steam bubble collapses occurred, i.e., the number of vents that chugged.

b. The times when the individual vents chugged.

These data provide statistical information such as the probability of a given number of vents chugging and the mean delay time between chugs at individual vents during a pool chug for a given test condition.

Vent phasing was determined by instrumenting individual vents in the 1/10 scale and 1/6 scale three vent geometries with a vent static pressure transducer, coupled conductivity probes, and an accelerometer mounted on the vent near

the vent exit. After examinating a large amount of data the vent static pressure was found to be the best indicator for the occurrence of a chug at a vent.

The pool wall pressure, vent static pressure and vent water level traces for the different types of chugs in the single vent geometry will be discussed below to illustrate the interrelationship between these traces and how these were used to determine phasing in the multivent geometry.

Figure A2-4 shows the wall pressure and vent static pressure traces and the vent water level trace for a "classical" chug in a single vent geometry. At the start of the chug the vent is dry and both the pool wall and vent static pressures decrease. This is caused by the rapid condensation occurring at the vent exit which both reduces the pressure in the steam bubble and induces an increased steam flow in the vent which reduces the vent static pressure. The bubble collapse produces the spike in the wall pressure trace. A rapid reduction in the condensation rate at the vent exit causes a positive pressure wave to propagate up the vent which in turn causes the vent static pressure to increase. As a result both the pool and vent vibrate at their respective natural frequencies. Due to the impedance mismatch at the steam water inter- face the vent vibrates at its natural frequency whereas the pool wall pressure frequency contains components from both the pool and vent (ringout). Instru- mentation measuring the vent static pressure showed the minimum preceding the maximum in the vent static pressure to occur at about the same time as the positive pressure spike in the pool wall.

The second type of chugs observed is illustrated in Figure A2-5. In these chugs ("oscillatory" chugs) the pool wall pressure shows periodic pressure oscillations at the same frequency as the oscillations in the vent static pressure. Generally, the vent pressure oscillations for the oscillatory type chugs are smaller in magnitude than those for the classic chugs. Also, for the oscillatory chug no clear spike is observed in the wall pressure traces.

Other types of chugs observed are combinations of the classic and oscillatory chugs as shown in Figure A2-6 where an oscillatory chug precedes the classical chug. In general, all chugs observed could be placed in one of the three categories described (classical, oscillatory, or a combination of the two). However, in a few tests with the highest steam mass flux of 16 lbm/sec-ft^2 and non-zero steam air-content bursts of periodic pressure oscillations were found to occur which fit in neither of these three categories.

An examination of a large amount of multivent data showed the chugs occurring at each individual vent in a multivent geometry have similar characteristics as those in a single vent geometry. That is classical chugs, oscillatory chugs and their combinations occur at individual vents, except the ones at 16 lb/sec ft^2 and non-zero air-content. Based on these observations, a phasing algorithm was developed as described in the following discussion.

The occurrence of a "pool" chug was detected by using the chug finder on the wall bottom pressure trace. The times at which pool chugs occurred were input to the phasing algorithm. A time window was then defined around the POP for the pool chug which was sufficiently wide so as to encompass the duration of the pressure oscillations for that "pool" chug.

Within the time window for the pool chug, the phasing algorithm scanned the individual vent static pressures to determine if a positive excursion from the mean occurred which exceeded an operator-set threshold. If such an excursion was found the algorithm then located the preceding minimum in the vent static pressure. Next, the water level probes in that vent were checked to determine if there was any water in the vent. If the water level was below a preset level (generally 1-in) a classical chug was said to have occurred at that vent. The time of the pressure minimum was then taken to be the time at which the chug occurred at that vent.

After the vents that had classical chugs were identified the other vents were examined for an oscillatory type chug. The vent static pressures and vent water levels for these vents were examined in a time window of 0.025 seconds following the time of occurrence of the first chug found in the pool chug.

This 0.025 second window is slightly greater than the period for the vent quarter wave mode (which was less than 0.020 seconds for the vent lengths used). In this time window, if a vent was found to be dry and its static pressure amplitude greater than a second operator-specified threshold, an oscillatory type chug was presumed to have occurred at that vent. This second vent static pressure threshold was lower than that used for detecting classical chugs since the magnitude of the pressure oscillations for the oscillatory chugs were smaller than those for the classical chugs. The time of the vent static pressure minimum was taken to be the time of occurrence of the oscillatory chug.

If none of the three vents* were found to have a large positive excursion in the vent static pressure, the phasing algorithm went on to the next pool chug. This means that phasing was determined only for those pool chugs where a classical chug or a combination (classical and oscillatory) chug occurred at one or more vents.

The two threshold values for the vent static pressure mentioned above were set by the operator to give the most reliable phasing data for a given test run. The quality of these thresholds was determined by comparison with visual phasing determination for the first 20 pool chugs in the test.

The phasing algorithm was run on the first 100 pool chugs detected in the test. In each pool chug the algorithm determined the number of vents that chugged and the time of occurrence of these chugs at the individual vents. The percentages of pool chugs with one, two or all three vents chugging were computed from these phasing outputs for individual pool chugs. The mean time delay (the time between the first and the last vent to chug in a pool chug) and its standard deviation were also computed. These phasing data were obtained for the 45 psia wetwell airspace pressure tests only. The vent static pressure variations at the lower wetwell airspace pressure were not large enough for adequate phasing determination.

---

*Phasing was determined from the three vent geometries only.

It was recognized from the outset of this test program that determination of
phasing would be difficult. Although the phasing algorithm performed ade-
quately, it was able to determine phasing for about 70 to 80 percent of the
pool chugs.

Besides the pool wall pressure amplitude statistics and phasing, other data
reduction involved obtaining condensation rates from drywell pressure data
and PSDs of pool wall pressure traces. The procedure used for obtaining the
condensation rates will be discussed in Section A4. PSDs were obtained using
standard Fast Fourier Transform (FFT) analyses.

Table A2-1
INSTRUMENT LIST

Designator	Measured Parameter	Instrument Type	Instrument Calibration Accuracy	Total Measurement Accuracy	Rise Time	Tolerances On Set Conditions
P1	Steam Supply Pressure	Pressure Gauge and Transducer	±0.5 psi	±1.0 psi	--	--
P2	Orifice Meter Differential Pressure	Differential Pressure Transducer	±0.5" H_2O	±0.6" H_2O		
T1	Steam Supply Temperature	Thermocouple	±2°F	±4°F		
F1	Steam Flow	Orifice Meter	±2%	±6%	--	±10%
P3	Air Supply Pressure	Pressure Gauge and Transducer	0.5 psi	±1.0 psi	--	--
T2	Air Supply Temperature	Thermocouple	±2°F	±4°F	--	--
F2	Airflow	Turbine Meters	±5%	±10%	--	±10%
P4	Drywell Average Pressure	Pressure Gauge and Transducer	±0.5 psi	±3 psi	--	--
P5	Drywell Instantaneous Pressure	Pressure Transducer	±0.5 psi	±1 psi	<2 msec	--
P6	Wetwell Airspace Pressure	Pressure Gauge and Transducer	±0.5 psi	±1 psi	--	±2 psi
P7-12	Pool Wall Pressure	Pressure Transducer	±0.5 psi	±1 psi	<50μ sec	--
P13-15	"Source" Pressure	Pressure Transducer	±0.5 psi	±1 psi	<50μ sec	--
P16-18	Vent Static Pressures	Pressure Transducer	±0.5 psi	±1 psi	<50u sec	--
T3	Drywell Temperature	Thermocouple	±4°F	±8°F	<10 sec	--
T4	Wetwell Airspace Temperature	Thermocouple	±4°F	±10°F	<10 sec	--
T5-16	Pool Temperatures	Thermocouple	±4°F	±8°F	<1 sec	±15°F
C1-3	Vent Water Level	Coupled Cond. Probes (24 per vent)	--	±4"	<2 msec	--
L1	Wetwell Water Level	Differential Pressure Transducer	±1.5" H_2O	±3"	--	±3" Average
A1	Pool Wall Acceleration	Accelerometer	±5%	±10%	**	--
A2	Basemat Acceleration	Accelerometer	±5%	±10%	**	--
A3-5	Vent Accelerometer	Accelerometer	±5%	±10%	**	--

*See Figure 2-6.
**Frequency response of 5 kHz.
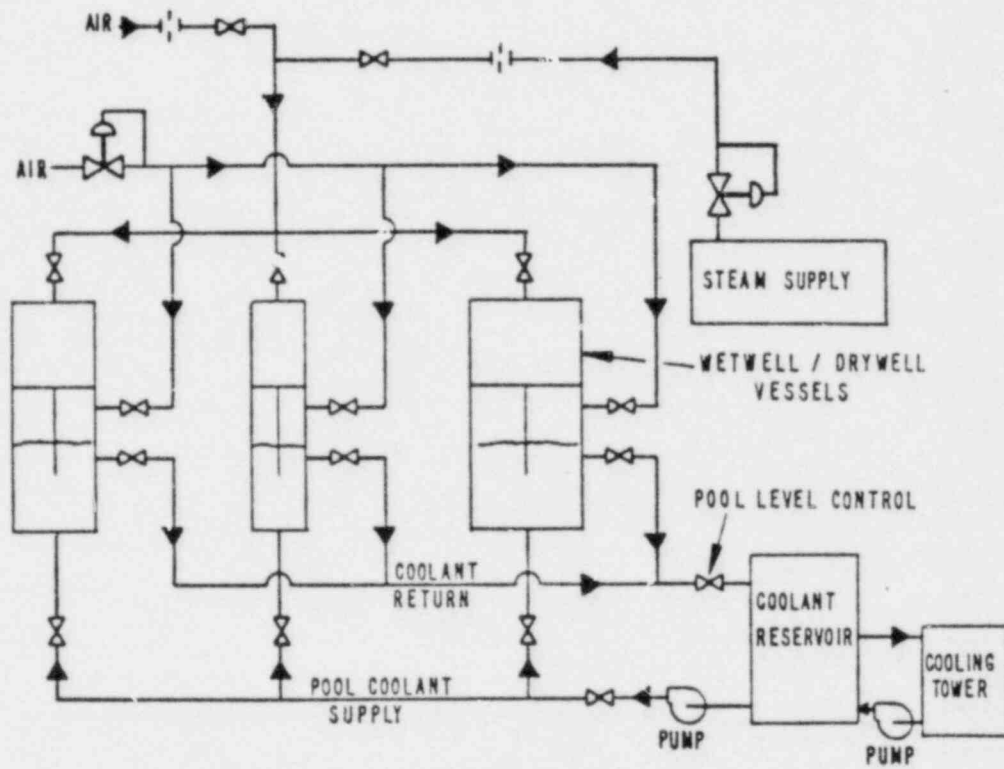
Figure A2-1. Schematic of the Scaled Multivent Test Facility
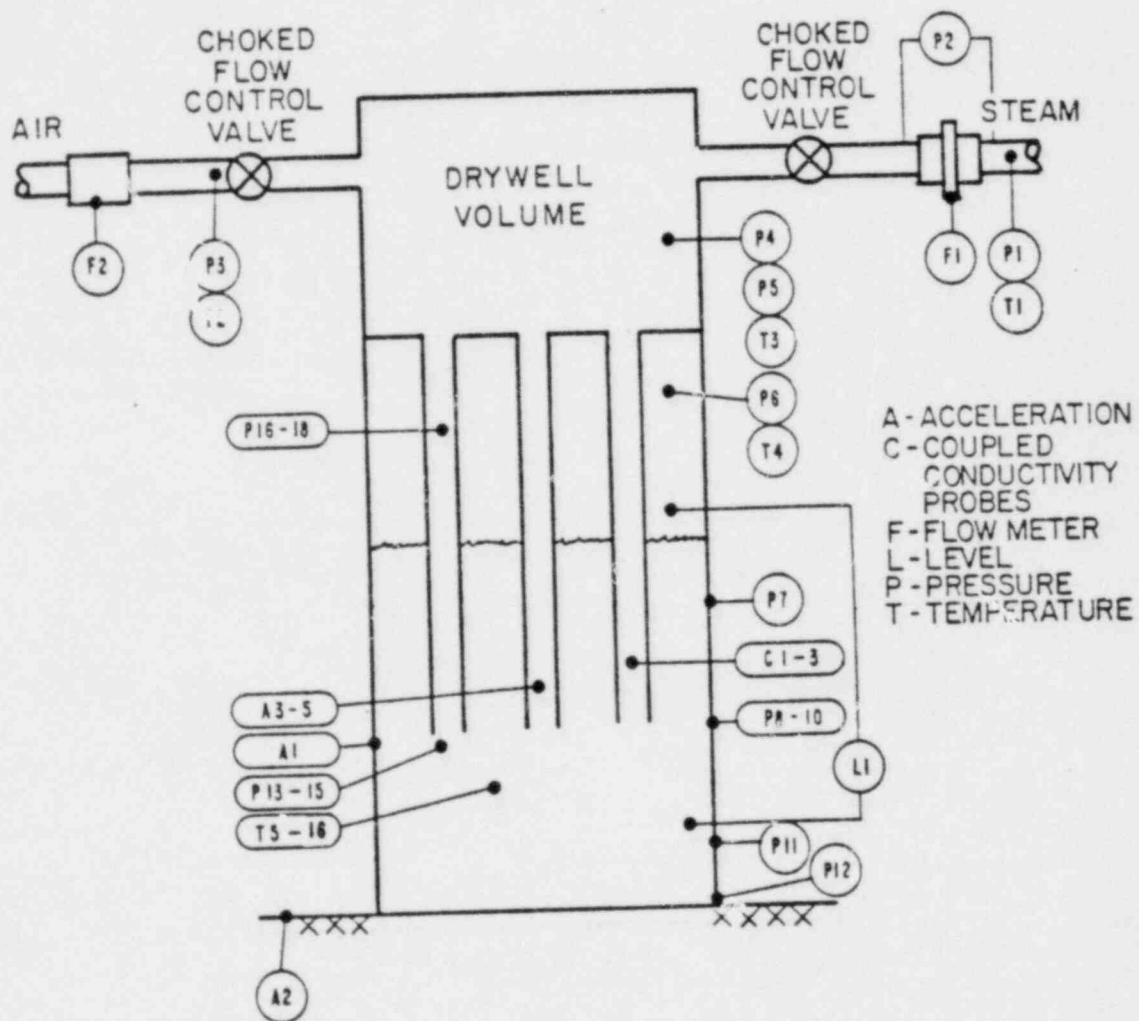
Figure A2-2. Schematic of Instrument Locations
(Keyed with Table 2-4)
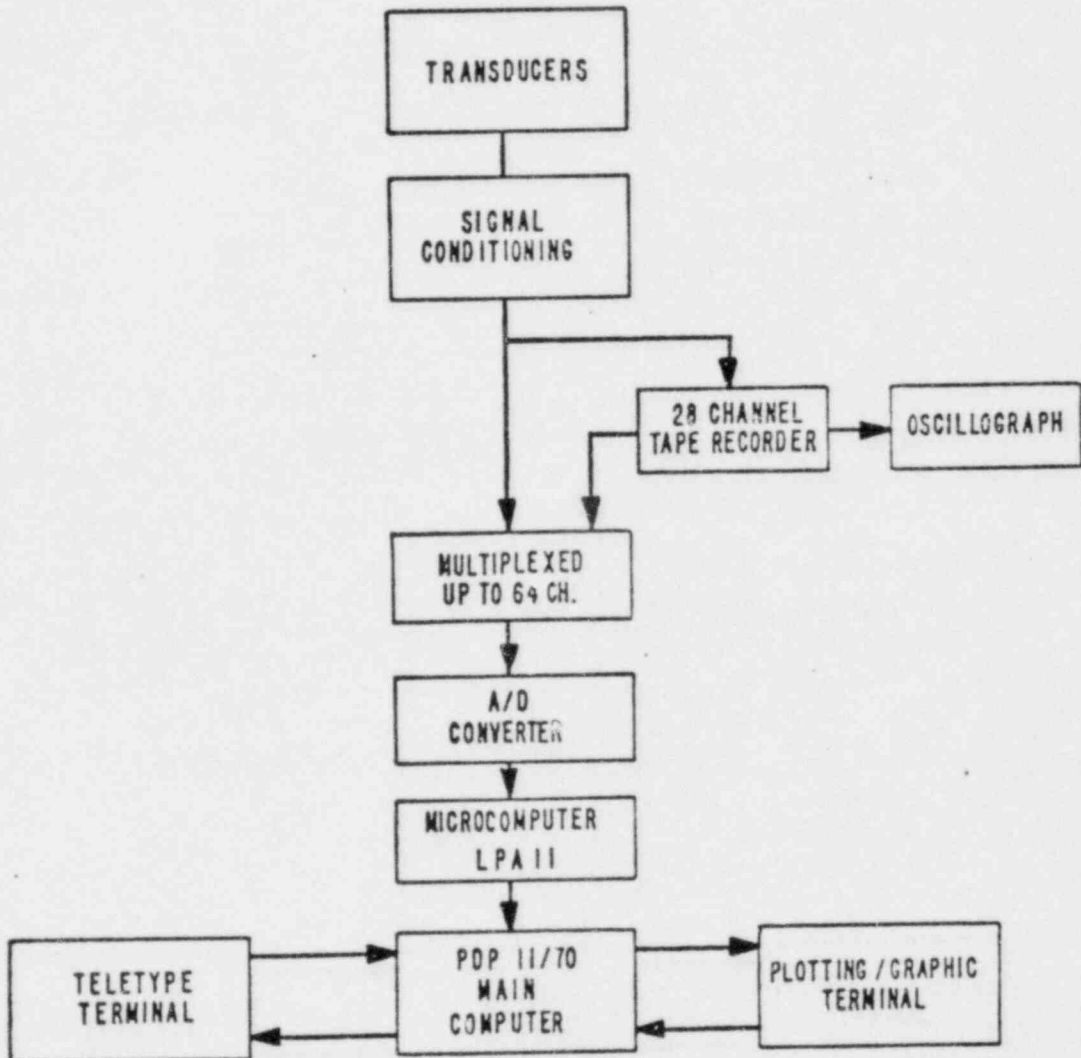
Figure A2-3. Schematic of the Data Acquisition System

The following Figures are General Electric Company Proprietary
and have been removed from this document in their entirety.

A2-4   A Classical Chug in a Single Vent Geometry

A2-5   An Oscillatory Chug in a Single Vent Geometry

A2-6   A Combination Chug - An Oscillatory Chug Preceding a
        Classical Chug - in a Single Vent Geometry

A3. TEST GEOMETRIES AND TEST MATRIX

The single and multivent geometries tested in Phases 1 and 2 of the Scaled
Multivent Test program will be discussed in this section along with the test
matrices used.

A3.1 TEST GEOMETRIES

The scaled geometries tested in this test program are shown in Tables A3-1
along with the as-built critical dimensions. The two scaling schemes consi-
dered in the beginning of this test program (Reference B8) will be discussed
in Subsection A3.2 and Section A4. Both of these scaling schemes required
that all dimensions in a subscale geometry be scaled by the factor which is
defined as the ratio of the scaled vent diameter to the proptotypical vent
diameter. Table A3-2 shows the dimensions of the Reference Mark II contain-
ment from which the test geometries listed in Table A3-1 were scaled.
Specifically, the vent submergence and clearance were scaled linearly. The
drywell volume was scaled down by the cube of the scale factor and the pool
to vent area ratio was preserved at the prototypical value, except for
geometries where it was deliberately varied. Vent lengths were set at approx-
imately 9-ft for all configurations regardless of scale. This length provided
the best match to the requirement for multiple use of several test vessels.
All the test geometries had the drywell mounted on top of the wetwell similar
to the Mark II drywell/wetwell configuration.

The five baseline geometries having 1, 3, 7 and 19 vents at 1/10 scale and
1, 3, and 7 vents at 1/6 scale are shown schematically in Figures A3-1 and
A3-2. The layout of the multiple vents in the wetwell pools was designed
to produce the following features:

a. Constant vent-to-vent spacing for all configurations at a single scale.

b. Constant vent-to-wall spacing at same locations on the wall.

c. Constant pool-to-vent area ratios.

Figures A3-3 and A3-4 show the single and multiple vent layouts at 1/10 and 1/6 scales.

The type of data comparisons that can be made using the test data from the various test geometries are given in Table A3-3. Geometries A, K, P and U provided the baseline 1/10 scale 1, 3, 7 and 19 vent data; geometries J, M and V the baseline 1/6 scale 1, 3, and 7 vent data. The baseline single vent data at four subscales - 1/10, 1/6, 1/4 and 5/12 - are provided by geometries A, J, T and S respectively. Geometries R and S gave the effect of vent length on chugging. Drywell volume effect on single vent chugging was obtained in geometries B, C, and D. Geometries L and N provided the effect of oversized drywell volume on multivent chugging. The data on the effect of pool size and vent location in the pool were obtained in geometries A, B, C, D, E, F, G, and H. These data are used to determine the dynamics of the chug induced pressure waves in the pool and help in understanding the multivent data.

A3.2 TEST MATRIX

The test matrices are shown in Table A3-4. As shown in Table A3-1, the type I test matrix was used for the baseline test geometries. Type II test matrix was used for the remaining geometries.

The test conditions were chosen based on the requirements of the two scaling schemes (Reference A8) that were postulated - Froude and Mach scaling. These two scaling schemes result from choosing different sets of parameters to non-dimensionalize the system of equations governing the motion of the steam and water during chugging and are discussed further in Section A4.

In the Froude scaling scheme the impetus is to preserve the bubble growth and pool dynamics due to the motion of the steam/water interface in and out of the vent. Froude scaling has been used quite successfully in the scaling of pool

swell experiments (References A10 and A11). The main requirements that result from this scaling scheme are:

a. System pressure reduced by S.
b. Steam mass fluxes reduced by $S^{3/2}$.
c. All dimensions linearly scaled by S.

S is the scale factor defined as the ratio of the scaled vent diameter to the full scale vent diameter. The main shortcoming with the Froude scaling scheme is that the thermodynamic parameters affecting condensation cannot be preserved.

The Mach scaling scheme on the other hand attempts to preserve the condensation process. The condensation phenomenon is mainly governed by the thermodynamic properties (such as subcooling, enthalpies, etc.) of both the liquid and vapor phases. Therefore, the Mach scaling scheme preserves these thermodynamic parameters between scales. The main requirements of this scaling scheme are:

a. Prototypical system pressures.
b. Prototypical steam mass fluxes.
c. Prototypical pool temperatures.
d. All dimensions scaled linearly by S.

The test matrices chosen reflect the requirements of the two scaling schemes with tests at reduced wetwell airspace pressure corresponding to Froude S ling, and those at prototypical wetwell airspace pressure (45 psia) corresponding to Mach scaling. Several tests were added at atmospheric wetwell airspace pressure to bridge the gap between the Froude scaled and Mach scaled test conditions.

The important point here is that no single scaling scheme will satisfy all aspects of the chugging phenomenon. Therefore, the test matrices chosen were made sufficiently broad so as to cover a wide range of test conditions. This feature combined with the single vent tests performed over a wide range of scales in the Scaled Multivent Test Program has provided sufficient data to evaluate the effects of scale on the chugging phenomenon and demonstrate the applicability of the subscale multivent effects to full-scale.

Table 3-1

SCALED MULTIVENT TEST PROGRAM
TEST GEOMETRIES

Geometry Code	Geometry Number	Vent Diameter (in.)	Scale	Number of Vents	Vent Length (ft)	Wetwell Diameter (in.)	Drywell Volume (ft^3)	Vent Clearance (in.)	Vent Submergence (in.)	Vent Offset (in.)	Pool To Vent Area Ratio	Test Matrix Type*
A	1	2.32	1/10	1	9.47	10.02	2.5	14	14	0	18.6	I
B	2	2.32	1/10	1	9.47	17.25	2.5	14	14	0	55.3	II
C	3	2.32	1/10	1	9.47	17.25	7.3	14	14	0	55.3	II
D	4	2.32	1/10	1	9.47	17.25	32	14	14	0	55.3	II
E	5	2.32	1/10	1	9.47	17.25	2.5	14	14	4	55.3	II
F	6	2.32	1/10	1	9.47	29.25	2.5	14	14	0	159	II
G	7	2.32	1/10	1	9.47	29.25	2.5	14	14	6	159	II
H	8	2.32	1/10	1	9.47	29.25	2.5	14	14	10	159	II
J	9	3.83	1/6	1	8.72	17.25	11	23	23	0	20.3	I
K	10	2.32	1/10	3	9.47	17.25	7.3	14	14	0	18.4	I
L	11	2.32	1/10	3	9.47	17.25	32	14	14	0	18.4	II
M	12	3.83	1/6	3	8.72	29.25	33	23	23	0	19.5	I
N	13	3.83	1/6	3	8.72	29.25	93	23	23	0	19.5	I
P	14	2.32	1/10	7	9.47	27.25	17.3	14	14	0	19.6	I
R	15	10.02	5/12	1	17	44	190	60	60	0	19.3	I
S	16	10.02	5/12	1	9.7	44	195	60	60	0	19.3	I
T	17	6.06	1/4	1	9.0	27.25	41.5	36	36	0	20.2	I
U	18	2.32	1/10	19	9.5	44	46.5	14	14	0	18.9	I
V	19	3.83	1/6	7	8.7	44	77	23	23	0	18.9	I

*See Section 3.2

Table A3-2

PROTOTYPICAL MARK II CONTAINMENT GEOMETRY PARAMETERS

Parameter	Reference Dimension
Vent Diameter	24 in.
Vent Length	42 ft
Drywell Volume	2655 ft^3/vent
Vent Clearance	12 ft
Vent Submergence	12 ft
Pool to Vent Area Ratio	19.5

Table A3-3

SV/MV DATA COMPARISONS

Geometries*	Purpose
A, K, P, U	Baseline 1/10 scale single vent/multivent data
J, M, V	Baseline 1/6 scale single vent/multivent data
A, J, T, S	Single vent data at four scales
R, S	Effect of vent length
B, C, D	Effect of drywell volume on single vent chugging (larger drywell volumes used correspond to those used in MV tests)
L, N	Effect of oversized drywell volume on multivent chugging
A, B, F	Effects of pool size (centered vent)
B, E	Effect of vent location in 18-in pool
F, G, H	Effect of vent location in 30-in pool
A, E, H	Effect of pool size with vent located at the same distance (5-in) from the 0° circumferential wall location
B, G	Effect of pool size with the vent located at the same distance (9-in) from the 0° circumferential wall location

_____

*See Table A3.1.

Table A3-4a

TYPE I TEST MATRIX
GEOMETRIES* 1, 9, 10, 12, 14, 15, 16, 17, 18, 19*

Pressure (psia)	Froude Scaled[+]		14.7	45	
Steam Mass Flux (1bm/sec-ft^2)	0.1, 0.2 0.5, 1, 2	0.1, 0.5, 2	0.2, 1, 4	0.5, 1, 2, 4, 8, 10**, 16***	1, 4, 10**, 16***
Air Content (%)	0	0.1, 0.2, 0.5	0	0	0.1, 0.2, 0.5
Temperature (°F)	90, 130	90	90, 130	90, 130, 160, 200	130
Number of Tests	100	90	60	244	93

Total Number of Type I Tests: 587

[+] Froude scaled pressure is obtained by multiplying the full-scale pressure (45 psia) by the scale factor.

*See Table A3-1 for description of test geometries.

**Steam mass flux of 10 1bm/sec-ft^2 for Geometries 15, 16, 17, 18, 19.

***Steam mass flux of 16 1bm/sec-ft^2 for Geometries 1, 9, 10, 12, 14, 17.

Table 3-4b

TYPE II TEST MATRIX
GEOMETRIES 2, 3, 4, 5, 6, 7, 8, 11, 13*

Wetwell Airspace Pressure (psia)	Froude Scaled[+]	45
Steam Mass Flux (1bm/sec-ft^2)	0.2, 0.5, 1	0.5, 1, 2, 4, 8, 16
Air Content (%)	0	0
Temperature (°F)	90, 130	130, 160
Number of Tests	6	12

Total Number of Type II Tests: 162

[+] Froude scaled pressure is obtained by multiplying the full-scale pressure (45 psia) by the scale factor.

*See Table A3-1 for description of test geometries.
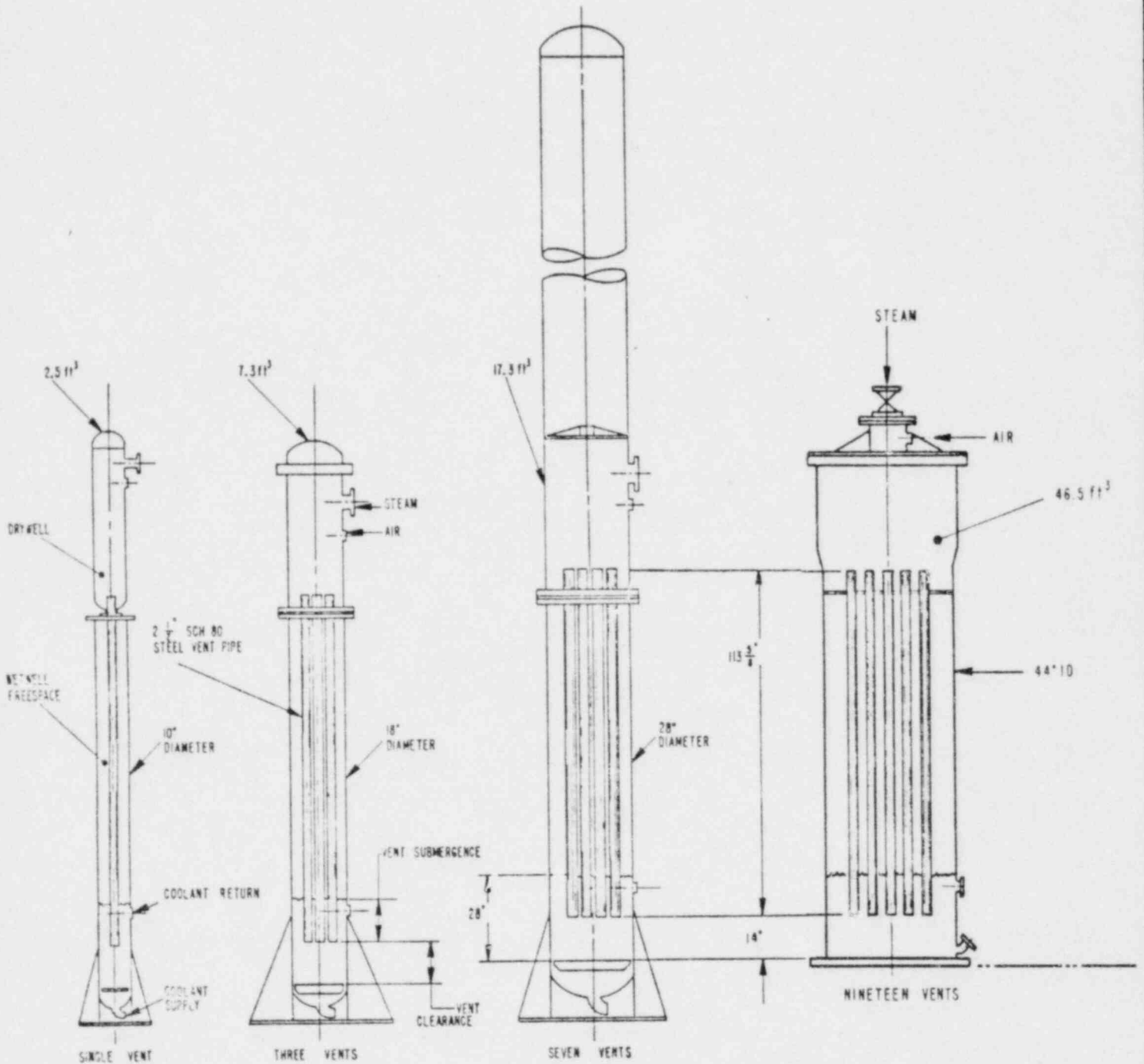
Figure A3-1.   Scaled Multivent Test Program 1/10 Scale Baseline Geometries
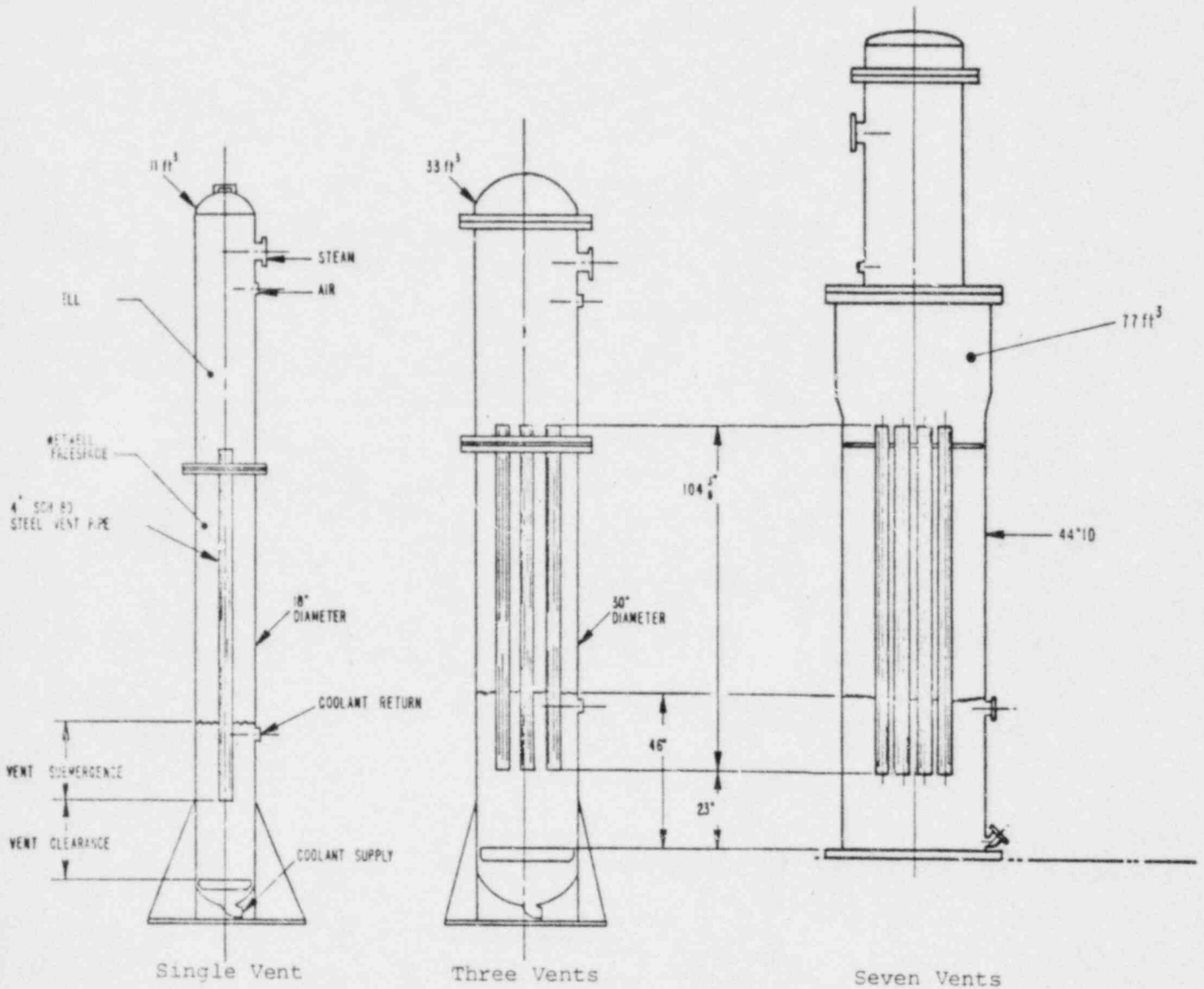
Figure A3-2.   Scaled Multivent Test Program 1/6 Scale Baseline Geometries
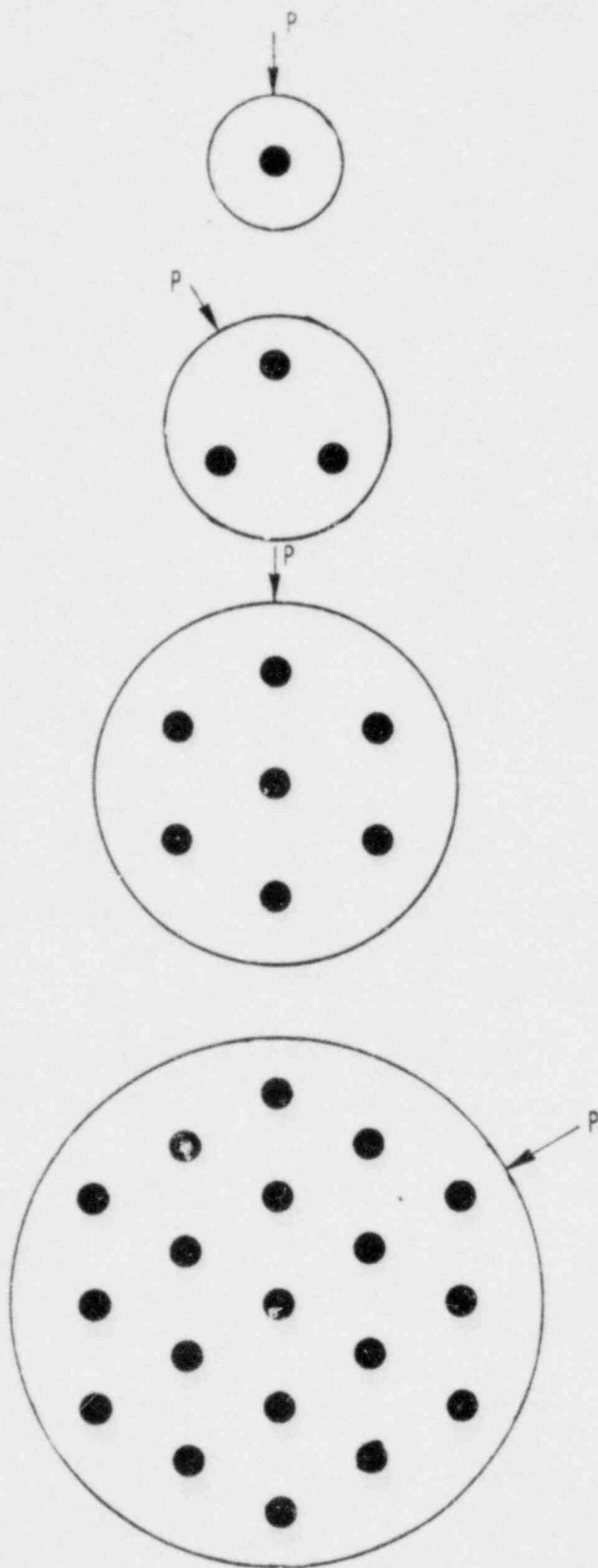
DIMENSIONS	NO OF VENTS			
	1	3	7	19
VENT DIAMETER	2.32"	2.32"	2.32"	2.32"
POOL DIAMETER	10.02"	17.25"	27.25"	44"
POOL TO VENT AREA RATIO	18.6	18.4	19.6	18.9

"P" DESIGNATES TYPICAL WALL PRESSURE
TRANSDUCER LOCATIONS

Figure A3-3.   Scaled Multivent Test Program 1/10 Scale Vent Arrangements
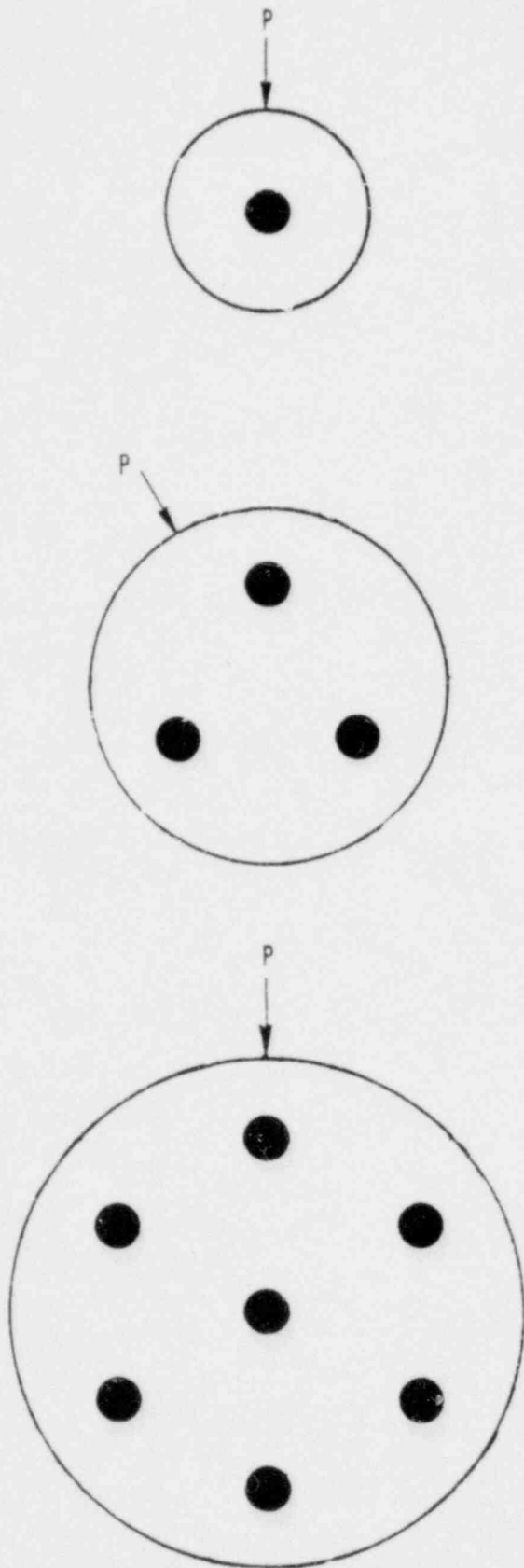
DIMENSIONS	NO OF VENTS		
	1	3	7
VENT DIAMETER	3.83"	3.83"	3.83"
POOL DIAMETER	17.25"	29.25"	44"
POOL TO VENT AREA RATIO	20.3	19.5	18.9

"P" DESIGNATES TYPICAL WALL PRESSURE TRANSDUCER LOCATIONS

Figure A3-4. Scaled Multivent Test Program 1/6 Scale Vent Arrangements

A4. SINGLE VENT CHUGGING

Four subscale (1/10, 1/6, 1/4 and 5/12 scale) single vent geometries were tested in the Scaled Multivent Test Program. The objectives of these single vent tests were as follows:

a. Obtain baseline single vent chugging data at 1/10 and 1/6 scale for comparison against the multivent data at these scales.

b. Obtain the effect of scale on single vent chugging so as to allow assessment of the applicability of subscale data trends to full-scale.

c. Obtain the effect of system conditions (steam mass flux, steam air-content, pool temperature) on chugging to allow understanding of full-scale blowdown test data.

A4.1 GENERAL OBSERVATIONS

Although the general characteristics of the chugging phenomena have been described in   reports (References A7, A12 and A13), a review of these characterist.   .t this time will be useful to the discussions of scaling considerations presented in Subsection A4.2. Briefly, a single vent geometry consists of the following elements (see Figure A4-1):

a. A steam space, generally referred to as the drywell, to which saturated steam (or a steam/water mixture) is supplied at a prescribed rate.

b. A pipe, generally referred to as the vent or downcomer, connected to the drywell at one end and the other end submerged in a pool of cold water.

c. A vessel, generally referred to as the wetwell, partially filled with cold water (the pool into which the vent is submerged) and with the remaining volume filled with air (the wetwell airspace).

In the single vent configuration representative of a single cell in the multi-vent Mark II suppression pool geometry, the drywell is mounted directly over the wetwell and the vent is a straight constant diameter pipe.

Chugging occurs in this system when the condensation rate at the vent exit exceeds the rate at which steam is supplied to the drywell. Figure A4-2 shows the pool bottom, vent static, and drywell pressure traces along with the water level traces during chugging in the 1/6 scale single vent geometry.

A typical chugging cycle occurs when at some point in the cycle the water exits the vent and the steam/water interface exits the vent (Point A in Figure A4-2) and forms a steam "bubble" at the vent exit in the pool. The steam/water inter-face is quickly cooled by turbulent convection in the pool and rapid condensation is triggered (Point B--Figure A4-2). The rapid condensation reduces the pressure in the steam bubble which results in a drop in the pool bottom wall pressure. The rapid condensation also causes a flow of steam from the drywell into the condensing region causing the vent static pressure to fall. Since the rate of condensation is larger than the rate at which steam is supplied to the drywell, the pressure in the drywell also decreases.

The steam bubble at the vent exit collapses producing a pressure spike in the pool (Point C--Figure A4-2) which excites the pool acoustic models (pool ring-out). A rapid reduction in the condensation rate at the vent exit occurs as the steam/water interface area is reduced substantially due to bubble collapse. Pressure oscillations are produced in the vent as a response to the reduced-condensation, thus resulting in reduced vent flow. These vent pressure oscil-lations (vent ringout) are transmitted into the pool via the steam/water inter-face. Therefore, the pressure oscillations measured at the pool wall are a composite of pool and vent ringouts.

Also in response to the drastically reduced condensation rate at the vent exit the drywell stops depressurizing. However, at this point the drywell pressure has dropped below the hydrostatic pressure at the vent exit and so water from the pool is drawn up into the vent (Point D--Figure A4-2). The

drywell starts to pressurize because of steam flow from the steam supply into the drywell and the near-zero condensation rate.

The rising drywell pressure decelerates and stops the rising of the water column (Point E--Figure A4-2) and then accelerates it out of the vent. Some condensation generally occurs as the water is discharged from the vent (Point F--Figure A4-2) and cold water is exposed to the steam, possibly due to deposition of a water film on the vent and/or motion-induced turbulence. Eventually, the rising drywell pressure expels the water from the vent (Point G--Figure A4-2) and the steam/water interface moves into the pool and the cycle repeats itself.

Figure A4-2 shows that each chug cycle varies from chug to chug. For example, in the chug starting at 18.4 seconds the drywell depressurization, the water entry height into the vent and the cycle period is considerably smaller than the preceding chug cycle discussed above. Since the magnitude of the drywell depressurization is directly related to the condensation process, it follows that the entire chug cycle is governed by the condensation process.

The overall chug cycle having described it is now appropriate to focus on the processes occurring while the steam/water interface is in the pool, because these processes control the overall characteristics of the chug cycle. Early in the Scaled Multivent Test Program, the 1/16 scale (vent id 1.5-in) single vent tests (CONMAP tests [Reference A14]) were performed to gain insight into the condensation processes occurring at the vent exit. In this part of the test program the wetwell was fabricated from a Pyrex glass pipe which enabled filming of the chugging on high speed movies.

The high speed movies were synchronized with high speed visicorder traces of the drywell, wetwell airspace, vent static and pool bottom center pressures. Coupling the movies with these high speed visicorder traces have provided valuable insights on the sequence of events occurring at the vent exit, i.e., the bubble formation and collapse processes that are primarily responsible for the pressure oscillations caused by a chug in the pool.

One immediate observation made from these movies was that each chug event differed from the others, i.e., the size and shape of the bubble formed at the vent exit and the detailed collapse characteristic were different in each chug. Some chugs had a substantial steam bubble formed at the vent exit, and usually the collapse of these bubbles produced needle-like pressure spikes in the pool. In other chugs the steam/water interface barely exited at the vent, and after a few oscillations near the vent exit the interface went back into the vent. Such condensation events generally produced sinusoidal oscillations in the pool and lacked the needle-like spike and the subsequential high frequency pool response.

Although details of the condensation process at the vent exit varied from chug to chug, some overall characteristics were common for most chugs. These characteristics were most clearly observed in the chugs which had a distinct bubble collapse (which also cause high amplitude pressure oscillations in the pool).

Figure 4-3 shows the visicorder traces for one of the chugs where a distinct bubble collapse occurred. This chug had a steam mass flux of 2 lbm/sec-ft^2, 0% steam air-content, and 100°F pool temperature. At the bottom of the figure is a line with a set of symbols corresponding to the key items noticed on the film. A frame by frame sequence of the same event is presented in Figure A4-4. The history starts where the bubble has almost reached its maximum size and ends after the water has entered the vent pipe. The other components of the entire chugging cycle including the penetration of water into the vent pipe, expulsion and growth of the bubble are not shown in Figure A4-3.

The chronological sequence of events represented in Figures A4-3 and A4-4 is described in the following paragraphs.

At 0.0 seconds* the bubble is growing, raising the level of the pool and compressing the air in the wetwell. The drywell pressure is dropping slowly, partly as a result of the expansion of the bubble and partly because of condensation (probably both in the vent and on the bubble walls). The pressure in the vent pipe is dropping slowly, following the drywell pressure. The bubble surface

---

*The time scale has an arbitrary zero.

appears shiny and smooth, although it is composed of a series of lobes rather than being a distinct sphere. The maximum bubble size is estimated from the movie to occur at 0.006 seconds. This corresponds with the maximum pressure in the wetwell.

During the bubble formation phase, the steam water interface is at saturation temperature (hence near zero condensation rate). The bubble is probably surrounded by a "blanket" of hot water which was heated while the water was in the vent. This blanket of hot water is convected away due to pool turbulence. This cools the steam water interface and triggers the rapid condensation.

In the next frame, at 0.008 seconds, there is the first appearance of a dark haze indicating the start of the rapid condensation on the bubble surface. We interpret this as the onset of an interfacial instability associated with extremely rapid condensation, probably limited by Mach Number or molecular kinetic effects rather than by the usual "heat transfer coefficient". At this time the pressures on the pool bottom and in the vent pipe starts to drop.

As the darkening of the bubble proceeds from 0.008 to 0.012 seconds, the vent and the pool bottom continue to depressurize. The pressure drop in the pool is indicative of a pressure decrease in the bubble as the rate of condensation builds up. Although this is not too evident in Figure A4-3, in general the pressure decline in the vent pipe lags the pool response by a millisecond or so, indicative of the time taken for acoustic waves to travel up the vent pipe. Except when rapid changes are occurring, the difference between the vent pipe pressure and the drywell pressure provides a measure of the flow rate from the drywell. The drywell pressure responds to the integral of this flow rate and there is an increasing downward slope to the drywell pressure trace as the vent depressurizes.

At about 0.013 seconds the vent pressure maintains a nearly constant value, slightly leading the corresponding constant rate of depressurization in the drywell. A quasi-steady flow has been set up, limited perhaps by the gas dynamics of the vent. The momentum of the steam flowing downwards in the vent

is transferred to the water in the pool via condensation at the steam/water interface. This induces a downward flow of water past the interface in the pool. This downward flow of water in the pool has been clearly observed in these and other movies of chugging and is partly responsible for the mixing and turbulence set up in the pool.

The bubble internal pressure should also have stabilized to some value on the order of a few psi below the pool pressure. This leads to collapse of the bubble, which is still attached to the vent. Thus, from 0.013 seconds to 0.018 seconds the pressure rises at the transducer located at the pool bottom as would be expected theoretically for bubble collapse under a constant applied overall pressure difference. During this period of time the wetwell depressurizes as the air expands to fill the volume given up by the collapsing bubble.

At about 0.017 seconds the film shows the onset of 'pinching" of the side of the attached bubble. The exact reason for this pinching has not yet been established. However, it probably occurs due to downward motion of the water in the pool induced by the condensation. This downward flow of water (and of course steam) imparts a downward motion to the collapsing bubble. Therefore, the bubble tends to separate from the vent, and a necessary prerequisite to complete separation is the formation of a neck that collapses more rapidly than the main body of the bubble. This pinching does not always occur, however, as some bubbles collapse back into the vent without releasing any large pressure pulse.

The formation of a neck (usually, but not always, near the vent) restricts the flow of steam to the collapsing bubble. Therefore, the pressure inside the bubble drops, as manifested by a declining pressure at the bottom of the pool from 0.018 seconds to 0.022 seconds when the bubble appears to be completely detached. The flow from the vent may or may not be influenced by the development of the bubble detachment, depending on how much steam is condensing above or below the neck. If the neck is near the vent exit (as it often is) the effect is to reduce the effective flow area and restrict the flow rate.

This is believed to be the reason for th small step in vent pressure that occurs at about 0.022 seconds. The area restric ion may be sudden and acute enough to actually induce a small shock wav that pr pagates up the vent against the steam flow. This is why the step in vent pressure is delayed two to four milliseconds behind the small peak in the pool trace.

As the bubble detaches, it begins to rapidly collapse (under an increased driving pressure difference) and it appears that the wetwell depres urization rate is enhanced (as shown in Figure 3 at 10.2 seconds).

At 0.023 seconds a sharp spike occurs in the pool trace. This is almost the time at which complete bubble collapse appears on the film. This collapse is evidenced by the large cloudy "bubble" being replaced by a small dispersed collection of small bubbles, presumably containing noncondensible gas. The overall "size" of this collection of small bubbles is minimum at "collapse" and may increase slightly later as the pressure drops. The pool also becomes much brighter as micro-bubbles in s spension are compressed, condensed, and dissolved.

The sequence of sharp spikes spaced about one millisecond apart on the pool trace is believed to be due to wave propagation in the water in the pool, i.e., the pool ringout.

At 0.023 seconds the water is observed to be drawn up inside the vent pipe and the steam-water interface disappears from view. This event usually happens about two milliseconds after bubble collapse, but sometimes occurs earlier or as much as 13 milliseconds later.

There is a sharp rise in vent pressure at 0.025 seconds that continues until 0.028 seconds. This sharp rise in the vent pressure signals the end of the rapid condensation as the steam/water interface is now in the vent. The pressure rise is caused by the sudden reduction in the rate of steam flow in the vent resulting from the "turning-off" of the rapid condensation. This situation is akin to that which occurs in pipe lines where the flow is suddenly stopped by the sudden closure of a valve and a compression wave is generated

which propagates upstream of the valve bringing the flow in the pipe to a stop.

Subsequent to the sharp rise in the vent static pressure there is a distinct change in slope of the drywell depressurization. This supports the idea of a compression wave originating at the steam/water interface (due to end of the rapid condensation) that passes the transducer in the vent and one to two milliseconds later reaches the drywell, immediately changing the flow rate out of the drywell. There is even a suggestion of temporary backflow into the drywell in some traces.

Following these events the vent "ring-out" occurs, where oscillations of decaying amplitude occur in the vent as the vent pressure equilibrates with the drywell pressure. These pressure oscillations are transmitted into the pool and are evident in the pool bottom pressure trace. Note that the phase difference observed between the vent static pressure and pool bottom pressure in this vent ringout phase is due to the differences in the propagation times of the signal to the vent static pressure transducer location in the vent and the pool bottom center transducer location

Figure A4-5 shows the drywell, vent static and pool bottom center pressures for a chug spike that occurred in Run 15 of the 4TCO Mark II prototypical full-scale single vent tests. All the features associated with the condensation induced bubble collapse and pressure responses of the pool, vent and drywell discussed above are present and remarkably similar in these full-scale data.

Considering the general features discussed above, the processes that occur at or near the vent exit were found to be present (although blurred at times) for all chugs that exhibit a spikey pool wall pressure trace.

In addition to the spikey chugs which generally produce the large pool wall pressure oscillations, the other general category of chugs observed was the oscillatory-type chugs. Figure A4-6 shows the drywell, vent static and pool

bottom center pressures and vent water level for a typical oscillatory type chug observed in the 1/6-scale single vent geometry.

In such a chug condensation is triggered almost immediately after the steam/water interface exits the vent. As a result a significant bubble is not formed at the vent exit. The condensation at the vent exit causes a flow in the vent and its pressure drops. The drywell depressurizes as flow is drawn out of it. However, the condensation rate is small enough that it does not dominate, but instead couples with the vent dynamics. The result is the interface and vent pressure oscillate at the coupled frequency of the system (generally close to the vent first harmonic). Finally, when the water around the interface is heated the condensation rate goes to near zero and water is drawn into the vent. However, because of a low condensation rate the drywell pressure is not much below the hydrostatic pressure at the vent exit and the water does not go up in the vent very far before it is quickly expelled out again.

Figure A4-7 shows an oscillatory type chug observed in the 4TCO chug full-scale single vent tests. Again, the chug exhibits all the features shown in the subscale data.

Based on the preceding discussions, all the elements that constitute the chugging phenomenon are shown in Figure A4-8. This figure shows that all the elements are interrelated and although condensation is the key element that "drives" all the other elements, they provide feedback that affects the condensation. For example, the water motion in and out of the vent is driven mainly by the condensation (both at vent exit and in the vent) induced drywell pressure oscillations. However, it is the motion of water in and out of the vent that is partially responsible for the turbulence in the pool and the bubble formation process, both of them influencing the condensation process. Similarly, the vent flow is driven by the condensation, but in turn influences the condensation rate if the vent chokes or, as in case of the oscillatory chug, where the condensation couples with the vent dynamics. Additional complexity is added

by the stochastic element injected by the turbulence in the pool that triggers condensation both at the vent exit and when the water is in the vent.

In summary, chugging is a rather complex phenomenon with many interacting elements. The phenomena is driven by condensation which in turn is affected by the response of the other elements. The current state of the art is such that very little is known about the detailed physics of condensation. Therefore, a complete first principles type analysis is not possible at the present time. However, as discussed in this and the following section, sufficient understanding of chugging has been gained from the available experimental data to allow analysis of the aspects of chugging that are relevant to the Mark II Chugging Loads Definition effort.

A4.2 SCALING CONSIDERATIONS

In the Scaled Multivent Test Program the tests for multivent effects were performed at 1/6 and 1/10 scale. Therefore, the main issue to be addressed in terms of effects of scale was to determine if the multivent effects observed at these subscales would also occur at full-scale.

When the Scaled Multivent Test Program was initiated scaling schemes were developed based on existing analytical models for chugging [References A15 and A16]. The models consisted of a set of equations describing the dynamics of the drywell, vent, pool and wetwell airspace. In both these analyses, simple ad hoc models were used to describe the condensation process occurring at the vent exit. Note, since then several other investigators have developed models for chugging [References A17, A18 and A19] which, except for minor details, have essentially the same set of governing equations.

The approach used in developing scaling schemes required the selection of appropriate reference parameters to non-dimensionalize the governing equations. Based on the choice of these reference parameters, dimensionless groupings were obtained that needed to be preserved in the subscale tests. Recognizing the

lack of knowledge on the physics governing the condensation processes and that the chugging phenomenon involved interactions of several complex processes helped establish the understanding that it would not be possible to derive a single scaling scheme that satisfied all aspects of the phenomenon. Therefore, two scaling schemes were selected with each one attempting to preserve a particular portion of the phenomenon.

In the Froude scaling scheme, the objective was to preserve the bubble formation process at the vent exit and the effect of gravity on the water motion in and out of the vent. In this Froude scaling scheme the following choice of reference parameters were chosen:

velocity V_x = $\sqrt{gh_x}$, where g is the gravitational constant

length L_x = D_v where D_v is the vent diameter

time t_x = Lx/Ux = $\sqrt{D_v/g}$

density ρ_x = ρ_{steam}

Using these reference parameters scaling requirements for the subscale tests were developed on the basis of preserving the various dimensionless groupings appearing in the non-dimensional governing equations. These scaling requirements for the Froude scaling scheme are listed in Table A4-1. As shown by the information given in this table, the important implications of Froude scaling are that the dimensions of the subscale geometries be linearly scaled and that the scaled tests be conducted at reduced pressure and mass flux. Although Froude scaling attempts to preserve the initial bubble formation at the vent exit and properly model the effects of gravity, it makes several compromises that effect pool response and condensation. Neither is it possible to satisfy the requirement on pool sonic velocity. Therefore, the pool response is considerably distorted in this scaling scheme. Also, this scheme requires that subcooling be scaled. This would result in pool temperatures at smaller scales that were very close to saturation temperature. This large distortion of pool subcooling affects the condensation process.

Nonetheless, due to the uncertainties involved at the time in the understanding of the relative importance of the various processes involved in chugging the decision was made to include Froude scaled tests in the test program.

The second scaling scheme used was the Mach scaling scheme. This scheme was based on the recognition that the condensation was the key process in chugging. The condensation phenomenon is mainly governed by the thermodynamic properties (such as subcooling, enthalpies, etc.) of both liquid and vapor phases. Further, during subscale tests at 1/10, 1/6 and 1/4 scales [Reference A7] the gross chug behavior (such as the period between chugs) was the same at all scales for a given steam mass flux (mass flow per unit vent area) into the drywell if the thermodynamic properties were kept constant from scale to scale. Further the flow in the vent was observed to be choked or reach a constant value of the Mach number during the rapid condensation at the vent exit. Therefore, a Mach scaling (although Mach is not the most appropriate name for this scaling approach) scheme was proposed which preserved the thermodynamic properties, the steam mass flux and the vent Mach number between scales. In Mach scaling the choice of reference parameters are:

$$U_x = a - \text{steam acoustic velocity}$$

$$L_x = D_v - \text{vent diameter}$$

$$t_x = L_x/U_x = D_v/a$$

$$\rho_x = \rho_{steam}$$

The effect that this choice of reference parameters has on the scale-model parameters is also shown in Table A4-1. Note that all dimensions are reduced by the scale factor, time is reduced by the scale factor, and the system overpressure and thermodynamic conditions are held at full-scale. This means that the scaled test would be conducted under prototype test conditions, but at scaled dimensions. Note that this scaling approach does not preserve the pool Froude number nor does it properly model the gravitational effects. However, the main advantage of this scheme is that it

preserves the thermodynamic properties controlling the condensation process and the gross chug characteristics which are controlled by the condensation. It also preserves the pool response to the impulse produced by the steam bubble collapse at the vent exit.

Because of the complex nature of the chugging phenomenon, neither scaling scheme will be able to satisfy all aspects of the phenomenon. Therefore, single vent tests at four subscales were performed in the Scaled Multivent Test Program over a wide range of conditions (both Froude and Mach scaled condition plus some tests at atmospheric wetwell airspace pressure). The data from these tests have been examined in terms of scale effects and their applicability to full-scale will be discussed later.

A4.3 ASSESSING THE APPLICABILITY OF SUBSCALE DATA TO FULL-SCALE DATA

As discussed previously a large body of single vent data has been generated over a wide range of test conditions. The question that must be answered now is under which test conditions do the subscale single vent data exhibit chugging characteristics similar to those observed at full-scale. After these test conditions have been identified, the multivent effects observed under these test conditions are expected to also occur at full-scale.

Based on the discussion of the various processes involved in chugging in Subsection 4.1, condensation is clearly the dominant process. Therefore, the first criterion used to assess similarity between data at various scales (including full-scale) will be that similar condensation rates occur during rapid condensation at the vent exit.

The other criterion used to assess similarity between scales will be that similar pool wall characteristics in terms of pool acoustic modes are excited, i.e., pool ringout. The pool wall pressure characteristics reflect the dynamics of the bubble collapse, i.e., the chug "source". The current Mark II generic methodology [Reference A20] involves deriving the chug "source" from

the pool wall pressures in a single vent geometry. Therefore, by examining the frequency content of the chug pool wall pressure characteristics the frequency content of the bubble collapse impulse can be deduced.

A4.3.1 Comparison of Condensation Rates at Various Scales

First, the condensation rate at various scales will be examined. The condensation rate can be most easily determined by examining the drywell pressure fluctuations. As discussed in Subsection 4.1, the drywell acts as a capacitance and the rate of pressurization or depressurization can be used to determine the flows in or out of it. From mass conservation for the drywell,

$$\frac{d \, (\rho_D V_D)}{dt} = \dot{m}_D - \dot{m}_C \tag{A4-1}$$

where

ρ_D = density of steam in the drywell

V_D = volume of the drywell

$\dot{m}_D$ = steam mass flow rate into the drywell

$\dot{m}_C$ = steam mass flow rate out of the drywell

The drywell pressure p_D and density ρ_D are related as follows

$$p_D \rho_D^{-k} = \text{constant} = P_{DO} \rho_{DO}^{-k} \tag{A4-2}$$

where p_{DO} and ρ_{DO} are the time averaged drywell pressure and density and k is the polytropic exponent. Combining Equations A4-1 and A4-2 and rearranging terms,

$$\dot{m}_C = \dot{m}_D - \frac{V_D \rho_{DO}}{k \, P_{DO}^{1/k}} \cdot P_D^{(1-k)/k} \frac{dp_d}{dt} \tag{A4-3}$$

Equation A4-3 in terms of steam mass fluxes is

$$\dot{m}_c'' = \dot{m}_D'' - \frac{V_D \rho_{DO}}{k \, A_v P_{DO}^{1/k}} \, p_D^{(1-k)/k} \, \frac{dp_D}{dt} \tag{A4-4}$$

where

$\dot{m}_c''$ = steam mass flux out of drywell

$\dot{m}_D$ = steam mass flux into the drywell

A_V = vent cross sectional area

During the time that the rapid condensation occurs at the vent exit, $\dot{m}_c''$ is essentially the steam mass flux condensed.

Drywell pressure traces from selected single vent tests at the four scales were first filtered to remove noise and smooth out pressure oscillations caused by the unsteady vent flow dynamics. The slope of the drywell pressure, i.e., dp_D/dt were calculated within a time window that adequately covered the duration of condensation at the vent exit. The steam mass flux $\dot{m}_c''$ out of the drywell was calculated using Equation A4-4. The duration of the rapid condensation τ_{COND}, was taken as the duration over which $\dot{m}_c'' > 2$ lbm/sec-ft^2. Figure 4-9 illustrates the above procedure.

Figure A4-9a shows the raw drywell pressure trace during the rapid condensation at the vent exit for a chug in the 1/6 scale single vent geometry.* The raw trace has a small amount of random noise superimposed on it as well as legitimate pressure oscillations following the depressurization. These pressure oscillations are due to the vent ringout — the unsteady flow dynamics in the vent as discussed earlier in Subsection 4.1.

---

*Test CJ3630A; 4 lbm/sec-ft^2 steam mass flux, 0% steam air-content, 130°F pool temperature, and 45 psia wetwell airspace pressure.

A two step digital filtering process is used where a 200 Hz low pass filter was used to first remove the random noise from the pressure trace as shown in Figure A4-9b. Second, a low pass filter was used with a cutoff frequency appropriate for smoothing the unsteady component produced by the vent. The resulting smoothed drywell pressure is shown in Figure A4-9c. The slope, i.e., dp_D/dt, was then computed (Figure 4-9d) from which the condensation mass flux, $\dot{m}_c''$, was calculated using Equation A4-4. The resulting variation of $\dot{m}_c$ as a function of time is shown in Figure A4-9e. Figure A4-9e shows that before the rapid condensation started, $\dot{m}_c''$ has a value below lbm/sec-ft^2 (dotted line in Figure A4-9e), probably due to some small amount of condensation occurring in the vent as well as the physical displacement of the water column in the vent. As rapid condensation starts at the vent exit $\dot{m}_c''$ rises rapidly reaching around lbm/sec-ft^2 at the peak of the condensation process. Then, $\dot{m}_c''$ starts to decrease rapidly as the rapid condensation process at the vent exit comes to a halt and $\dot{m}_c''$ drops below lbm/sec-ft^2.

These quantities are recorded from the computed $\dot{m}_c''$ the duration of the rapid condensation τ_{COND} (when $\dot{m}_c''$ is greater than 2 lbm/sec-ft^2), the peak value* $\dot{m}_{cp}''$, and the average value $\dot{m}_{ca}''$ over the interval τ_{COND}. These quantities were obtained for as many as 100 chugs from each test analyzed (some tests had less than 100 chugs occur in the period that data were recorded). Then, average values and standard deviations were computed for each of these quantities.

Figure 4-10 shows the average condensation steam mass flux during rapid condensation at the vent exit at various subscales and full-scale (4TCO data) for various test conditions. This figure also shows that the condensation mass flux is maintained reasonably constant between various scales for the Mach scaled test conditions. Therefore, maintaining full-scale test conditions does appear to preserve the condensation rates at the vent exit.

---

*The peak value of $\dot{m}_c''$ is obtained using the 200 Hz low pass filtered drywell trace to obtain as realistic a value as possible.

On the other hand, the condensation steam mass flux decreases with increasing scale for the Froude scaled test conditions. Further, the decrease in the condensation mass flux does not follow the $S^{1.5}$ as would be expected based on the Froude scaling scheme.

As discussed in Subsection 4.1, the condensation at the vent exit is the most important process in the chugging cycle and governs the gross chug behavior. Therefore, it was concluded on the basis of the discussion that since the subscale tests at Mach scaled conditions preserve the condensation rate at the vent exit the data from these are representative of the gross chug behavior at full-scale. Similarly, it was concluded that test data at Froude scaled conditions are not representative of the gross chug behavior at full-scale.

A4.3.2 Comparison of Pool Response Characteristics at Various Scales

The pool wall pressure characteristics of the subscale data are compared with those observed in the Mark II prototypical 4TCO full-scale single vent tests [Reference A5]. Figure A4-11 shows the largest chugs observed in the 4TCO tests and their corresponding PSDs are shown in Figure A4-12. These large chugs were selected from the 4TCO tests because these chugs are the bounding 4TCO chugs and will play a central role in the development of the Mark II Chugging Load Definition.

The time traces shown in Figure A4-11 are the response of the pool to the chug forcing function (the steam bubble collapse and the vent pressure oscillations). The vent pressure oscillations occur at the vent harmonic frequencies and can be identified by examining the PSDs of the pressure traces shown in Figure A4-12. The lowest vent frequency corresponds to a 1/4 standing wave in the vent (between 5 and 10 Hz for the 4TCO vent). The highest vent harmonic frequency observed usually corresponds to the 3/4 standing wave (between 15 and 30 Hz). The intermediate 1/2 wave frequency was also observed in some chugs.

The forcing function for the steam bubble collapse is impulsive in nature (for example that expected from Rayleigh bubble collapse type calculations) and can be approximated by a triangular impulse [Reference A20]. The width of this triangular impulse, i.e., the frequency content, is related to the bubble collapse time. This impulsive forcing function excites the pool acoustic modes.

With proper models of the pool the pressure traces at the pool wall can be used to backout the impulsive forcing function due to the bubble collapse and the sinusoidal forcing function for the vent components [Reference A20]. As previously discussed, PSDs of the vent pressure show that in the 4TCO tests the pressure oscillations in the vent steam space do not have any significant power at frequencies above that for a 3/4 standing wave in the vent (above 30 Hz). Therefore, the higher frequencies observed in the PSDs of the pool wall pressure traces (Figure A4-12) are the pool modes excited by the impulsive forcing function due to the steam bubble collapse. Based on the PSDs shown in Figure A4-12, the conclusion can be made that on impulsive forcing function must have an impulse width small enough for the impulsive forcing function to have a significant frequency content of at least a 100 Hz to be capable of exciting any dominant pool models that occur in that frequency range (usually the axial pool modes).

In the subscale geometries the pool dimensions are reduced linearly by the scale factor (see Subsection 4.2). Therefore, the frequencies of the pool modes go up in inverse proportion to the scale factor. This implies that to preserve the modal response of the pool observed at full-scale, the frequency content of the impulsive forcing function caused by the bubble collapse must also extend to the inverse of the scale factor.

Figure A4-13 shows the pool bottom wall pressure trace and the corresponding PSD for a chug in the 1/10-scale single vent geometry at Mach scaled test conditions. The vent length for this geometry was 9.5-ft (see Table A3-1). Therefore, the frequency of the lowest vent harmonic is 40 Hz and the vent

third harmonic is around 120 Hz. Hence, the frequencies above an approximate 120 Hz are due to pool response to the bubble collapse impulse; the first mode of the pool appears around 300 Hz. Note, by the plot of the cumulative power (dotted line on the PSD plot) most of the power lies below a 1000 Hz. This is precisely the pool response that would be expected in the 1/10-scale geometry based on the response of the full-scale pool discussed above.

Figures A4-14, A4-15 and A4-16 show the pool bottom pressure traces and the corresponding PSD for chugs in the 1/6, 1/4 and 5/12 scale single vent geometries respectively at Mach scaled conditions. These figures show the pool responses are consistent with those expected as based on the full-scale pool response and linear scaling of the pool size. Therefore, the pool response similarity and similarities between the characteristics of the impulse produced by the bubble collapse are preserved between scales at full-scale, i.e., Mach scaled test conditions in the subscale single vent geometries.

The pool bottom pressure trace and its corresponding PSD for a chug in the 1/10-scale geometry at Froude scaled conditions are shown in Figure A4-19. The striking feature seen in this figure is that most all the power in the PSD is below 100 Hz with much of it at the first vent harmonic, and the remaining power at the second vent harmonic. This means that at the Froude scaled conditions in the 1/10-scale geometry, the bubble collapse is retarded to a point where its frequency content is very low. The pool response is totally distorted.

The same observation holds true for the pool response to chugs in the 1/6-scale geometry at Froude scaled conditions as seen from Figure A4-18. The pool responses are somewhat less distorted with decreasing scale, i.e., for the 1/4 and 5/12 scales as shown in Figures A4-19 and A4-20, respectively.

The distortion of the pool response at Froude scaled conditions was expected to a certain degree, because as discussed in Subsection A4.2 Froude scaling

requires that pool sonic velocity be scaled by $S^{1/2}$ where S is the scale factor. Obviously this cannot be achieved if water is used and the pool response distorted. In addition, there is further distortion in the pool response which is related to the distortion of the bubble collapse dynamics.

Consider the Rayleigh bubble collapse equation for a spherical bubble collapsing in the pool of liquid:

$$\ddot{R}R + \frac{3}{2}\dot{R}^2 = \frac{p_b - p_o}{\rho_\ell}$$

where R is the bubble radius at some time t, p_b is the pressure inside the bubble, and p_o is the pressure in the surrounding liquid, and ρ_ℓ is the density of the liquid. For simplicity it is assumed that p_b and p_o are constant.* The bubble collapse time t_c, is then proportional to

$$R_o \sqrt{\frac{p_o - p_b}{\rho_\ell}}$$

Now it is reasonable to assume that R_o is proportional to the vent diameter D_v. Therefore,

$$t_c \; \alpha \; D_v \sqrt{\frac{\rho_\ell}{p_o - p_b}} \qquad\qquad (A4-5)$$

In the Froude scaling scheme, the vent diameter and system pressures (i.e., p_o) are reduced by the scale factor S and hence the bubble collapse time is reduced by $S^{1/2}$ if p_b goes as S^{-1}. In fact, the pressure p_b inside the collapsing bubble is related to the actual pool water temperature (as opposed to subcooling). Therefore, for a given pool temperature, p_b remain a constant

_____

*The arguments developed hold even if p_b varys with time as assumed in Reference A15.

to the first order even if the system pressure p_o is reduced by $S^{1/2}$ as per
Froude scaling. Hence, the bubble collapse time does not scale as $S^{1/2}$
(which also implies that the bubble collapse dynamics are distorted), but by
a factor larger than $S^{1/2}$, i.e., the bubble collapse is slower than expected
from the Froude scaling scheme. This and the inability to scale pool sonic
velocity causes a very distorted pool response.

In case of Mach scaling, where full-scale conditions are preserved including
the pool temperature, both p_o and p_b are preserved at full-scale values and
hence the bubble collapse time t_c is reduced by the scale factor. Since the
pool dimensions are also reduced by the scale factor, the pool response is
preserved as shown by the data.

In summary, the Froude scaling scheme is unable to correctly preserve the
condensation rate, the bubble collapse and pool response characteristics.
Therefore, the conclusion is that Froude scaled data cannot be used for
drawing conclusions regarding chugging behavior at full-scale.

On the other hand, the Mach (although Mach is a misnomer) scaling scheme which
requires testing a prototypical system conditions preserves the condensation
rate, the bubble collapse and pool response characteristics from scale to
scale. Therefore, the trends from the Mach scaled data should remain valid
at full-scale. Thus, in the remainder of the report, only the Mach scaled
data will be considered.

A4.4 SUBSCALE AND FULL-SCALE DATA TRENDS

After having determined the subscale data that are representative of chugging
at full-scale the trends of these data with system conditions can be used to
understand and interpret the full-scale data obtained from blowdown tests.
The subscale data trends obtained in the Scaled Multivent Test Program were
reported in References A1 and A2. Therefore, only the salient points regarding
these data trends will be discussed here.

A4.4.1 Subscale Data Trends

The subscale tests in the Scaled Multivent Test Program were performed in a
steady-state mode (Subsection A2.1), i.e., system conditions (steam mass
flux, steam air-content, pool temperature, and wetwell airspace pressure)
were maintained constant for the duration of a given test. This allowed
the determination of the dependence of chugging on system conditions in a
systematic manner.

As previously discussed, the tests performed at the full-scale values of the
system conditions (Mach scaled conditions) are representative of chugging
behavior at full-scale. Therefore, the data trends presented are from the
Mach scaled tests, which constitute over half the tests performed. Since
testing at full-scale conditions fixes the wetwell airspace pressure at 45 psia,
the remaining system conditions of interest are the steam mass flux, steam
air-content and pool temperature.

The data trends are presented in terms of the mean peak overpressure (POP),
peak underpressure (PUP) and chug frequency (inverse of the mean period
between chugs, t_p). The mean values are computed from the values of these
parameters for individual chugs in a given test. Due to the strong stochastic
element present in chugging, the values of these parameters vary substantially
from chug to chug and the standard deviations are generally of the same order
as the mean values. Nonetheless, the mean values are well behaved and
repeatable for a given test condition. Further, the data trends will be
presented mostly for the mean POP and PUP at the pool bottom elevation,
because the data trends with system conditions were found to be the same at
other pool locations.

A4.4.1.1 Effect of Steam Mass Flux

The effects of steam mass flux on mean POP, PUP and chug frequency are shown
in Figure A4-21, A4-22 and A4-23, respectively, for the single four subscale
single vent geometries. In general, the data trends are similar at all
four scales.

The mean POP increases almost linearly up to a steam mass flux of 2 lbm/ft^2-sec. There is a distinct reduction in the mean POP as the steam mass flux is increased from 2 to 4 $lbm/sec-ft^2$, followed by a rise in mean POP as the steam mass flux is increased more. This trend is particularly marked for the larger scales.

This reduction in mean POP from 2 $lbm/sec-ft^2$ to 4 $lbm/sec-ft^2$ is due to a change in the characteristics of the chugs. At 2 $lbm/sec-ft^2$ most of the chugs are the classical type, i.e., spiky chugs. At 4 $lbm/sec ft^2$, however, oscillatory type chugs occur predominantly [Reference A2].

As the steam mass flux is increased beyond 8 $lbm/sec-ft^2$, the mean POP again increases. The trend in mean PUP (Figure A4-22) is similar to that for the mean POP. In all the scales, the mean chug frequency increases almost linearly with steam mass flux (Figure A4-23).

A4.4.1.2 Effect of Pool Temperature

The effects of pool temperature on the mean POP and PUP at various steam mass fluxes are shown in Figures A4-24 and A4-25 for the 1/6-scale single vent geometry. In all steam mass fluxes, except 16 $lbm/sec-ft^2$, the mean POP reaches a maximum at a pool temperature between 130°F and 170°F. At 16 $lbm/sec-ft^2$, the mean POP increases continuously with pool temperature over the range of pool temperatures tested. Hence, for all values of the steam mass flux, the mean POP would approach zero as the pool temperature approached the saturation temperature. Therefore, a maximum in the mean POP is expected to occur between a pool temperature of 200°F and 275°F (saturation temperature at 45 psia wetwell airspace pressure) at the 16 $lbm/sec-ft^2$ steam mass flux.

In general, the mean PUP decreases with increasing pool temperatures for steam mass fluxes up to 8 $lbm/sec-ft^2$. At the highest steam mass flux of 16 $lbm/sec-ft^2$ the pool temperature did not have any significant effect on the mean PUP over the range of pool temperatures tested. The mean PUP is expected to approach zero as the pool temperature approaches the saturation value.

The effect of pool temperature on the mean chug frequency is shown in Figure A4-26. The pool temperature is seen as having no significant effect on the chug frequency for steam mass fluxes of 4 lbm/sec-ft^2 and lower. At higher steam mass fluxes, a slight pool temperature effect was observed where the mean chug frequency peaks between 130°F and 170°F, after which it decreases as the pool temperature is increased.

These pool temperature trends observed at 1/6 scale were present at the other subscales also [References A1 and A2].

A4.4.1.3 Effect of Steam Air-Content

The effects of steam air-content on the mean POP and PUP are shown in Figures A4-27 and A4-28 respectively in the 1/6 scale single vent geometry. Both mean POP and PUP decrease continuously with increasing steam air-content. Steam air-content does not change the mean chug frequency, however, it affects the characteristics of the chugs significantly (the sharp spikes become rounded and the pool ringout frequency was drastically reduced).

This same data trends were observed at all subscales.

In summary, the system conditions affect the chugging pool wall pressure characteristics. A physical explanation of the trends observed is given in Reference A7. Finally, the data trends were also observed in the multivent geometries.

A4.4.2 Interpretation of Full-Scale Blowdown Data

All the full-scale tests (4T, 4TCO and JAERI) have been performed in the blowdown mode. Therefore, the system conditions such as steam mass flux, steam air-content and pool temperature were changed through the course of these blowdown tests. The subscale steady-state data trends however, have made it possible to understand and interpret the data from these full-scale blowdown tests.

Figure A4-29 shows the variation of the vent steam mass flux, steam air-content and bulk pool temperature as a function of time for 4TCO Test 25 which was a 2.5 in. liquid break. Figure A4-30 shows that at the start of the blow-down the vent steam mass flux rises rapidly as air is purged out of the dry-well and then drops off gradually as the steam generator vessel blows down. The steam air-content falls continuously from the start of the blowdown and drops below 0.1% at around 30 seconds into the blowdown. The bulk pool temperature rises continuously through the blowdown and the total rise is about 40°F.

Besides the parameters (steam mass flux, steam air-content, and pool tempera-ture) discussed above, and additional air in the pool from the pool swell transient phase. After the pool swell transient, the pool is expected to have a fairly large amount of air in the form of dispersed bubbles. These bubbles rise under the influence of gravity. However, the downward flow induced by the condensation tends to sweep some of these bubbles back into the pool. Therefore, these bubbles clear out of the pool and into the wetwell airspace at a lower rate than under the influence of gravity alone.

The presence of free air bubbles in the pool tend to have the same mitigating effect as air in the steam. This was observed in some preliminary tests performed in the 1/16 scale single vent geometry. However, at present no measurement of the distribution of air in the pool are available, and also no data are available to quantitatively determine the influence of this free air in the pool on the chugging characteristics. Therefore, the effects of air in the pool cannot be quantified in the following discussion, but the fact that air in pool does mitigate, chugging should be kept in mind when analyzing blowdown data.

Figure A4-30 shows the measured pressure time history at the 4TCO pool bottom center for 4TCO Run 25 after the initial pool swell transient period. As shown by this figure, the amplitude of the pressure oscillations increases initially as the blowdown progresses and large amplitude chugs occur around 30 seconds into the blowdown. After that, the amplitudes decrease to the end

of the blowdown. This trend is more clearly seen in Figure A4-31 which shows the mean POP over consecutive 10 second intervals of the blowdown.

This behavior of the POP as a function of time into the blowdown can be explained based on the data trends from the subscale data discussed earlier and the steam mass flux, steam air-content and pool temperature histories shown in Figure A4-29. After the initial pool swell transient, steam with a high air-content is purged into the pool (see Figure A4-29). Due to the high steam air-content, the condensation rate at the vent exit is low and as expected from the subscale POP trends with steam air-content, the POP of the pressure oscillations is small. As the steam air-content decreases (and also pool air-content) with time in the blowdown, the condensation rate at the vent exit increases and the POP increases.

This behavior of the POP as a function of time into the blowdown can be explained based on the data trends from the subscale data discussed earlier and the steam mass flux, steam air-content and pool temperature histories shown in Figure A4-29. After the initial pool swell transient, steam with a high air content is purged into the pool. Due to the high steam air-content, the condensation rate at the vent exit is low and as expected from the subscale POP trends with steam air-content the POP of the pressure oscillation is small. As the steam air-content and pool air-content decreases with time in the blowdown, the condensation rate at the vent exit increases and the POP increases.

As shown in Figure A4-29, the air-content drops below 0.1% around 30 seconds into the blowdown. The subscale test showed that below this value of 0.1% the steam air-content did not have any significant effect on POP and, for all practical purposes, the vent steam can be considered air-free. As expected, the amplitudes of the chugs is quite large around 30 seconds into the blowdown with the chugs exhibiting the spikey pressure time histories characteristics of air-free chugging.

Once the steam is "air-free", i.e., steam air-content below 0.1%, the POP behavior is controlled by the variation of the steam mass flux and pool

temperature (and possibly the air present in form of bubbles in the pool).
Figure A4-29 shows that after 30 seconds where the steam can be considered
"air-free" the bulk pool temperature rises by only 13°F. Therefore, based on
the subscale data trends this is not expected to influence POP variation
significantly. However, the steam mass flux starts dropping rapidly beyond
30 seconds into the blowdown. Therefore, based on the effect of steam mass
flux on POP observed in the subscale tests the POP is expected to decrease
continuously as the steam mass flux decreases (see Figures A4-30 and A4-31).

Therefore, the variation of chug amplitudes during the full-scale 4TCO blow-
downs is consistent with the system conditions dependence observed in the
subscale steady-state test data.

The JAERI wall pressure data were analyzed to determine if similar system
conditions dependence was also observed in the JAERI full-scale multivent
tests. The pool wall pressure information in the JAERI data reports is
presented in the form shown in Figure A4-32 where the envelopes of the peak
overpressure (POP) and peak underpressure (PUP) are plotted on the decimated
time plot of the pool wall pressure for the entire blowdown. Such data are
available for the pool and vent wall pressure locations shown in Figures A4-34
and A4-35 (WPPF and VPPF are pool and vent pressure transducers, respectively).

As shown in Figure A4-32, there is difficulty in distinguishing individual
chugs from the POP and PUP envelope. Therefore, average values for POP and
PUP were obtained by averaging the respective envelopes over 10 second con-
tiguous intervals for the entire blowdown.

Initially, the mean POP and PUPs over 10 second intervals were obtained for
the pool bottom transducers. However, because of the geometry and installation
method used for the pool bottom transducers, the data was found to be
unreliable. Therefore, the 10 second mean POPs and PUPs were obtained for
the pool sidewall transducers (WWPF202, WWPF302, WWPF402, WWPF502, WWPF602
and WWPF702 (see Figure A4-34 and A4-35) data which are probably more reliable.

However, Figures A4-33 and A4-35 show these sidewall transducers at the vent
exit elevation are located in close proximity to different vents. Therefore,
the pressures measured by a given transducer will be heavily biased towards
the chugs occurring at the vent closest to that transducer. For example,
Figure A4-36 shows the 10 second mean POPs as a function of blowdown time for
the six vent exit elevation locations (WWPF202, WWPF302, WWPF402, WWPF502,
WWPF602 and WWPF702 (see Figures A4-33 and A4-35) for JAERO Test 0002.
This figure shows considerable spatial variation, i.e., variation from loca-
tion to location even in the 10 second mean POPs. The reason for this spacial
variation is that chug strengths vary considerably from vent to vent. The
average value for the 10 second mean POPs at the various vent exit elevations
will be used in order to smooth out this spatial variation caused by the
vent to vent variations in chug strengths.

The spatially averaged value for the 10 second mean POPs as a function of
blowdown time for JAERI Test 0002 is shown in Figure A4-37. The POP is shown
as reaching a peak value around 65 seconds into the blowdown. This behavior
of the POP can be understood if one looks at the system conditions variation
during the blowdown. Figure A4-38 shows the variation of the steam mass flux
and steam air-content as a function of blowdown time for this test. Fig-
ure A4-38 shows that the steam-air content is dropping continuously into the
blowdown and drops below 0.2% around 64 seconds (about the time where the
average POP peaks). After the steam-air content has dropped below 0.1% the
behavior of average POP follows a downward trend due to decreasing steam
mass flux.

Again this observed dependence of the average POP with air-content and steam
mass flux is consistent with the trends seen in the subscale tests. Therefore,
the JAERI full-scale multivent data exhibit system conditions dependence
which is consistent with that observed in both the subscale and 4T tests.

Table A4-1
CHUGGING SCALE-MODEL PARAMETERS

$$\text{Scale Factor} = S = \frac{(L_x) \text{ scaled}}{(L_x) \text{ prototype}}$$

Reference Parameter	Froude Scaling	Mach Scaling
reference length L_x	D_v	D_v
reference velocity U_x	$\sqrt{gD_v}$	a
reference time t_x	$\sqrt{D_v/g}$	D_v/a
reference density ρ_x	ρ_{steam}	ρ_{steam}

Scale-Model Parameters	Froude Scaling Requirement	Math Scaling Requirement
$\dfrac{m_D t_x}{\rho_x V_D}$	$m_D \sim S^{7/2}$ (scaled mass flux)	$m_D \sim S^2$ (full-scale flux)
$\dfrac{A_v L_x}{V_D}$	$V_D \sim S^3$ (scaled drywell)	$V_d \sim S^3$ (scaled drywell)
$\dfrac{a}{U_x}$	$a \sim S^{1/2}$ (cannot achieve)	$a \sim S^\circ$
$\dfrac{fL_x}{D_v}$	$f \sim S^\circ$ (full scale friction)	$f \sim S^\circ$ (full scale friction)
$\sqrt{\dfrac{\rho_x}{\rho_w}}\dfrac{a}{U_x}$	$p \sim S$ (scaled pressure)	$p \sim S^\circ$ (full scale pressure)
$\dfrac{U_x^2}{gL_x}$	$t_x \sim S^{1/2}$ (scaled time)	$g \sim S^{-1}$ (cannot achieve)
$\dfrac{C_w \Delta T \rho_w}{h_{fg}\rho_x}$	$\Delta T \sim S$ (scaled subcooling)	$\Delta T \sim S^\circ$ (full scale subcooling)

Table A4-1 (Continued)

Scale-Model Parameters	Froude Scaling Requirement	Math Scaling Requirement
$\dfrac{D_v}{L_x}$, $\dfrac{A_v}{L_x^2}$	$D_v \sim S$ (scaled vent)	$D_v \sim S$ (scaled vent)
$\dfrac{a_w}{U_x}$	$a_w \sim S^{1/2}$ (cannot achieve)	$a_w \sim S^\circ$

Figure A4-1. Schematic of the Drywell/Wetwell

The following Figures are General Electric Company Proprietary and have been removed from this document in their entirety.

A4-2   The "Chug" Cycle

A4-3   Pressure Traces for a "Selected Event"

A4-4   Successive Frames from the Movie Showing the Bubble in Figure 1

A4-5   A High Amplitude Classical Chug from 4TCO Test Run 15

A4-6   An Oscillatory Chug from a 1/6 Scale Vent Test

A4-7   An Oscillatory Chug from 4TCO Test Run 13

Pool Wall
Pressure
Oscillations

```
                        ┌─────────────────────┐
                        │ Initial Conditions: │
                        │ Bubble size & shape;│
                        │ Local pool tem-     │
                        │ perature- etc.      │
                        └─────────────────────┘
                                                      ┌──────────────────┐
┌──────────┐   ┌──────────┐   ┌──────────────┐        │ Pool Heat        │
│ Acoustic │   │ Steam    │   │ Condensation │        │ Transfer         │
│ Response │ ← │ Bubble   │ ← │ at Vent Exit │        │ Characteristics  │
│ of the   │   │ Collapse │   │              │        │ (Turbulence,     │
│ Pool     │   │          │   │              │        │ Pool Temp., etc. │
└──────────┘   └──────────┘   └──────────────┘        └──────────────────┘

                               ┌──────────────┐
                               │ Unsteady Flow│        ┌──────────────────┐
                               │ Dynamics In  │        │ Properties of    │
                               │ The Vent     │        │ the steam such   │
                               └──────────────┘        │ as air-content,  │
                                                       │ etc.             │
                               ┌──────────────┐        └──────────────────┘
                               │ Drywell      │
                               │ Dynamics     │        ─ Steam from steam
                               └──────────────┘             supply

                                              ┌──────────────────┐
                                              │ Condensation in  │
                                              │ the vent         │
                                              └──────────────────┘
┌──────────┐                   ┌──────────────┐
│ Wetwell  │                   │ Water Motion │
│ Airspace │ →                 │ in and out   │
│ Dynamics │                   │ of the vent  │
└──────────┘                   └──────────────┘

                               ┌──────────────┐
                               │ Pool Inertial│
                               │ Dynamics     │
                               └──────────────┘
```

Figure A4-8. Interactive Processes in Chugging

The following Figures are General Electric Company Proprietary and have been removed from this document in their entirety.

A4-9   Drywell Pressure Trace - Data Reduction to Obtain $\dot{m}''_c$

A4-10   Steam Mass Flux During Rapid Condensation as a Function of Scale

A4-11a   Large Amplitude Chugs from the 4TCO Tests

A4-11b   Large Amplitude Chugs from the 4TCO Tests

A4-12a   PSDs of the Chugs from the 4TCO Tests Shown in Figure A4-11

A4-12b   PSDs of the Chugs from the 4TCO Tests Shown in Figure A4-11

A4-13   Pressure Time History and PSD for a Chug in the 1/10 Scale Single Vent Geometry, Mach Scaled Conditions

A4-14   Pressure Time History and PSD for a Chug in the 1/6 Scale Single Vent Geometry, Mach Scaled Conditions

A4-15   Pressure Time History and PSD for a Chug in the 1/4 Scale Single Vent Geometry, Mach Scaled Conditions

A4-16   Pressure Time History and PSD for a Chug in the 5/12 Scale Single Vent Geometry, Mach Scaled Conditions

A4-17   Pressure Time History and PSD for a Chug in the 1/10 Scale Single Vent Geometry, Froude Scaled Conditions

A4-18   Pressure Time History and PSD for a Chug in the 1/6 Scale Single Vent Geometry, Froude Scaled Conditions

A4-19   Pressure Time History and PSD for a Chug in the 1/4 Scale Single Vent Geometry, Froude Scaled Conditions

A4-20   Pressure Time History and PSD for a Chug in the 5/12 Scale Single Vent Geometry, Froude Scaled Conditions

A4-21   Variation of Mean POP at Pool Bottom Elevation with Steam Mass Flux (130° Pool Temperature), Single Vent Tests at Four Scales

A4-22   Variation of Mean PUP at Pool Bottom Elevation with Steam Mass Flux (130° Pool Temperature), Single Vent Tests at Four Scales
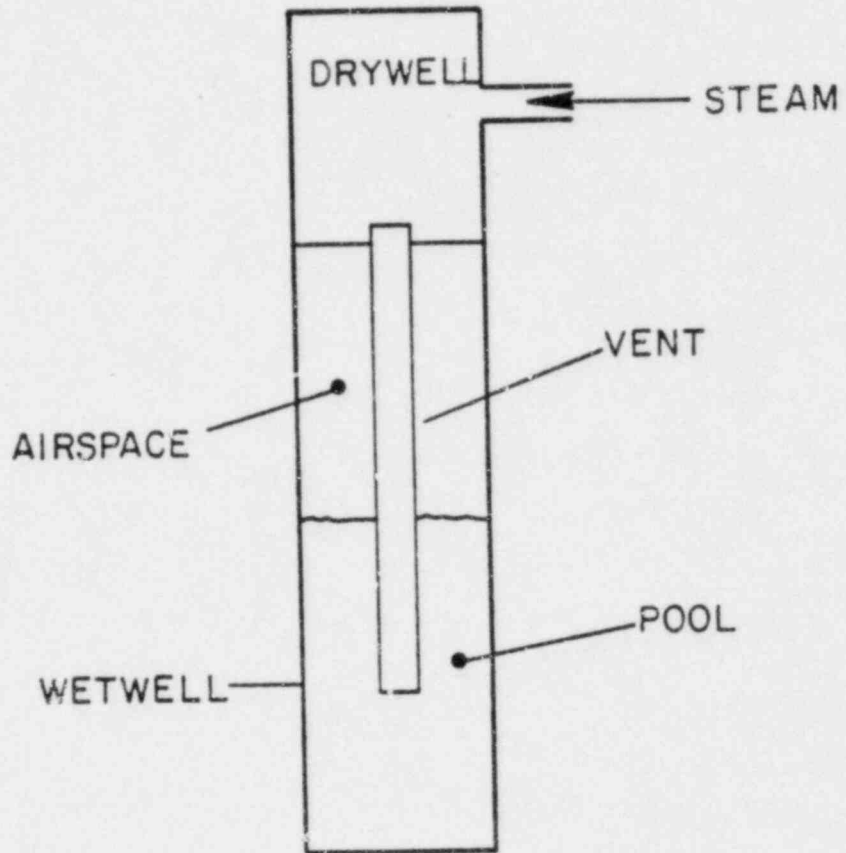
The following Figures are General Electric Company Proprietary and have been removed from this document in their entirety.

A4-23   Variation of Mean Chug Frequency wity Steam Mass Flux (130°
          Pool Temperature), Single Vent Tests at Four Scales

A4-24   Variation of Mean POP at Pool Bottom Elevation With Pool
          Temperature, 1/6-Scale Single Vent Tests

A4-25   Variation of Mean PUP at Pool Bottom Elevation With Pool
          Temperature, 1/6-Scale Single Vent Tests

A4-26   Variation of Mean Chug Frequency With Pool Temperature,
          1/6 Scale Single Vent Tests

A4-27   Variation of Mean POP at Pool Bottom Elevation With Steam
          Air-Content, 1/6 Scale Single Vent Tests

A4-28   Variation of Mean PUP at Pool Bottom Elevation With Steam
          Air-Content, 1/6 Scale Single Vent Tests

A4-29   Blowdown History for 4TCO Test 25

A4-30   Pool Bottom Pressure Time History for 4TCO Test 25

A4-31   Variation of Mean POP During the Blowdown, 4TCO Test 25

A4-32   Wetwell Pool Bottom Pressure, JAERI Test 2101

Figure A4-33. Plan Locations of Transducers for JAERI Wetwell
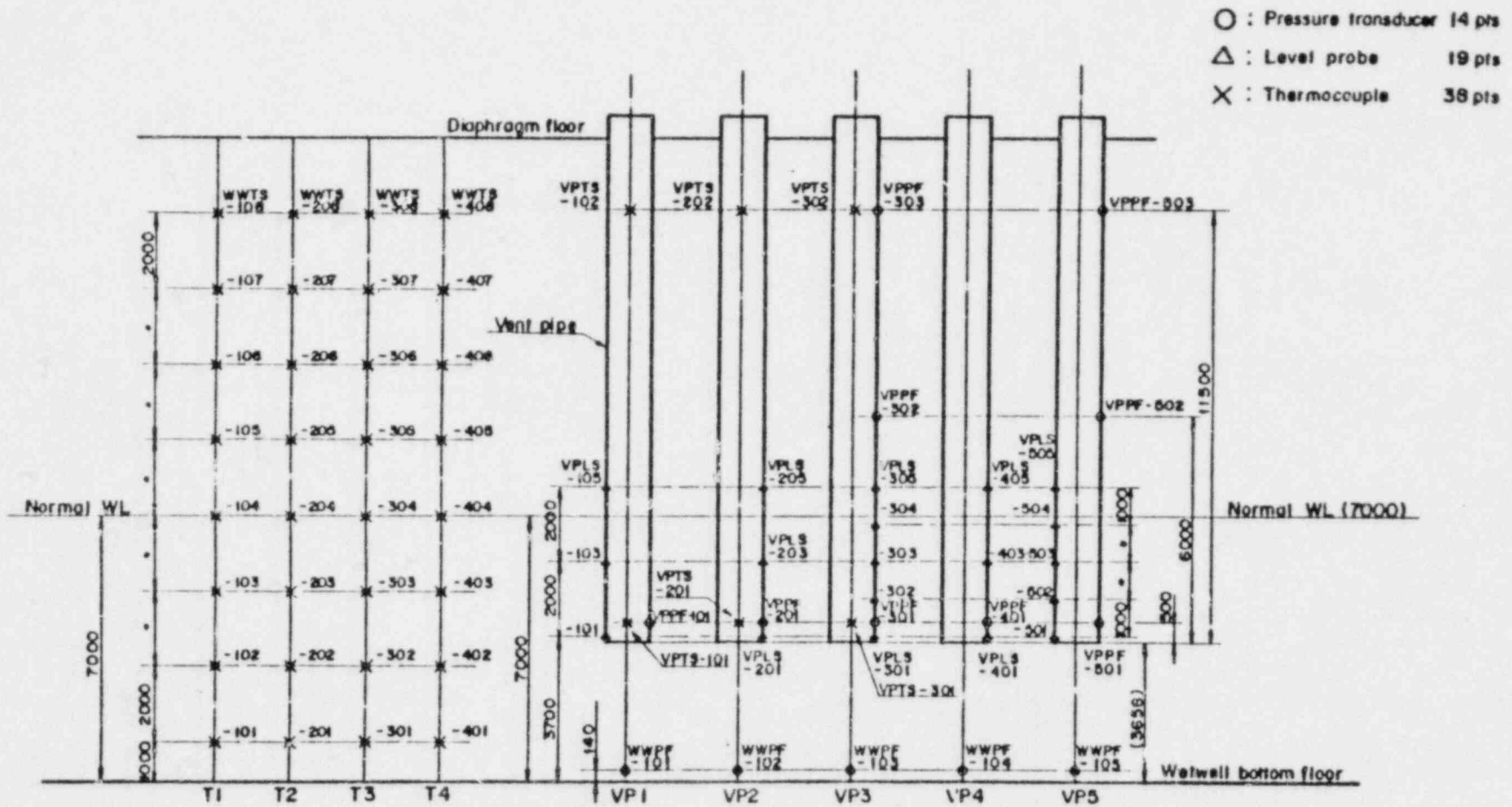
Figure A4-34. Locations of Pressure Transducers and WAter Level Probes for Vent Pipes, and Locations and Thermocouples for JAERI Wetwell
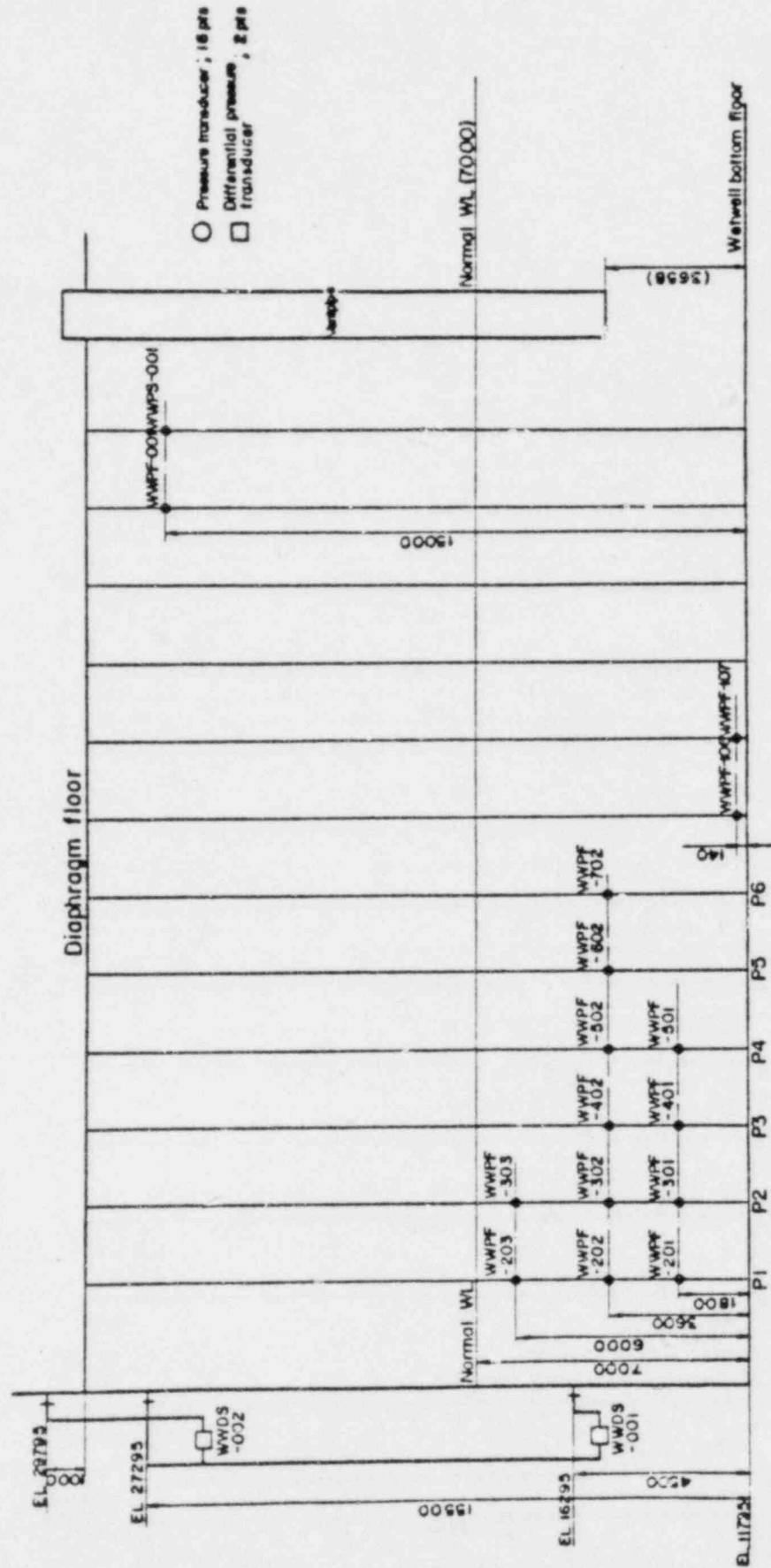
Figure A4-35. Locations of Pressure and Differential Pressure Transducers for JAERI Wetwell

The following Figures are General Electric Company Proprietary and have been removed from this document in their entirety.

A4-36   Vent Exit Elevation Pool Wall Pressures, JAERI Test 0002

A4-37   Average Vent Exit Elevation Pool Wall Pressure, JAERI
         Test 0002

A4-38   Calculated Steam Mass Flux and Air Content, JAERI
         Test 0002

A5. MULTIVENT CHUGGING

The primary objective of the Subscale Multivent Test Program was to demonstrate the bounding nature of single cell (i.e., single vent in an appropriate sized pool) pool wall pressures. The multivent data at 1/10 and 1/6 scale obtained in this test program are discussed in Subsection A5.2.

The observed reduction of pool wall pressure amplitudes in multivent geometries is due to the multivent effects - desynchrony of bubble collapses at individual vents and variation of the severity of bubble collapse, i.e., chug strength at individual vents in a multivent geometry. These multivent effects observed in the subscale multivent data are discussed in Subsection A5.2.

Available full-scale multivent data from the JAERI tests [Reference A6) are discussed in Subsection A5.3. These data also exhibit the multivent effects observed at subscale.

The response of the pool can be predicted in terms of pool acoustics using pool wall pressure data from tests where pool size and vent location in the pool were varied. It is also shown that multivent chugging pool wall pressure characteristics can be predicted by incorporating the multivent effects in an acoustic model of a multivent geometry.

A5.1 SUBSCALE MULTIVENT DATA

In the scaled Multivent Test Program five multivent geometries were tested (3, 7, and 19 vents at 1/10 scale and 3 and 7 vents at 1/6 scale). The multivent geometries were tested at the same conditions as the corresponding single vent geometries. As discussed in Section A4, the tests at prototypical test conditions (Mach scaled conditions) are only representative of expected chugging behavior at full-scale. Data from tests under prototypical test conditions will be discussed in the following subsections.

A5.1.1 Overall Multivent Chugging Characteristics

A5.1.1.1 General Characteristics

Data traces for the 1, 3, 7 and 19 vent 1/10-scale geometries are shown in Figures A5-1 through A5-4, respectively, at a steam mass flux of 4 $lbm/sec-ft^2$, 130°F pool temperature and zero air-content. The salient observation from these figures is that the pool wall pressure amplitudes are significantly lower in the multivent geometries.

However, apart from this reduction in wall pressure amplitudes, the overall characteristics of chugging in multivent geometries is similar to that in the single vent geometry, i.e., the condensation is intermittent as evidenced by the burst of oscillations in the vent static pressure and the depressurizations in the drywell pressure. Further, all bursts of condensation, while the water is out of the vents, produce a pool wall pressure oscillation, i.e., the pool wall pressure oscillations are produced by the rapid condensation and the resulting rapid acceleration and deceleration of the steam water interface (bubble collapse) at the vent exit in both single and multivent geometries.

The magnitudes of the vent static pressure oscillations are approximately the same for the single and multivent geometries. This indicates that the transient flow induced in the vent due to rapid condensation is approximately the same in single and multivent geometries.

The magnitude of the drywell depressurizations induced by the rapid condensation are somewhat smaller on the average in the multivent geometries than in the single vent geometries. This is to be expected because the rapid condensation is not synchronized and the condensation rate is not the same at all vents in the multivent geometries. Also, because the water motion in and out of the vent is controlled to a large extent by the drywell pressure fluctuations (see Subsection A4.1), the height of the water excursions into the vents are somewhat lower in the multivent geometries.

An examination of these data traces for the 1/6 scale, 1, 3 and 7 vent geometries [Reference A2] show that the observations made above from the 1/10-scale data also hold at 1/6 scale.

A5.1.1.2 Effect of System Conditions

Another measure of the similarity of chugging in single and multivent geometries is the behavior of the mean POP, PUP and chug frequency, i.e., average number of chugs per second with system conditions - steam mass flux, steam air-content and pool temperature. A comparison of the behavior of the mean POP, PUP and chug frequency for single and multivent geometries was presented in the two earlier data reports [Reference A1 and A2] and will be discussed only briefly here.

The variation of mean POP, PUP and chug frequency with steam mass flux for the 1/10 scale single multivent geometries is shown in Figures A5-5, A5-6, and A5-7, respectively. These figures show that the variation of mean POP, PUP and chug frequency with steam mass flux are similar for the single and multivent geometries. Both POP and PUP increase with increasing steam mass flux except for a dip around 4 $lbm/sec-ft^2$. The mean chug frequency increases linearly with steam mass flux.

The effects of pool temperature on mean POP and PUP for the 1/10 scale single and multivent geometries are shown in Figures A5-8 and A5-9. Again, the variation of mean POP and PUP is shown to be similar in single and multivent geometries. The mean POP peaks at some pool temperature while the mean PUP decreases continuously with increasing pool temperature. Pool temperature had no significant effect on the mean chug frequency in either the single vent or multivent geometries.

Increasing steam air-content reduces both mean POP and PUP in the single and multivent geometries as shown in Figures A5-10 and A5-11. Steam air-content had no significant effect on the mean chug frequency.

This similarity in the behavior of mean POP, PUP and mean chug frequency with system conditions between single and multivent geometries was also observed at 1/6 scale [Reference A2]. Therefore, the conclusion is that in general overall chugging characteristics in multivent geometries are similar to those in single vent geometries.

A5.1.2 Multivent Pool Wall Pressures

In the previous discussion (Subsection A5.1.1) the general characteristics of chugging are shown as being similar in single and multivent geometries. However, the magnitudes of the pool wall pressures were seen to be lower in multivent geometries. In this discussion, comparisons between single and multivent pool wall pressures will be presented. These comparisons are made in terms of the POP, mean square power (MSP) and PSDs. These three quantities are related to the intensity of the pool and vent responses caused by chugging. The POP is a measure of the intensity of the pool response produced by the impulsive excitation due to the steam "bubble" collapse. The mean square power (MSP) is a direct measure of the amplitude of the pool wall pressure oscillations, while the PSD gives a measure of the power by frequency in the pool wall pressures.

A convenient way to compare single and multivent data (such as POP and MSP) is in terms of the multivent multiplier. The multivent multiplier is simply the ratio of the value of a parameter (such as a mean POP) in a multivent geometry to the value in the single vent geometry. Figures A5-12 and A5-13 show the multivent multiplier based on mean POP at the pool bottom elevation for the 1/10 and 1/6 scale geometries. Note that by definition the multivent multiplier is unity for the single vent geometry. These figures show that the multivent multiplier is less than one for all the multivent geometries, i.e., the mean POP in the multivent geometries is less than that in the corresponding single vent geometry.

In the 1/10-scale geometries (Figure A5-12), the multivent multiplier drops rapidly going from the single vent to the 3 and 7 vent geometries, and then

increases for the 19 vent geometry. The increase in the multivent multiplier from the 7 to the 19 vent geometry is most likely due to the combined effects of the increased number of vents participating in a given pool chug and the increased number of spiky chugs occurring at individual vents in the 19 vent geometry. This will be discussed more later.

In the 1/6 scale geometries, the multivent multiplier is seen to decrease with an increasing number of vents, except for a steam mass flux of 8 lbm/sec-ft^2. At a steam mass flux of 8 lbm/sec-ft^2, the multivent multiplier increases slightly from the 3 to 7 vent geometry. Again, this increase is probably due to the same reasons given above for the increase of the multivent multiplier in the 1/10 scale 19 vent geometry.

Another multivent multiplier of interest is that based on maximum POP observed in single and multivent geometries. Figures A5-14 and A5-15 show the multivent multiplier based on maximum POP for the 1/10 and 1/6 scale geometries. Again, the multivent multiplier is seen as being less than unity, i.e., the maximum POP observed in a single vent geometry is bounding.

The POP is a measure of the initial response of the pool to the chug, and as will be shown later is a function of the pool modes excited. The mean square power (MSP) on the other hand is a measure of the intensity of the entire pool and vent response. Figures A5-16 and A5-17 show the multivent multiplier based on the average MSP (average MSP is the average value of MSP for all the chugs occurring in a test). These figures show that the average MSP decreases drastically in the multivent geometries and, again, the single vent value is clearly bounding.

Besides the reduction of the MSP in a multivent geometry, there is a rather marked change in the distribution of the power by frequency. Figures A5-18, A5-19, A5-20 and A5-21 show selected chugs and their PSDs from the 1/10 scale 1, 3, 7 and 19 vent geometries, respectively. These PSDs illustrate the general trend of power by frequency between the single and multivent geometries. In the single vent geometry, most of the power is in the vent harmonics

(approximately 50 Hz, 100 Hz, 150, Hz, etc.) and the first axial mode of the pool (between 300 Hz and 400 Hz). The spike at 960 Hz is due to line noise and will be removed in the final version of the figure. The lack of significant power at higher pool modes implies that the impulsive bubble collapse does not have frequency content high enough to excite the higher axial and radial pool modes (note that pool circumferential modes are not expected to be excited because of vent location in a single vent geometry).

The salient feature seen in the PSDs for chugs in the multivent geometries (Figures A5-19, A5-20 and A5-21) is the overall reduction in power over the entire frequency range. This is consistent with the reduction in mean square power discussed previously. Further, the power spreads out over a wider range of frequencies with increasing number of vents, i.e., more and more higher pool modes are excited. The lower overall power levels and the excitation of the higher pool modes in a multivent geometry are due to the two multivent effects - vents chugging out of phase and the variation in chug strengths at individual vents. A discussion of these multivent effects will be presented in Subsection A5.2. The consequence of these multivent effects on pool wall pressure characteristics will be discussed in Subsection A5.4 where it will be shown that the essential features of the multivent chug PSDs can be predicted using acoustic theory.

In summary, in terms of both POP and MSP, the pool wall pressures in the multivent geometries are less than those in the corresponding multivent geometries, i.e., single vent wall pressure amplitudes are bounding. PSDs of chugs in single and multivent geometries show that in the multivent geometries the power at the vent harmonics and lowest pool mode (first axial mode) is reduced. However, higher circumferential and radial pool modes are excited in the multivent geometries.

A5.2 MULTIVENT EFFECTS

The pool wall pressure characteristics in single and multivent geometries were previously discussed. The next logical question is what effects, i.e.,

multivent effects, occur in a multivent geometry that produce the observed
reduction in pool wall pressure amplitude and the type of pool response shown
by the PSDs. Two multivent effects were observed in the multivent geometries;
(1) bubble collapses at individual vents do not occur at precisely the same
time, i.e., out-of-phase bubble collapses, and (2) the magnitude of the pres-
sure impulses produced by the bubble collapses at individual vents are not
identical, i.e., the chug "strength" varies from vent to vent. The test data
demonstrating these multivent effects are presented in the following subsections.

A5.2.1 Vent Desynchronization

As discussed in Section 4 there are two distinct parts to a chug cycle. The
first part comprises the water motion in and out of the vent (referred to as
the gross chug) related to the recovery of the drywell pressure. The second
part is rapid condensation that occurs when the steam/water interface exits
the vent. The pool wall pressure oscillations of interest during chugging are
produced during the second part of the chug cycle due to the rapid condensation
induced motions of the steam/water interface and/or steam bubble collapse at
the vent exit.

The desynchronization discussed here will be relative to this rapid condensation/
bubble collapse part of the cycle at individual vents. Note that desynchroniza-
tion of this part of the cycle does not preclude the synchronization of the
gross chug part of the cycle because normally the period of the gross chug
(order of the period between chugs) is much larger than the period of the
rapid condensation/bubble collapse (order of tens of milliseconds). In fact,
it is expected and has been observed in both these subscale and the JAERI full-
scale tests that the gross chug cycle is in phase for the individual vents in
a multivent geometry whereas, the rapid condensation/bubble collapses at
individual vents are not.

As described in Section A3, a phasing algorithm was developed to determine the
occurrence of and the time at which bubble collapses occurred at individual
vents. The algorithm used the vent static pressure and vent water level in

individual vents to obtain these phasing data. Since only three vents were instrumented in the subscale multivent geometries tested, complete phasing data were obtained for the three vent geometries only. In a given three vent geometry test, this phasing algorithm was used to determine the percentages of chugs in which one, two or all three vents chugging (had rapid condensation/bubble collapse). In chugs consisting of two or three vents chugging the average time delay between the first and last vent to chug was also computed. These data have been reported earlier in Reference A1, however, a portion of these data will be briefly presented here again.

The percentages of chugs comprising of one, two and three vent chugs for the 1/10 scale three vent geometry are shown in Figures A5-22, A5-23 and A5-24, respectively. The lower steam mass fluxes seen as having a significant number of chugs caused by only one or two individual vents chugging. At higher steam mass fluxes all three vents chugged in almost all of the chugs. This trend was also found to occur in the 1/6 scale three vent geometry [Reference A1].

The delay times between the first and last vent to chug in the 1/10 scale 3 vent geometry for chugs in which two and three vents chugging are shown in Figures A5-25 and A5-26, respectively. In general, the average delay time was   seconds in the 1/10-scale geometry. The corresponding delay times in the 1/6-scale geometry were also around   seconds.

The important point to be noted here is that not all chugs were a result of chugs (bubble collapses) at all the individual vents. Also, the chugs at individual vents were not synchronized. As will be shown in Subsection 5.4, these multivent effects are responsible for the lower pool wall pressure amplitudes and PSD characteristics for chugs in multivent geometries.

A5.2.2 Variation of Chug Strengths at Individual Vents

Besides the non-synchronous chugs at individual vents the other multivent effect observed was that the strength of the bubble collapse and hence the magnitude of the resulting pressure spike varied from vent to vent. In the

previous section, it was shown that all vents did not participate in all the chugs observed in the 1/10 and 1/6-scale three vent geometries especially at the lower steam mass flux. This demonstrates that chug strengths vary from vent to vent for chugs where all vents do not participate.

A measure of the variation of chug strength from vent to vent in the subscale multivent geometries tested can be obtained by examining the pool wall pressures measured at the three different circumferential locations at the vent exit elevation. All test geometries had three transducers located 120° apart circumferentially at the vent exit elevation. In the multivent geometries, each of these pressure transducers was located close to a particular vent in the multivent geometry. Therefore, the amplitude of the POP measure at each circumferential location reflects to a large extent the chug strength at the vent closest to it (since pressure amplitude was found to vary inversely with distance between the vent and wall pressure measurement location [Reference A1]). For example, only if the chug strengths at all vents were identical, the peak overpressure (POP) measured at each of these three circumferential locations would be identical.

Figure A5-27 shows the pool wall pressures at the three circumferential vent exit elevation locations in the 1/6 scale 3 vent geometry. The steam mass flux was 8 lbm/sec-ft^2 and as determined from the vent static pressures over 80% of the chugs shown all three vents participated. This figure shows that the POPs at the three locations are different for individual chugs. Therefore, it can be concluded that the chug strength at individual vents varies.

Similar data from the 1/10 scale 19 vent geometry at a steam mass flux of 8 lbm/sec-ft^2 are shown in Figure A5-28. Again, from vent static pressure data for vents closest to each circumferential wall pressure measurement location it was determined that all these vents participated in the chugs shown. The POPs at the three different circumferential locations are seen as being different for individual chugs. Note that the variation of chug strength from vent to vent is expected to be stochastic to a large extent. Therefore, it is expected that for some chugs the chug strength at the three vents would be similar.

In summary, the two major multivent effects observed in the subscale multivent tests were that chugs (bubble collapses) at individual vents are desynchronized and vary in strength.

A5.2.3 Multivent Effects at Full-Scale

The mechanisms responsible for the multivent effects and the expected effects of scale on these mechanisms will be discussed in this subsection. Further, by using the JAERI full-scale multivent data it will be shown that these multivent effects also occur at full-scale.

A5.2.3.1 Mechanisms Causing Multivent Effects

As discussed earlier, a steam bubble is formed at the vent exit as the steam/ water interface is driven out of the vent due to drywell repressurization. The rate of bubble growth and hence the shape of the bubble at this point are primarily governed by the dynamics of the water motion out of the vent. The size to which the bubble grows is controlled by the time it takes to trigger the rapid condensation. Also as discussed earlier, the rapid condensation is triggered when the steam/water interface is sufficiently cooled down via turbulent convection in the pool, i.e., when the "blanket" of hot water surrounding the bubble is eroded away and cold water is exposed to the steam. Therefore, the time at which rapid condensation (and hence bubble collapse) is triggered depends on both the thickness of the hot water "blanket" surrounding the bubble and the rate of turbulent convection in the pool.

The thickness of the hot water "blanket" surrounding the steam/water interface as it exits the vent is a function of the amount of condensation and the turbulent convection occurring during the water motion in and out of the vent. The rate of turbulent convection in the pool depends on the intensity of the turbulence in the pool caused by both the water motion in and out of the vent as well as the water motion induced in the pool by rapid condensation during the preceding chug. In summary, the time at which bubble collapse is triggered and hence the size of bubble formed at the vent exit is a function of several strongly stochastic elements.

Consider the situation in a multivent geometry where the gross chug is synchronizea. i.e., water motion in and out of the vent is synchronized at individual vents. The steam/water interfaces at individual vents therefore exit the vent at nearly the same time and steam bubble start to form at individual vents. At some point rapid condensation is triggered at one of the vents.

Now an examination was made to determine if the start of rapid condensation and bubble collapse at this first vent can be communicated to and initiate bubble collapses at other vents. Communication between vents can occur either through the water in the pool or the steam space via the drywell. If communication between vents occurs via the pool, the delay time between bubbble collapses at individual vents should be of the order of acoustic propagation time in the pool. In the subscale 3 vent geometries this propagation time is of the order of a few milliseconds. The fact that the measured average delay times between bubble collapses at individual vents was found to be around 20 milliseconds precludes the communi tion via the pool as the mechanism triggering bubble collapses at other vents.

Communication via the steam space involves pressure waves generated due to rapid condensation at one vent causing pressure perturbations in other v_nts through the irywell. Because the drywell volume is much larger than the volume of a vent, the drywell acts as a large capacitance and does not allow effective communication between vents. This is borne out in the tests of the 3 vent subscale geometries with oversized drywell volumes where no significant change was found in the measured average delay time between bubble collapses at individual vents. Therefore, communication via the steam space is not a plausible mechanism for synchronization of bubble collapses at individual vents. Note that even if communication via the pool or steam space were possible mechanisms for synchronization of chugs at individual vents it would be expected that the delay times would go up with scale since the acoustic propagation paths increase.

The most plausible mechanism for bubble collapse at individual vents at this point, appears to be the turbulent convection in the pool. This means that

bubble collapses at individual vents are triggered by local turbulent convection rates at each vent. Unfortunately, there is not enough data on the pool turbulence to conclusively demonstrate this in terms of the measured delay times. Nonetheless, postulating that local turbulent convection is the mechanism triggering bubble collapse does explain certain observed facts. First, due to the stochastic nature of turbulence, the delay times between bubble collapses would vary significantly around some value related to the mean time scale of the turbulence. The delay time data do indeed show a wide variation in the delay times from chug to chug - the standard deviation is of the order of the mean value [Reference A1].

Second, due to the stochastic nature of turbulence, the time at which rapid condensation and hence bubble collapse is triggered varies from vent to vent. This implies that the size of the bubble formed before collapse starts, will also vary from vent to vent. Therefore, the chug "strength" will vary from vent to vent as was indeed observed in the data (Paragraph A5.2.2).

The variation of the delay time for bubble collapses between vents with scale would depend on how the pool turbulence characteristics would vary with scale. Generally, the average eddy size determines the time scale of the turbulence [Reference A21]. In the type of mechanisms generating turbulence in the pool (water motion in and out of the vent for example) it is expected that the mean eddy size is related to the vent diameter. Therefore, the time scale of the turbulence should increase with scale and hence in turn, the average delay time between bubble collapses at individual vents is also expected to increase. Since randomness is an inherent feature of turbulence, significant variation in the delay times as well as chug strengths at individual vents are expected to persist at full-scale.

A5.2.3.2 Multivent Effects at Full-Scale

Recently some data have become available from the Mark II prototypical full-scale 7 vent tests performed at JAERI [Reference A6]. Specifically, expanded time plots for pool and vent pressures are available for JAERI Tests 0002, 2101 and 3102. An examination of these expanded time plots show that the

multivent effects observed in the subscal tests also occur at full-scale.
Selected data showing the multivent effec. will be presented in the following.

Five of the seven vents in the JAERI multive geometry were instrumented for
the measurement of vent static pressure and \ ter level (see Figure A4-34).
The vent static pressure and vent water level data for these five vents were
ana' 'zed using the procedure described in Subsection A2.4 to determine the
time at which bubble collapses occurred at each of these vents.

Figure A5-29 shows the vent exit static pressures for the five vents (vents
1, 2, 3, 4, and 5 - see Figure A4-34) for a large chug occurring at around
    seconds in Test 000'. Using the vent water level data, the duration that
the water was out of the vent is also shown in Figure A5-29. As described in
Subsection A2.4, the time of occurrence of the spike produced by the bubble
collapse at each vent was taken to be the time of the minima in the vent static
pressure while the water was out of the vent and is indicated in Figure A5-29.

The bubble collapses are not seen as occurring simultaneously at the five
vents. Bubble collapse occurred at Vent 5 first and at Vent 2 last. The
delay time between Vent 5 and Vent 2 is about   msec.

A similar analysis was performed on several other large chugs and. as expected,
the bubble collapses at the five instrumented vents were desynchronized and
the delay time between the first and last vent to chug (desynchronization win-
dow) was varied considerably from chug to chug. Although all the available
data have not been analyzed yet, it appears that the mean value for this
delay time is greater than 50 milliseconds in these full-scale tests.

The second multivent effect (variation of chug strengths at individual vents)
was also observed in these full-scale data. As described in Paragraph A4.4.2,
there are several pool wall pressure transducers that are located near the
exits of different vents in the JAERI facility. Specifically, transducers
WWPF202, 302, 602 and 702 are located at the vent exit elevation next to
vents 2, 3, 4 and 7, respectively (see Figures A4-33 and A4-35). The pressure

amplitudes measured by these transducers reflect the chug strengths at vents closest to them.

The variation of chug strengths at individual vents is shown in Figure A5-30. The pool wall pressures at the vent exit elevation for a chug occur at 62.5 seconds in JAERI Test 0002. In this chug event a high amplitude chug occurred at Vent 7 as indicated by the large pressure spike at WWPF702. The other vents had relatively smaller chugs. Keep in mind that the variation of chug strengths from vent to vent is stochastic in nature and that not all pool chugs will exhibit the large variation seen in Figure A5-30. Nonetheless, varying degrees of variation in chug strengths from vent to vent were found in all the chugs from Tests 0002, 2101, and 3102 for which expanded time traces are available.

In summary, the multivent effects observed in the subscale multivent tests were also found to be present in the JAERI full-scale multivent tests, as expected from the previous discussion.

A5.3 ANALYSIS OF MULTIVENT CHUGGING

In previous discussions the multivent data were presented showing the chug pool wall pressure characteristics and multivent effects that occur in multivent geometries during chugging. Here the data will show that the multivent pool wall pressure characteristics can be explained by acoustic analyses that take into account the observed multivent effects. Using data obtained from special single vent tests where the pool size and vent location were varied, it will be shown that the pool response during chugging can be modeled using acoustic theory. Following this, the multivent pool wall pressure will be predicted using acoustic models for the multivent geometries and shown that the overall pool wall pressure data trends can be adequately predicted.

A5.3.1 Pool Response Dynamics

Several special single vent tests were performed in the Scaled Multivent Test
Program to provide data which would help in understanding the mechanics of
propagation of the chug-induced pressure waves in the pool and in the under-
standing of the pool response to multivent chugging. The obvious difference
between the single and multivent pool is that the multivent pool is larger,
and although the pool area per vent is the same, if vents chug out of phase,
each vent effectively "sees" a larger pool in a multivent geometry. The
other difference is that while the vent in a single vent geometry is located
along the vertical axis of the pool, the majority of the vents in a multivent
geometry are not. Therefore, circumferential modes, which cannot be excited
to any significant extent in a single vent geometry, are expected to be excited
in multivent geometries.

Recognizing these differences several tests were performed in the Scaled Multi-
vent Test Program to determine the effect of pool size and vent location on
the response of the pool and the resulting pressures at the pool wall. To
obtain the pool size effects, a 1/10-scale single vent was tested in a 18-in
diameter pool (the 1/10 scale 3 vent pool) and a 30-in diameter pool (see
Subsection A3.1). The 10-in diameter pool (the 1/10-scaled pool) was also
tested. The effects of vent location in the pool were obtained from tests
where the 1/10 scale vent was located off axis in the 18-in and 30-in diameter
pools (see Section A3.1).

The results from these tests were presented in the Phase 1 test report [Refer-
ence A1]. These results are compared here against the predictions from acoustic
models of the pool. The acoustic analysis used is identical to that developed
in the Mark II Generic Program [Reference A20]. The pool is modeled as an
acoustic cavity and the chug forcing function is modeled as a volumetric
source in the pool at the exit location of the vent(s). The acoustic wave
equation is solved using the Green's function method and the solution for the
pressure at any location in the pool or at the pool walls is of the form [20]:

$$p(\vec{r},t) = \int_0^{t+} dt_0 \int_V dV_0\ G(\vec{r},t/\vec{r}_0,t_0) q(\vec{r}_0,t) \tag{A5-1}$$

where

$$p(\vec{r},t) = \text{pressure in the pool at location } r \text{ and time } t,$$
$$q(\vec{r}_o,t) = \text{time dependent volumetric source located at } r_o$$
$$G(\vec{r},t/\vec{r}_o,t_o) = \text{time dependent Green's function.}$$

The Green's function can be expressed in terms of the pool eigenmodes [Reference A22] and for a cylindrical pool with a single vent, Equation A5-1 can be written as:

$$p(\vec{r},t) = \frac{24\rho c^2}{D_w L} \sum_n \frac{\Omega_N(\vec{r}_o)\Omega_N(\vec{r})}{\omega_n \Lambda_n} \int_0^{t+} \beta(\omega_n,t_o) \, S(t_o) \, \sin[\omega_n(t-t_o)] \, dt_o \quad (A5-2)$$

where

$$\rho = \text{density of the fluid in the pool (water)}$$
$$c = \text{pool acoustic speed}$$
$$D_w = \text{pool diameter}$$
$$L = \text{pool depth}$$
$$\Omega_N(\vec{r}_o), \Omega_n(\vec{r}) = \text{pool eigenfunctions}$$
$$\omega_n = \text{frequency of the } n^{th} \text{ pool mode}$$
$$\Lambda_n = \text{integration constant}$$
$$\beta(\omega_n,t_o) = \text{pool damping function}$$
$$S(t_o) = \text{volumetric point source at location } \vec{r}_o$$

The series summation and the time integral in Equation A5-2 were evaluated numerically. The point source $S(t_o)$ was taken to be a triangular impulse representing the bubble collapse component and a sinusoid representing the vent first harmonic component [Reference A20].

Figure A5-31 shows the effect of pool size on the mean POP. In this figure, the mean POP has been normalized by the mean POP measured in the smallest

pool - the 1/10-scale pool. The mean POP decreases as the pool size is
increased. Also shown on this figure are the trends predicted from acoustic
analyses discussed earlier. The predictions were performed using sources with
different widths τ_p for the triangular impulse part of the source - the fre-
quencies of the vent harmonics were not varied since vent lengths were kept
constant between geometries. The width of the triangular impulse τ_p was
normalized by the axial acoustic propagation time τ_a for the pool ($\tau_a = L/c$).

It is seen that the $\tau_p/\tau_a > 1$, the predicted decrease in POP is inversely pro-
portional to pool area, i.e., D_w^2. This is because when the impulse is broad
the pool responds in essentially a static fashion* or at most only the axial
pool modes are excited. For this case it can be seen from Equation A5-2 that
the pressure amplitude is inversely proportional to D_w^2, since the pool depth
L was kept constant and the speed of sound was assumed to be constant in the
different pools. This $1/D_w^2$ dependency of mean POP compares well with the
data at lower mass fluxes where the POP is lower [Reference A1] and many oscil-
latory chugs (having frequency contents predominantly at the vent first har-
monic) are observed. Note that due to the greater flexibility of the larger
pools, the pool sonic velocity in fact might be decreasing somewhat with pool
size. This probably explains why some data decrease faster than $1/D_w^2$ as seen
in Figure A5-31.

Now as τ_p/τ_a is decreased, that is, as the triangular impulse width is made
smaller at a given pool sonic velocity, the decrease in POP with pool size
is slower than $1/D_w^2$ as seen in Figure A5-31. This is because the sharper
impulse is able to excite the radial modes** in the larger pool where the fre-
quency of the radial modes is lower. It appears that τ_p/τ_a of   best pre-
dicts the data trends at the higher steam mass fluxes where predominantly
spiky chugs having large POPs were observed [Reference A1]. Finally, in the
limit that τ_p/τ_a goes to   , the impulse propagates initially as a pure

---

*The vent harmonic frequencies are well below the first pool mode and there-
fore the pool responds to these also in a static fashion.
**Due to the vent location at the pool vertical axis, circumferential modes
cannot be excited to any significant extent.

spherical wave and the expected variation in POP in this case would be as 1/D. Note that all the data are well below the 1/D trend (see Figure A5-31) indicating that the duration of pressure impulse produced by the bubble collapse is not short enough so that τ_p/τ_a approaches zero.

In summary, the effect of increased pool size is to reduce the pool wall pressure amplitudes and this trend can be predicted quite well using acoustic analyses of the pool response.

Next, the effect of vent location on pool wall pressure magnitudes are examined. As mentioned earlier, several tests were performed with the vent being offset varying amounts from the vertical axis of the pool. In these tests, the vent was offset such that it moved closer to the pressure transducers located at the 0° circumferential location as shown schematically in Figure A5-32. Note that the pressure transducers at the pool bottom, mid-clearance, vent exit and mid-submergence were all located at the 0° circumferential location. Therefore, offsetting the vent moved it closer to all these transducer locations. There were two additional pressure transducers located on the pool walls at the 120° and 240° locations at the vent exit elevation and offsetting the vent moves its exit away from these transducers.

The effect of vent offset on the mean POP at the vent exit elevation 0° circumferential location is shown in Figure A5-33. These data were from the tests performed in the 30-in diameter wetwell with the vent located at the vertical axis of the pool (zero offset), and with offsets of six to ten inches. The mean POP has been normalized by the mean POP at the same vent exit elevation in the scaled 1/10-scale vent geometry (the 1/10-scale vent centered in the 10-in diameter pool). Note that for the 10 in. offset in the 30-in vessel, the distance (5-in) between the vent and the 0° circumferential location is the same as that with the centered vent in the 1/10-scale wetwell (see Figure A5-34).

Figure A5-33 shows that the mean POP increases as the vent offset is increased, i.e., the vent is moved closer to the measurement location. This trend is most

marked for the higher steam mass fluxes. Also shown on this figure are the predictions from the acoustic analyses discussed earlier.

For $\tau_p/\tau_a > 1$, there is not much variation in mean POP with vent offset. This is to be expected since the variation of mean POP with vent offset is caused due to the response of the radial modes of the pool. Now for a pulse with $\tau_p/\tau_a > 1$, the frequency content is not high enough to excite the radial modes to any significant extent and hence very little variation with vent offset occurs. The close agreement between data at the lower steam mass fluxes and predictions with $\tau_p/\tau_a > 1$ shows that the chug source for these low steam mass fluxes does not have much high frequency content. This is consistent with the small POPs and a large number of oscillatory chugs with frequency content limited mainly to the first vent harmonic, are observed [Reference A1].

The higher steam flux (>8 lbm/sec-ft^2) data trends are more closely predicted with impulse having τ_p/τ_a of 0.45 which has sufficient frequency content to excite the radial pool modes. Hence, the narrow impulse produce the type of radial variation observed in the higher steam mass flux data.

Finally, to determine the combined effects of pool size and vent location, data from tests run in the three geometries shown in Figure A5-34 are examined. Figure A5-34 shows that in these three geometries, the pool size was varied and the vent offset was chosen such that the distance between the vent and pool wall locations at the 0° degree circumferential location was held constant at five inches.

Figure A5-35 shows the variation of mean POP with pool size at the 0° circumferential vent exit elevation location (distance between the location and the vent is constant at five inches for the three geometries). The mean POP has been normalized by the mean POP in the 1/10 scale single vent geometry. This figure also shows that the mean POP decreases with increasing pool size. This decrease with pool size is nearly the same as that previously shown in Figure A5-31 for the lower steam mass fluxes (>4 lbm/sec-ft^2), i.e., for these low steam mass fluxes, vent location effects are not important (consistent with the very small effect seen in Figure A5-33).

At the two higher steam mass fluxes, it is again seen that the mean POP decreases with pool size. However, the decrease is smaller than that previously show. in Figure A5-31 due to pool size alone. This indicates that for these higher steam mass fluxes, the vent location does effect the pool wall pressure to a significant extent. This is again consistent with the vent offset effect discussed earlier and shown in Figure A5-33.

The predicted variations in mean POP using acoustic analyses are also shown in Figure 5-35. As expected, the variation of mean POP is best predicted by impulses with τ_p/τ_a 1 for the lower steam mass fluxes. Whereas, for the higher steam mass flux data, shorter impulses with τ_p/τ_a of 0.45 best predict the data trends.

Besides demonstrating that the pool response to chugging can be predicted quite well with acoustic models of the pool, the pool wall pressure trends provide valuable insights on the observed multivent pool wall pressure trends. The data trends discussed above show that for the types of pool responses excited by chugging, the POP decreases with increased pool size irrespective of vent location in the pool. Therefore, with the observed desynchronized bubble collapses at individual vents (that is, individual vents effectively chugging in a larger pool) this pool size effect will result in lower wall pressure amplitudes in a multivent geometry.

This can be clearly illustrated by comparing the data from the geometry with a single 1/10-scale vent centered in the 18-in wetwell and the 1/10-scale 3 vent geometry which had 3 1/10-scale vents in the same 18-in wetwell. Figure A5-36 shows this comparison and it is seen that the mean POPs for the two geometries show a good agreement. This agreement shows that the observed reduction in pool wall pressures in a multivent geometry is due to the pool size effect with the vents chugging out of phase.

A5.3.2 Predictions of Multivent Pool Wall Pressures

In the previous section, it was shown that the observed pool responses to chugging can be predicted quite well using acoustic models of the pool. In

this section, acoustic models of the multivent geometries are used to show
that the multivent pool wall pressure trends can also be predicted.

A5.3.2.1 Methodology

Using the fact that the acoustic equation is linear the single vent acoustic
model discussed in the previous section was extended to a multivent geometry
in a straightforward manner. Instead of a single source in the case of the
single vent geometries multiple sources were placed in the multivent pool at
the exit locations of the individual vents. The pressure at any point $\vec{r}$ in
the pool or at the pool l due to one of these multiple sources at $\vec{r}_o$ was
calculated using Equation A5-2. The pressure at $\vec{r}$ due to multiple sources was
then obtained by a linear superposition of the pressure at that location to
each of the multiple sources. That is, for n sources

$$p(\vec{r},t) = \sum_n p_n(\vec{r},t)$$

(A5-3)

where $p_n(r,t)$ is the pressure at $\vec{r}$ due to the nth source and is given by
Equation A5-2.

Acoustic models of the 1/10-scale single and multivent geometries tested in
the Scaled Multivent Test Program (see Subsection A3.1), were constructed. A
simple baseline source was selected consisting of a triangular impulse of width
τ_p and one 50 Hz sinusoid representing the vent component. The amplitudes of
the triangular impulse and the sinusoid were chosen so as to give a POP of
50 psi and the average vent ringout amplitude in the 1/10-scale single vent
geometry.

The purpose of these analytical studies was not to formulate or justify a par-
ticular method for deriving multivent pool wall loads, but only to understand
the observed multivent pool wall pressure characteristics and data trends.
The simple source selected reflects this and consists of components necessary
to model only the essential features - impulse generated by the bubble col-
lapse and the first vent harmonic which is generally the dominant vent component--

of the chug source. Hence, no attempt was made to model the underpressure preceding the bubble collapse and higher vent harmonics (although these can be modeled with a more complex source).

The two multivent effects observed--desynchronization of chugs and variation of chug strengths at individual vents--were included in this multivent acoustic analysis. Desynchronization of the chugs was implemented by starting the sources at various vent locations at different times. The start times for chugs at individual vents were selected randomly within a desynchroniza- tion time window. Specifically, if τ_w is width of the desynchronization window, the time at which the source was started at an individual vent was determined by picking a random number between 0 and τ_w.

The variation of chug amplitudes from vent to vent was implemented by first assuming an amplitude distribution (normalized by the mean value) and then selecting amplitude factors at random for each vent in the multivent geometry from this distribution. The source at a given vent is then obtained by multiplying the standard source by the amplitude factor for that vent.

Therefore, implementing vent desynchronization and chug amplitude variation for a chug in the multivent geometry required making a random selection of source start times from a given desynchronization window and amplitude factors from a specified amplitude distribution function. Using these start times and amplitude factors for the sources at the individual vents, the pressure time history at a given pool location was then computed using Equa- tions A5-2 and A5-3. Generally, 20 such chug pressure time histories were computed and mean values of quantities such as POP and mean square power (MSP) were computed.

A5.2.2 Analytical Predictions

First, consider the case where identical sources are placed in-phase at all vents. Figure A5-37 shows the resulting pressure traces at the pool bottom elevation for the 1/10-scale 1, 3, 7 and 19 vent geometries. This figure shows that for all the geometries, the pressure traces are virtually identical.

The PCP (value shown on each corresponding pressure trace) is also virtually identical in all geometries - the minor variations are caused by the small differences in the pool to vent area ratios for the various geometries. The corresponding PSDs are shown in Figure A5-39. Again, it is seen that the PSDs are virtually identical and the only pool mode excited is the first axial mode in all the geometries.

This result demonstrates that with all vents in-phase and identical sources at each vent, the single and multivent pool wall pressures are identical; i.e., in the largest pool wall pressures observed in a single vent geometry to occur in a multivent geometry requires that the big chug occur at all vents and in-phase at all vents. This is extremely unlikely given the randomness involved in both the time of bubble collapse and strength of the bubble collapse at individual vents in a multivent geometry. In fact, as shown in Subsection A5.1, the maximum pool wall pressure amplitudes observed in a multivent geometry are considerably lower than those in the corresponding single vent geometry. Therefore, all vents in-phase with identical sources do not represent any observed multivent data.

Second, consider the case where all the vents are in-phase, but the source strength varies from vent to vent. In this case it was assumed that the distribution of the source strengths from vent to vent in a multivent geometry was the same as the variation in the POP of successive chugs in the single vent geometry, i.e., the spatial distribution of chug strengths in a multivent geometry was the same as the temporal distribution in a single vent geometry. At present, there is no concre justification for this assumption except that since the temporal distribution of POPs in a single vent geometry is available, it is easy to implement.

Pressure time histories were computed for 50 chug events in the 1/10-scale 3 vent geometry. In each chug event amplitude factors (normalized POP amplitudes) were selected randomnly for each of the three vents from the normalized (by the mean value) temporal distribution of POPS for the first 100 chugs that occurred in the 1/10-scale single vent test (steam mass flux 8 lbm/sec-ft^2, pool temperature 130°F and zero steam air-content). As described earlier,

the source amplitude at a given vent was obtained by multiplying the amplitude of the standard source by the amplitude factor selected for that vent.

The mean and maximum POPs for the 50 computed chug events in the 1/10-scale 3 vent geometry were   psi and   psi, respectively. The corresponding mean and maximum POPs for the 1/10-scale single vent geometry (using the same amplitude distribution) were 50 psi and 180 psi respectively. Therefore, the average POP in the three vent geometry is nearly the same as that for the single vent geometry in this case. However, the maximum POP is   )-stantially lower in the three vent geometry than in the single vent geometry. Similar results were obtained when similar computations were performed in the 7 and 19 vent geometries with the exception that the maximum POP decreased with increasing number of vents.

The main implication of these results is that one of the reasons why the maximum POP measured in a multivent geometry lower than that in a single vent geometry is   ) to the variation of chug strengths at individual vents. Also, the average POP in the multivent geometry where all vents are in-phase will be equal to the mean value of the amplitude distribution assumed for the spatial variation of chug strengths from vent to vent.

Next, the effects of desynchronized chugs at individual vents in a multivent geometry are examined. Identical sources were applied in the single vent geometry and at individual vents in the multivent geometries, except that the sources were desynchronized in the multivent geometry. As described earlier, the sources at individual vents were desynchronized randomly within a desynchronization window. To start with the width of the desynchronization window was taken to be   seconds which was the average delay time between the first and last vent to chug in the 1/10 and 1/6-scale 3 vent geometries (Subsection A5.2).

Pressure time history at the pool bottom elevation (same as the transducer location at this elevation in the test geometries) was computed for 20 chug events in each of the three 1/10 scale multivent geometries (3, 7 and 19 vents). Each chug event involved selecting start times for individual vents

randomly within the 0.02 second desynchronization window and then obtaining the pressure time history using Equations A5-2 and A5-3.

Figure A5-39 shows the multivent multiplier based on the mean POP at the pool bottom elevation for the 20 computed chug events. The multivent multipliers have been computed for several values of τ_p/τ_a.* This figure shows that the multivent multiplier is less than unity for the multivent geometries. The multivent multipliers based on mean POP obtained from actual test data are also shown in Figure A5-39. It is seen that the predicted multivent multipliers compare reasonably well with the actual data for the 19 vent geometry. Generally, the predicted values are higher than the measured values for the 3 and 7 vent geometries. The most probable reason for this overprediction of the multivent multiplier in the 3 and 7 vent geometries is that th   ug strengths at individual vents in these geometries were less ti   average chug strength in the single vent geometry. Note that in the analysis the same source and hence the same chug strength is used in the single and multivent geometries. The only reduction therefore in the multivent pool wall pressures comes about due to phasing.

Figure A5-40 shows the comparison between predictions and data for the multivent multipliers based on average mean square power (MSP). As before, the predicted multivent multipliers are somewhat higher than the measured values, but predict the data trends quite well.

Figures A5-41 through A5-44 show typical computed pressure time histories and their PSD's in the 1/10-scale single and multivent geometries. Note that as discussed earlier no effort was made to model the underpressure preceding the pressure spikes and therefore none of the computed pressure time histories exhibit the initial underpressure. The impulse width was chosen such that τ_p/τ_a was 0.45.

In the single vent geometry (Figure A5-41), the pressure time history clearly shows the classical pool ringout (first axial pool mode being the dominant

---

*τ_p is the width of the triangular impulse and τ_a is axial propagation time in the pool (that is, pool depth divided by the pool sonic velocity).

mode excited) with the vent ringout (at 50 Hz) superimposed on it. The PSD therefore shows dominant spikes at 50 Hz and 375 Hz (pool first mode frequency).

In the 3 and 7 vent geometries (Figures A5-42 and A5-43) the pressure time histories show that the pressure amplitudes have dropped compared to the single vent geometry, and higher frequencies appear in the time trace. This is reflected in the PSDs which show that the overall power is lower and several bumps are present at higher frequencies indicating that higher pool modes are excited. Nonetheless, the first pool axial mode is still dominant.

Finally, in the 19 vent geometry (Figure A5-44), the pressure trace shows a significant high frequency content and the first axial pool mode is no longer clearly evident. The PSD shows that the power in the first axial mode around 375 Hz has decreased considerably and higher pool modes (mainly radial and circumferential modes) are quite prominent. Although, the overall power is quite small compared to that in the single vent geometry (Figure A5-41).

Subsequently vent desynchronization reduces the overall power while spreading it into the higher pool modes. This is exactly the trend observed in the actual data as discussed in Subsection A5.1. Therefore, it can be concluded that the key multivent effect is vent desynchronization in that is is mainly responsive for the observed multivent pool wall pressure characteristics. The variation of the chug amplitudes from vent to vent on the other hand acts to mainly enhance the effects caused by vent desynchronization and make it highly improbable for large chugs to occur simultaneously at all vents.

The following Figures are General Electric Company Proprietary and have been removed from this document in their entirety.

A5-1   Data Traces, 1/10 Scale Single Vent Test

A5-2   Data Traces, 1/10 Scale 3 Vent Test

A5-3   Data Traces, 1/10 Scale 7 Vent Test

A5-4   Data Traces, 1/10 Scale 19 Vent Test

A5-5   Variation of Mean POP at Pool Bottom Elevation With Number of Vents, 1/10 Scale Single and Multivent Tests

A5-6   Variation of Mean PUP at Pool Bottom Elevation With Number of Vents, 1/10 Scale Single and Multivent Tests

A5-7   Variation of Mean Chug Frequency With Number of Vents, 1/10 Scale Single and Multivent Tests

A5-8   Variation of Mean POP at Pool Bottom Elevation With Number of Vents, 1/10 Scale Single and Multivent Tests

A5-9   Variation of Mean PUP at Pool Bottom Elevation With Number of Vents, 1/10 Scale Single and Multivent Tests

A5-10   Variation of Mean POP at Pool Bottom Elevation With Number of Vents, 1/10 Scale Single and Multivent Tests

A5-11   Variation of Mean PUP at Pool Bottom Elevation With Number of Vents, 1/10 Scale Single and Multivent Tests

A5-12   Multivent Multiplier (Mean POP) at Pool Bottom Elevation, 1/10 Scale Single and Multivent Tests

A5-13   Multivent Multiplier (Mean POP) at Pool Bottom Elevation, 1/6 Scale Single and Multivent Tests

A5-14   Multivent Multiplier (Maximum POP) at Pool Bottom Elevation, 1/10 Scale Single and Multivent Tests

A5-15   Multivent Multiplier (Maximum POP) at Pool Bottom Elevation, 1/6 Scale Single and Multivent Tests

A5-16   Multivent Multiplier (Mean Square Power) at Pool Bottom Elevation, 1/10 Scale Single and Multivent Tests

A5-17   Multivent Multiplier (Mean Square Power) at Pool Bottom Elevation, 1/6 Scale Single and Multivent Tests

The following Figures are General Electric Company Proprietary
and have been removed from this document in their entirety.

A5-18   Pressure Time History and PSD for a Chug in the 1/10 Scale
         Single Vent Geometry

A-   Pressure Time History and PSD for a Chug in the 1/10 Scale
         3 Vent Geometry

A5-20   Pressure Time History and PSD for a Chug in the 1/10 Scale
         7 Vent Geometry

A5-21   Pressure Time History and PSD for a Chug in the 1/10 Scale
         19 Vent Geometry

A5-22   Percent of One Vent Pool Chugs 1/10 Scale 3 Vent Tests

A5-23   Percent of Two Vent Pool Chugs, 1/10 Scale 3 Vent Tests

A5-24   Percent of Three Vent Pool Chugs, 1/10 Scale 3 Vent Tests

A5-25   Average Time Delay Between the First and Last Vent to
         Chug in Two Vent Pool Chugs, 1/10 Scale 3 Vent Tests

A5-26   Average Time Delay Between the First and Last Vent to
         Chug in Three Vent Pool Chugs, 1/10 Scale 3 Vent Tests

A5-27   Vent Exit Pool Wall Pressures at Three Circumferential
         Locations, 1/6 Scale 3 Vent Geometry

A5-28   Vent Exit Pool Wall Pressures at Three Circumferential
         Locations, 1/10 Scale 19 Vent Geometry

A5-29   Vent Exit Static Pressures for a Chug from JAERI Test 2101

A5-30   Vent Exit Elevation Pool Wall Pressures for a Chug from
         JAERI Test 0002

A5-31   Variation of Mean PCP at Pool Bottom Elevation (Normalized
         by Mean PCP in 10 inch Wetwell) with Wetwell Size (130°F
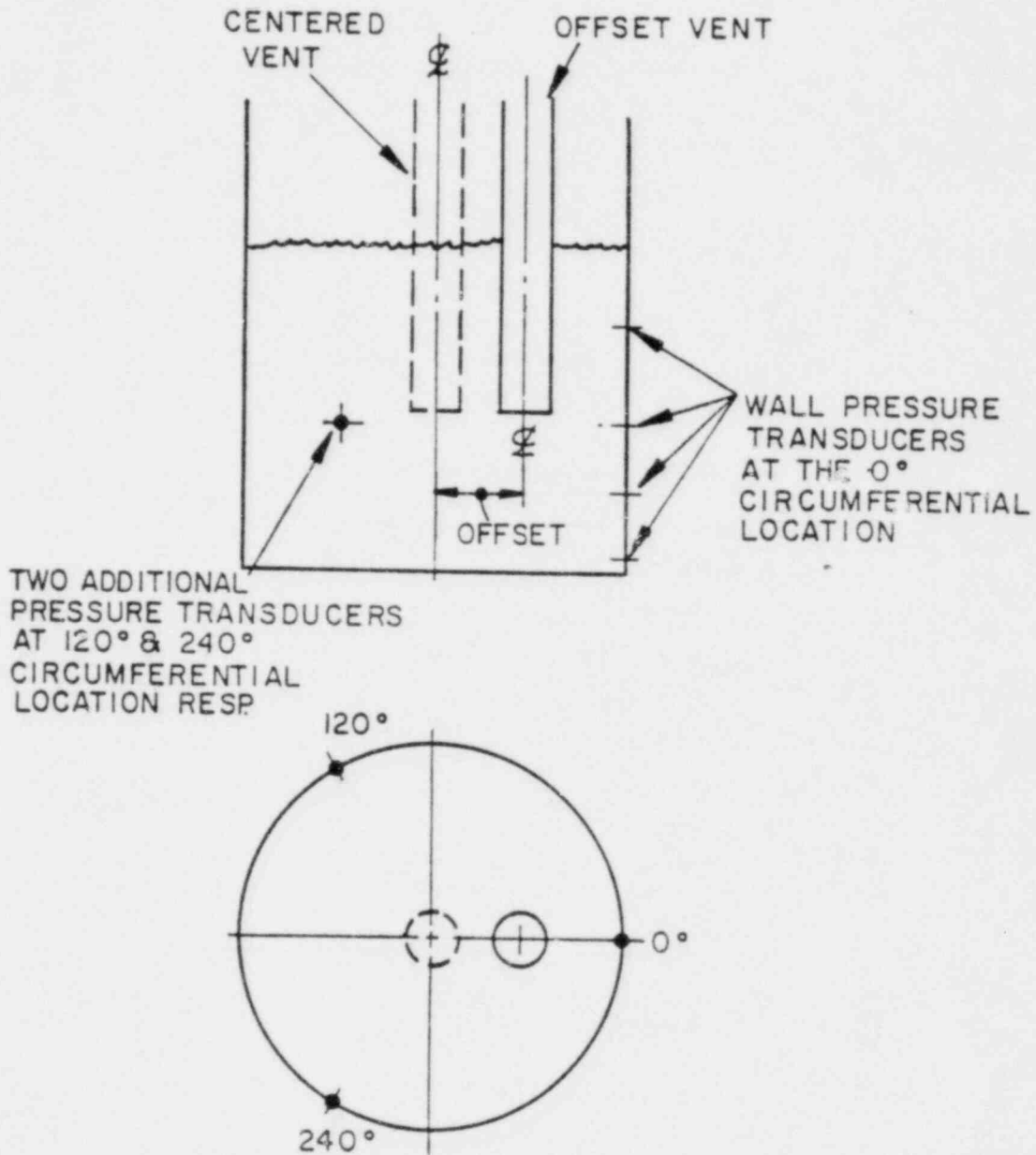   Pool Temperature), 1/10 Scale Single Vent Tests

Figure A5-32. Schematic of Vent Offset

This figure is General Electric Company Proprietary and has been removed from this document in its entirety.

A5-33   Effect of Vent Offset on Vent Exit Elevation Pool Wall
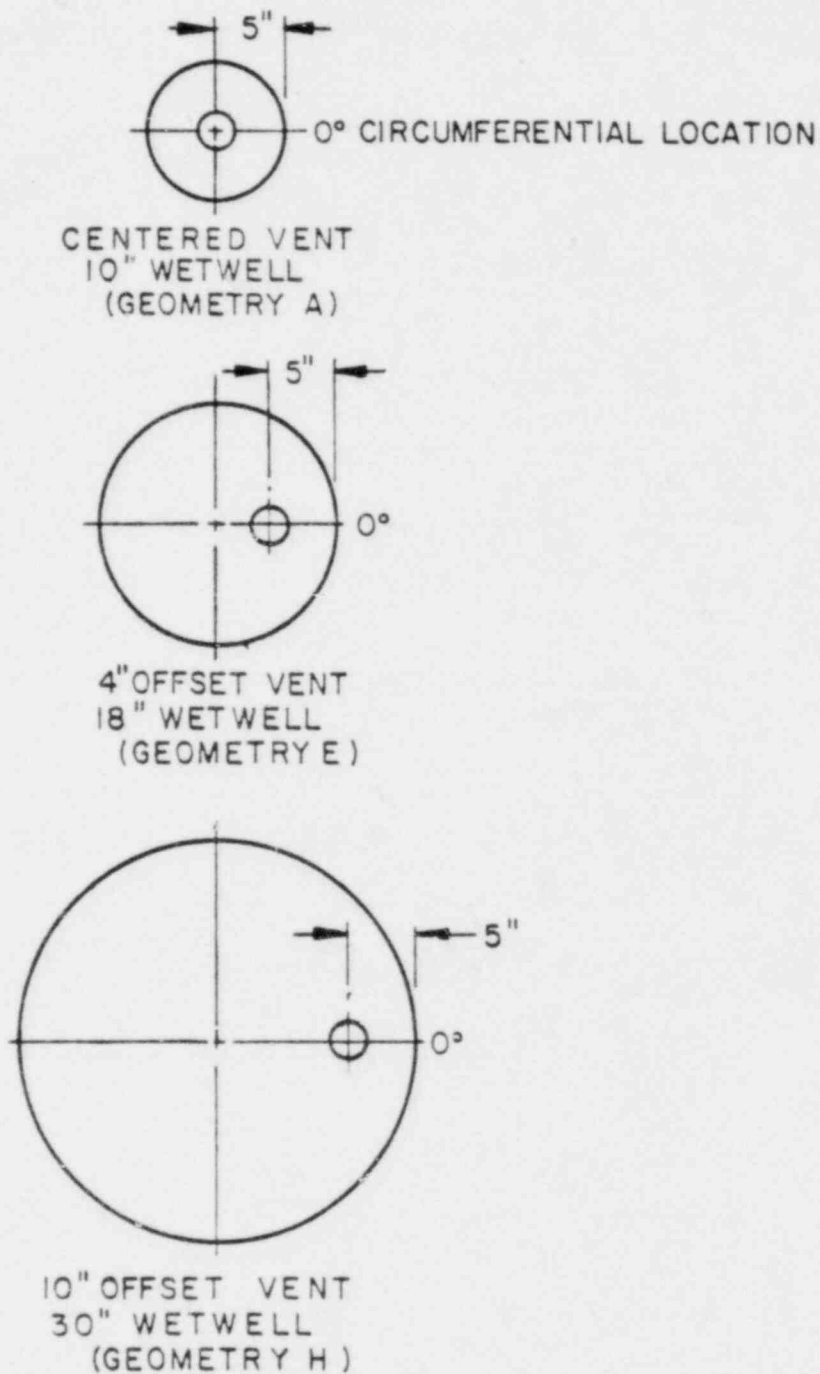   Pressure

5"

0° CIRCUMFERENTIAL LOCATION

CENTERED VENT
10" WETWELL
(GEOMETRY A)

5"

0°

4"OFFSET VENT
18" WETWELL
(GEOMETRY E)

5"

0°

10" OFFSET VENT
30" WETWELL
(GEOMETRY H)

Figure A5-34. Schematic of Equivalent Centered and Offset
Vent Geometries

The following Figures are General Electric Company Proprietary and have been removed from this document in their entirety.

A5-35   Effect of Pool Size on Vent Exit Elevation Pool Wall
         Pressure With the Distance Between Vent and Pool Wall
         Kept Constant

A5-36   Comparison of Mean POPs at Pool Bottom Elevation for the
         Centered Single Vent and Three Vents in the Same Size
         Wetwell, 1/10 Scale Single and Multivent Tests

A5-37a   Computed Pool Bottom Elevation Wall Pressure for the
         1/10 Scale Single Vent Geometry

A5-37b   Computed Pool Bottom Elevation Wall Pressure for the
         1/10 Scale 3 Vent Geometry, All Vents in Phase

A5-37c   Computed Pool Bottom Elevation Wall Pressure for the 1/10
         Scale 7 Vent Geometry, All Vents in Phase

A5-37d   Computed Pool Bottom Elevation Wall Pressure for the 1/10
         Scale 19 Vent Geometry, All Vents in Phase

A5-38a   PSD of Pressure History in Figure A5-37a

A5-38b   PSD of Pressure History in Figure A5-37b

A5-38c   PSD of Pressure History in Figure A5-37c

A5-38d   PSD of Pressure History in Figure A5-37d

A5-39   Multivent Multiplier (Mean POP) at Pool Bottom Elevation,
         1/10 Scale Single and Multivent Tests

A5-40   Multivent Multiplier (Mean Square Power) at Pool Bottom
         Elevation, 1/10 Scale Single and Multivent Tests

A5-41   Computed Pool Bottom Elevation Wall Pressure for the
         1/10 Scale Single Vent Geometry

A5-42   Computed Pool Bottom Elevation Wall Pressure for the
         1/10 ale 3 Vent Geometry

A5-43   Computed Pool Bottom Elevation Wall Pressure for the
         1/10 Scale 7 Vent Geometry

A5-44   Computed Pool Bottom Elevation Wall Pressure for the
         1/10 Scale 19 Vent Geometry

A6. CONCLUSIONS

A significant data base on single and multivent chugging has been obtained
in the Scaled Multivent Test Program. This data base has provided valuable
insights on the chugging phenomenon in single vent and multivent geometries
and has helped in understanding the observed data trends in the full-scale
blowdown tests.

Based on the single vent data obtained at four subscales (1/10, 1/6, 1/4 and
5/12) in this test program and data from full-scale blowdown tests, the
following conclusions were made:

a. Chugging is a complex phenomenon involving several interactive
    processes. The most important process, however, is the rapid con-
    densation at the vent exit that drives the phenomenon. The pool
    wall pressures measured are a superposition of the pool and vent
    responses to the rapid condensation at the vent exit.

b. Of the wide range of system conditions tested (wetwell airspace
    pressure, steam mass flux, pool temperatures, etc)., the prototypical
    system conditions, i.e., full-scale values of wetwell airspace pres-
    sure, steam mass flux, etc., preserve the rapid condensation process
    at the vent exit and the resulting pool response at the various scales.
    Therefore, subscale chugging at prototypical system conditions is
    representative of full-scale chugging.

c. Chugging characteristics are dependent on system conditions. The
    average pool wall pressure amplitudes and period between chugs show
    clear trends with steam mass flux, pool temperature and steam air-
    content which are similar at all four scales tested. Analysis of the
    full-scale blowdown data show that these same trends are also present
    in the full-scale blowdown tests.

The following conclusions were made from the multivent data:

a. The overall chugging phenomenon in multivent geometries is similar to that in single vent geometries and chugging characteristics show the same dependence on system conditions as seen in single vent chugging.

b. The multivent pool wall pressure amplitudes are lower than those in the corresponding single vent geometry at identical system conditions. Also, whereas in the single vent geometry the dominant pool response is at the first axial pool mode, in a multivent geometry, higher circumferential and radial pool modes are excited. Although the power in these higher pool modes is generally quite small.

c. Two major multivent effects were observed in multivent chugging-- the bubble collapses at individual vents are not synchronized and the strength of these bubble collapses varies at individual vents in a multivent geometry. These multivent effects are mainly responsible for the reduced wall pressure amplitudes and the pool response characteristics, i.e., presence of higher pool modes, observed in a multivent geometry.

d. These multivent effects were also found to be present in the full-scale JAERI multivent data. Therefore, it is concluded that multivent pool wall pressure characteristics observed in the subscale tests (lower pool wall pressure amplitudes and pool response characteristics) will also be seen at full-scale.

e. Acoustic models of the multivent pool geometry that include the observed multivent effects are able to predict the multivent pool wall pressure characteristics observed in the test data.

In closing, the data and analyses performed in the Scaled Multivent Test Program have shown that single vent pool wall pressures are bounding, and have provided the understanding of single and multivent chugging necessary for the application of single vent chugging data for evaluation of multivent pool wall loads.

REFERENCES

A1.   Patel, B. R., Dolan, F. X. and Block, J. A., "Comparison of Single and Multivent Chugging at Two Scales," NEDO-24781-1, January 1980.

A2.   Dolan, F. X., Patel, B. R. and Block, J. A., "Comparison of Single and Multivent Chugging - Additional Data," NEDE-25289, April 1980.

A3.   McIntyre, T. R., Ross, M. A. and Myers, L. L., "Mark II - Pressure Suppression Test Program," NEDO-13442-01, June 1976.

A4.   Grafton, W. A., McIntyre, T. R. and Ross, M.A., "Mark II Pressure Suppression Test Program - Phase II and III Tests," NEDO-13468, March 1980.

A5.   Byrd, P. K., et al., "4T Condensation Oscillation Test Program Final Report," NEDO-24811, August 1980.

A6.   Kukita, Y., et al., "Full-Scale Mark II CRT Program," JAERI M-8598, 8665, 8761, 8762, 8763, 8764, 8765; Nov. 1979-Feb. 1980.

A7.   "Chugging Parameteric Test Report - Small Scale," NEDO-21851, June 1978. .

A8.   Clabaugh, W. J., "Scaled Multivent Test Program Plan (Phase 1 Tests)," NEDO-23697A, Rev. 1, January 1979.

A9.   Clabaugh, W. J., "Scaled Multivent Test Program Plan (Phase 2 Tests)," NEDO-23697A, Rev. 1, Supplement 1, September 1979.

A10.   Chan, C. K., et al., "Suppression Pool Dynamics," NUREG-0264-3, June 1977.

A11.   Anderson, W. G., Huber, P. W. and Sonin, A. A., "Small Scale Modeling of Hydrodynamic Forces in Pressure Suppression Systems," NUREG/CR-0003, March 1978.

A12. Lee, C. K. B. and Chan, C. K., "Steam Chugging in Pressure Suppression Containment," NUREG/CR-1552, July 1980.

A13. Andeen, G. B. and Marks, J. S., "Analysis and Testing of Steam Chugging in Pressure Systems," EPRI-NP-908, 1979.

A14. Patel, B. R., Dolan, F. X. and Block, J. A., "CONMAP Tests Experimental Data Report," Creare Report TN-297, June 1979.

A15. This reference was deleted during printing.

A16. Healzer, J. M. "Single Vent Chugging Model, NEDO-23703, September 1977.

A17. Kowalcnuk, W. and Sonin, A. A., "A Model for Condensation Oscillations in a Vertical Pipe Discharging Steam into a Subcooled Water Pool," NUREG/CR-0221, June 1978.

A18. Sargis, D. A., Stuhmiller, J. H., and Wang, S. S., "Analysis of Steam Chugging Phenomena," EPRI NP-908, 1978.

A19. Pitts, J. H., "Steam Chugging in a Boiling Water Reactor Pressure Suppression System," Int. J. Multiphase Flow, Vol. 6, No. 4, August 1980.

A20. "Mark II Improved Chugging Methodology," NEDO-24822, June 1980.

A21. Hinze, J. O., "Turbulence," McGraw Hill, New York, 1959.

A22. Morse, P. M. and Feshback, H., "Methods of Theoretical Physics," Parts 1 and 2, McGraw Hill, New York, 1968.

PART B
EVALUATION OF FLUID-STRUCTURE
INTERACTION EFFECTS IN THE CREARE
MULTIVENT FACILITY

B1.   INTRODUCTION

This Section describes the methods and results from the fluid-structure inter-
action (FSI) evaluation of the Creare multi-vent facility. The evaluation
was undertaken to demonstrate that the eak overpressure associated with
transient pool pressure signals was not being significantly altered by the
test tanks characteristics other than the size of the scaled pool.

The basic method   measured the frequency response of an as-built Creare
tank and calculated the frequency response of a rigid-wall pool of the same
geometry. The measured and calculated frequency responses relate vent
pressure input to bottom pressure output. The frequency responses were used
to compare the predicted peak wall overpressure of the as-built with the
idealized rigid-wall tank under identical vent pressure input.

An analysis of the rigid-wall reference system was performed with a NASTRAN
finite-element model. Fluid pressure was assumed to be governed by the linear
acoustic equation. Analytical modeling of the as-built system was also per-
formed and gave satisfactory agreement with the experiment.

The FSI evaluation concentrated on test and analysis of the Creare 30-in
vessel. This was done because it was judged that the 30-in tank had the
greatest potential for FSI effects. Testing and analysis identical to those
used to evaluate the 30-in tank were also applied to a laboratory tank (A5T),
which was designed to be stiffer than any of those used in the multivent pro-
gram. This was done to verify the experimental and analytical procedures
and also provide a lower bound for the range of FSI effects in the tanks used
to establish the multivent multiplier (MVM). Identification of the range of
FSI effects from the smallest to the largest tank used to establish the MVM
is the most meaningful way to evaluate the potential effects of FSI. It should
be recognized, for example, that if the FSI effects were the same in all tanks,
the MVM would be unaffected by tank structural characteristics.

B2.   FREQUENCY RESPONSE FUNCTIONS

The essence of the FSI evaluation is in the comparison of the actual fluid-
structure system with an idealized reference system. The actual system was
characterized independently by controlled excitation tests, and analysis.
The reference system or idealized rigid-wall tank was characterized by
analysis. The system description in all cases was obtained in the form of
a single-input, complex, frequency response function. This allows system
response for both the actual and reference cases to be calculated and com-
pared for the same input. The reference system is a right circular cylinder
with the diameter and depth of the actual pool, and all wetted surfaces taken
to be rigid. The input for both systems is in the form of a pressure pulse
applied at the vent exit. The output quantity of interest is the acoustic
pressure at the tank bottom outer radius. The peak overpressure at this loca-
tion is the quantity used to define the multivent multiplier.

B2.1   EXPERIMENTAL METHOD

The dynamic characterization of the as-built tank utilized a specially
designed acoustic exciter (Figure B2-1). The exciter consisted of a baffled
piston driven by an electrodynamic shaker. It was designed to operate into a
high acoustic impedance to produce a pressure field which was uniform over the
piston surface. The piston was instrumented to measure both pressure and
acceleration on its face. The device was designed such that with broadband
random input the vent exit to pool bottom transfer function could be
measured with high coherence to 2000 Hz.

The piston was positioned in the 30-in vessel with the piston face submerged
to 20-in. The frequency response was measured using a band-limited Gaussian
random drive signal. Measurements were made with 512 spectral line resolution
over 0-2000 Hz and over 0-500 Hz. The latter measurement was made to accu-
rately resolve the dominant first peak in the frequency response. The
measurement was used to obtain a complex frequency response function.

B2.2 ANALYTICAL METHOD

The frequency response for the rigid-wall tank (equivalent to a cylindrical
acoustic cavity) was computed with a NASTRAN finite-element model. The
model for the 30-in tank utilized 1024 axisymmetric ring elements to repre-
sent the contained fluid. The fluid mesh and the input and output locations
for the NASTRAN model are shown in Figure B2-2. The input was in the form
of a pressure pulse on the simulated piston face, and the output was the time
history of the acoustic pressure response at the tank bottom outer radius.

B2.3 FSI EVALUATION

The comparison of the actual 30-in test tank with the rigid-wall tank was
made by comparing peak wall pressure response values for identical vent
pressure time histories. The basic requirements for the input waveform stipu-
lated that it should have the general form of an impulsive transient (similar
to chugging), and its Fourier transform should have a broad, smooth magnitude
spectrum that covers the frequency range over which response is seen in the
actual chugging test. The test input selected was

$$p_1 (t) = 1/4 \left[1 + \cos \frac{2\pi}{\tau} (t - \frac{\tau}{2}) \right]^2$$

Calculations were performed with a duration τ varying in five discrete steps
from 1.56 to 9.18 milliseconds. The pulse (called a haversine-squared) and
its associated Fourier magnitude spectrum, are shown in Figures B2-3 and
B2-4 for durations of 1.56 milliseconds and 6.05 milliseconds.

The Fourier transform of the output pressure for input $p_1(t)$ was computed from
an equation of the form

$$p_2 (f) = \hat{H}_{12} (f) \, p_1 (f)$$

where p_1 (f) and p_2 (f) are the Fourier transforms of the input and output pressure, and H_{12} (f) denotes the complex frequency response for either the as-built system, or the reference rigid system. The transient response and specifically the peak overpressure are obtained by inversion of H_{p_2} (f).
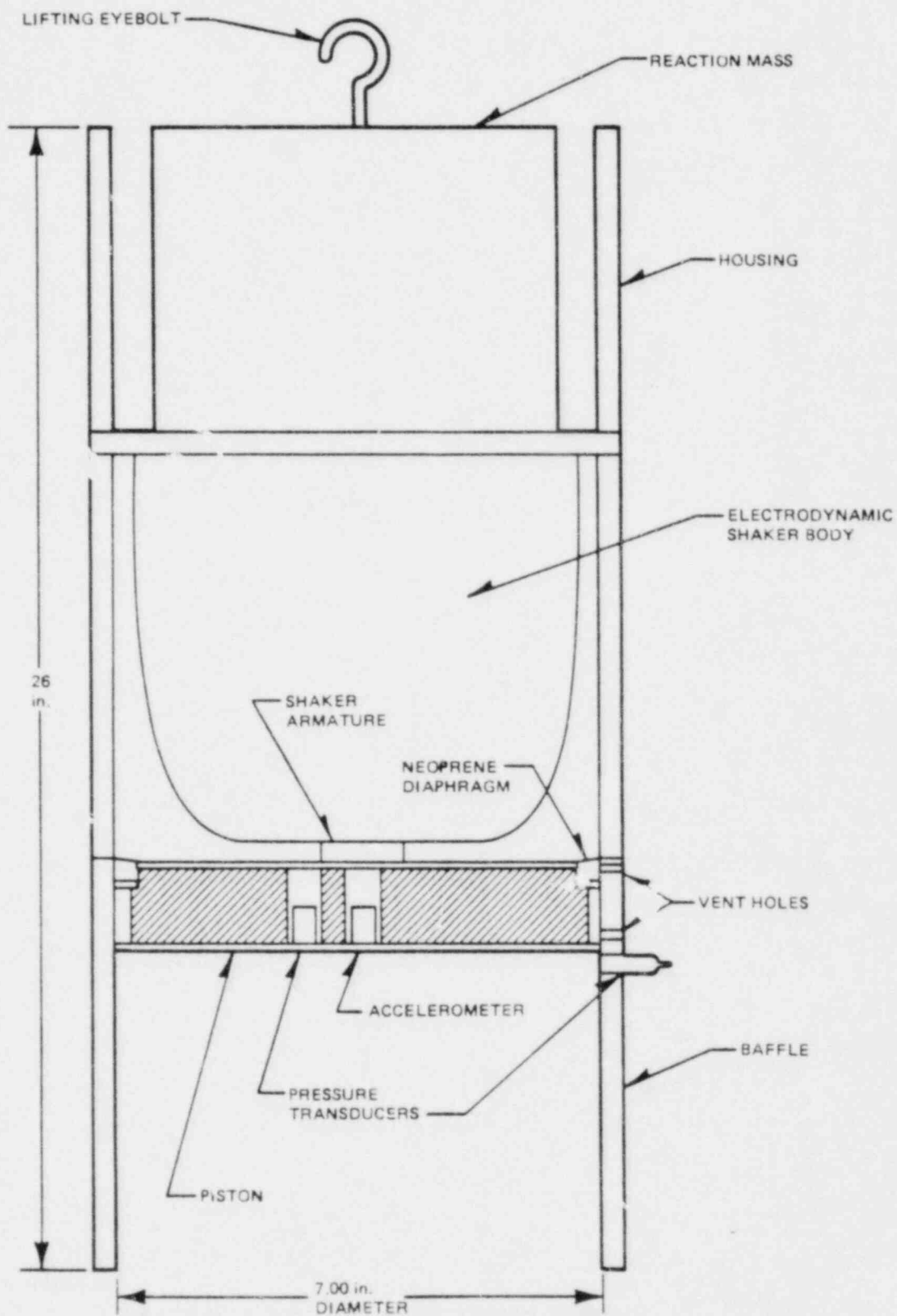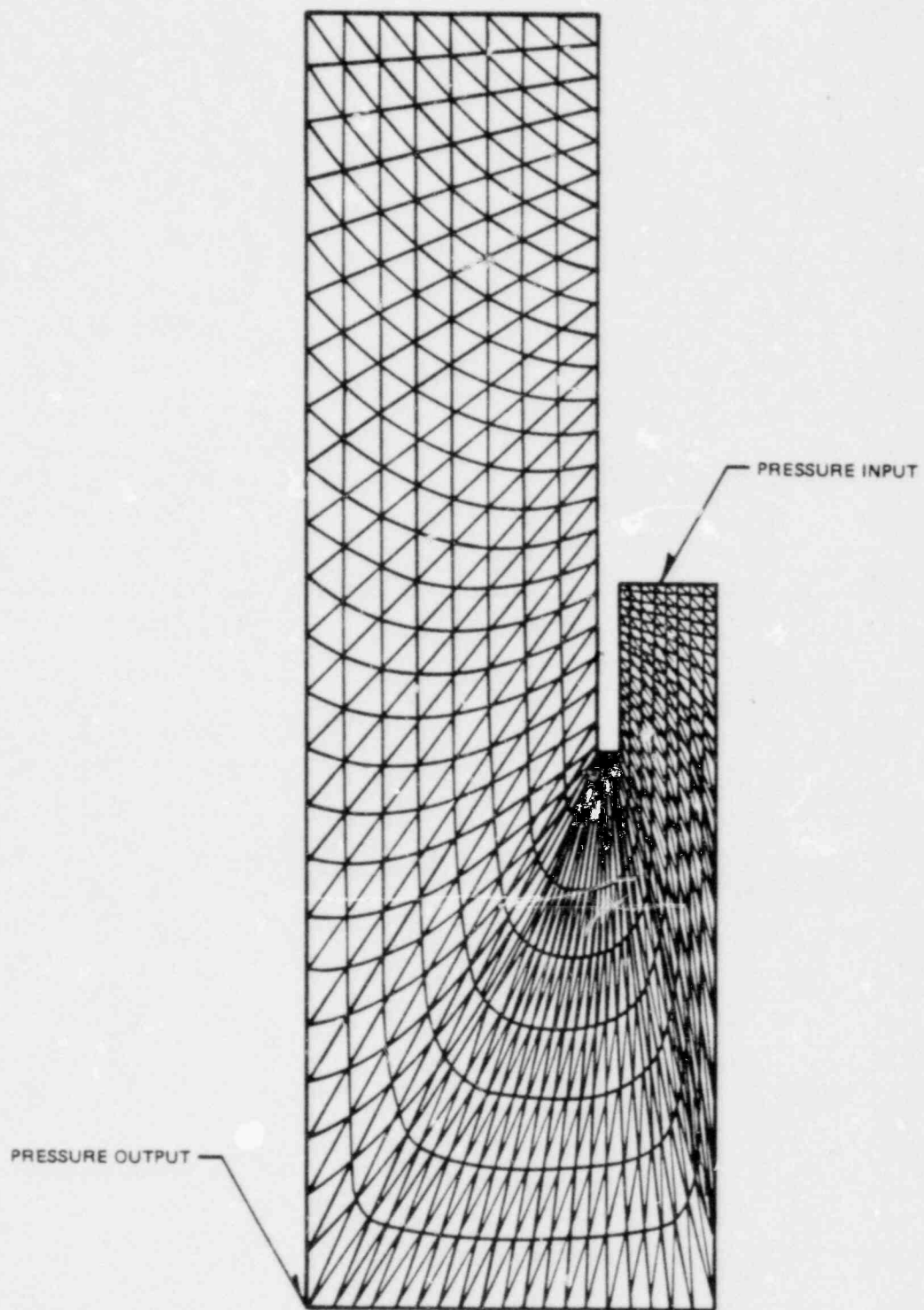
Figure B2-1. Sketch of Acoustic Exciter

PRESSURE INPUT

PRESSURE OUTPUT

Figure B2-2.   Fluid Mesh for NASTRAN Model
of 30-in Acoustic Cavity
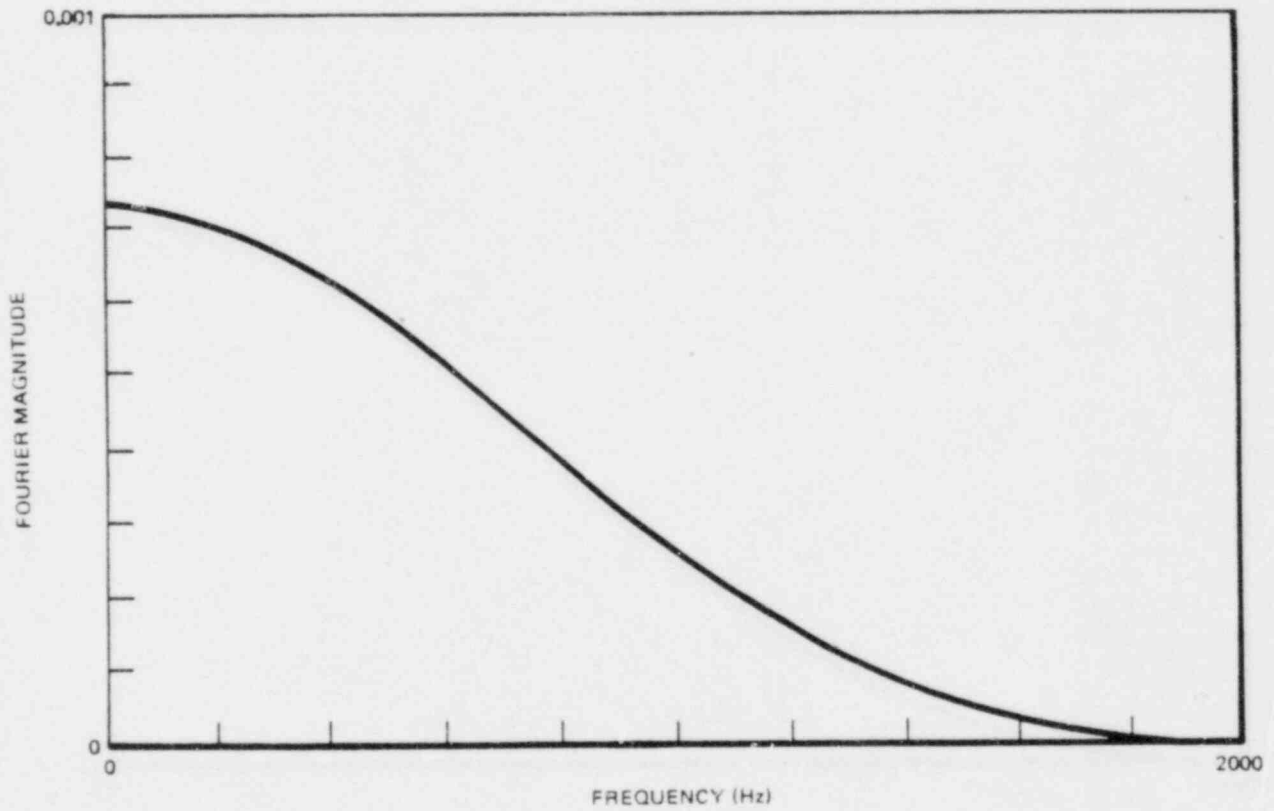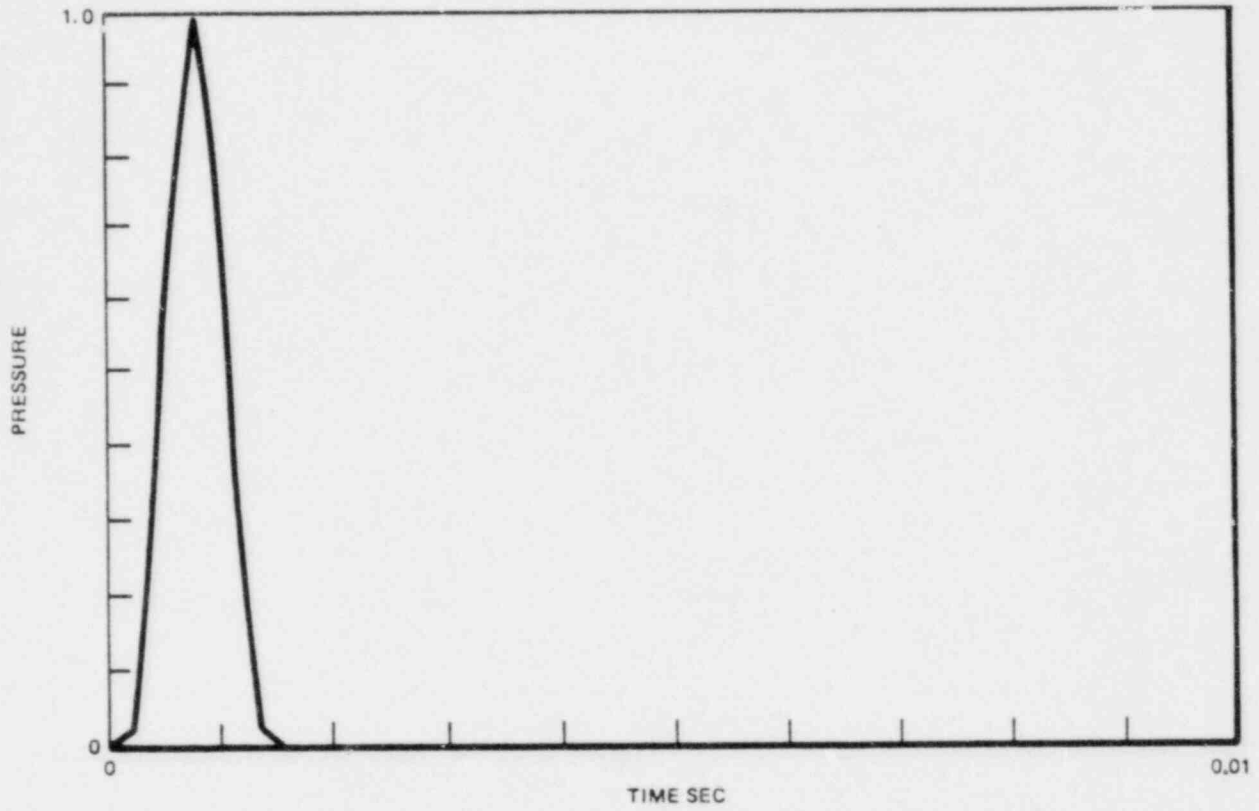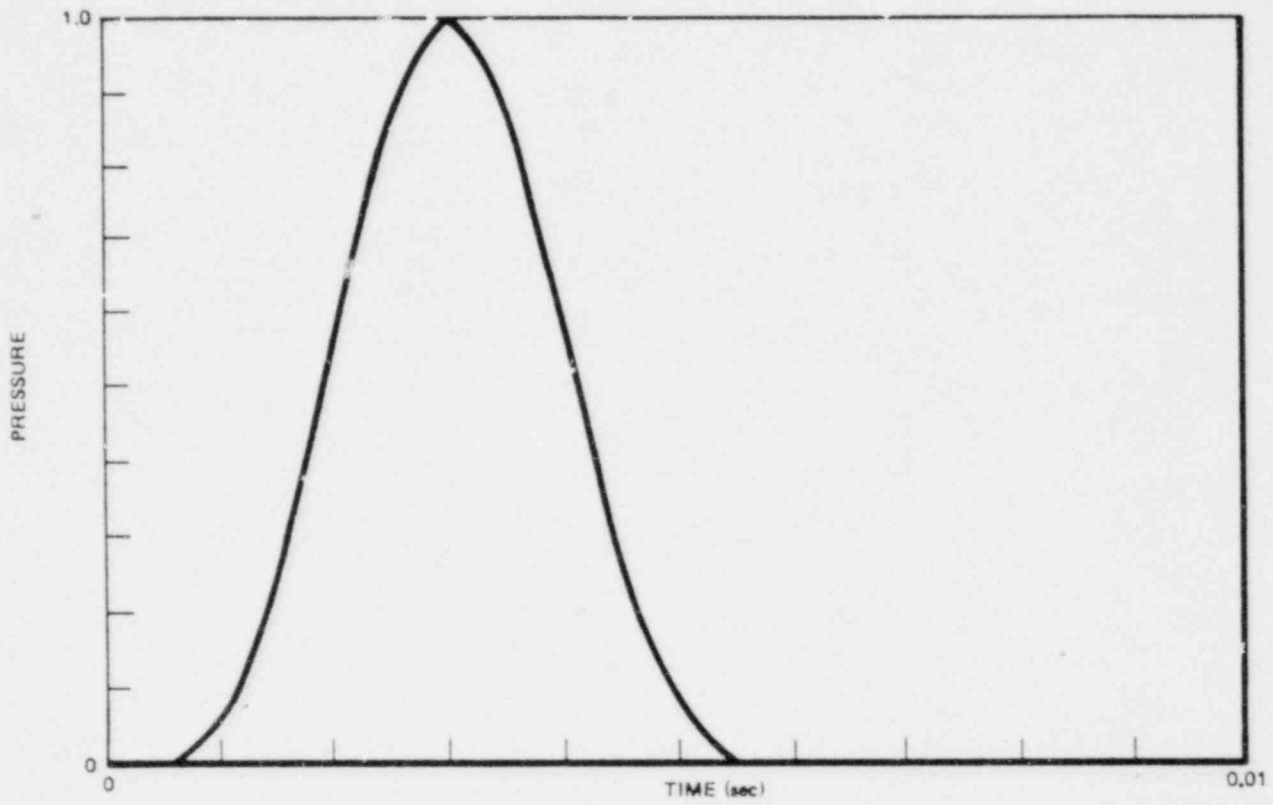
Figure B2-3. 1.56 ms. Haversine Squared Pulse
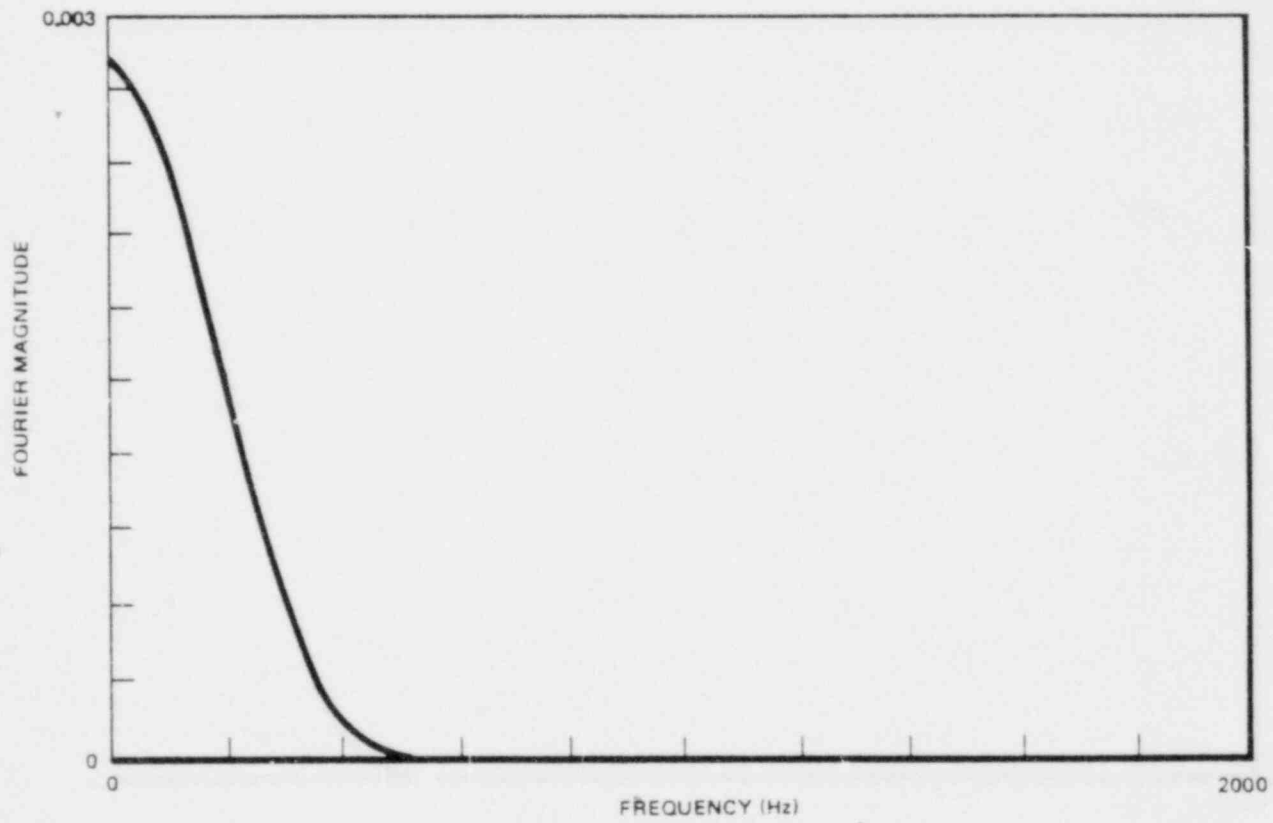
Figure B2-4. 6.05 ms. Haversine-Squared Pulse

B3.   RESULTS AND DISCUSSION

The vent exit to tank bottom frequency response in the 30-in pool calculated with the rigid-wall NASTRAN model is shown in Figure B3-1. The top portion of the figure shows the ratio of bottom pressure amplitude to vent pressure amplitude, and the bottom portion shows the relative phase angle between the output and the input. The peaks in the transfer function correspond to the natural frequencies of the acoustic cavity with the pressure held to zero on the vent exit plane.

The measured transfer function for the 30-in tank is shown in Figure B3-2.

The peak overpressure responses for the two systems are shown as functions of the input pulse width in Table B1.

The ratio of actual to rigid peak overpressure was plotted as a function of the effective cutoff frequency of the input pulse as shown in Figure B3-3.

When evaluating the FSI results the comparison of an actual system to an idealized rigid-wall system, in terms of dynamic response to broadband input, must be understood as being an extremely stringent test. In this problem it is more appropriate to establish the relative FSI effects in the test tanks by comparing the measured effects in the 30-in Creare tank with the same measured effects in the A5T tank. The A5T represents a tank that is more rigid than any of the vessels used in the multivent program. In this way, the range of FSI effects is bounded and the maximum resulting uncertainty in the multivent multiplier due to FSI is established.

Table B1

MEASURED AND CALCULATED PEAK OVERPRESSURE
RESPONSE TO UNIT AMPLITUDE HAVERSINE-SQUARED
INPUT PULSE FOR CREARE 30 IN. TANK

Pulse Width (ms.)
Cutoff Freq. (Hz.)

Source

Creare 30-in. Rigid
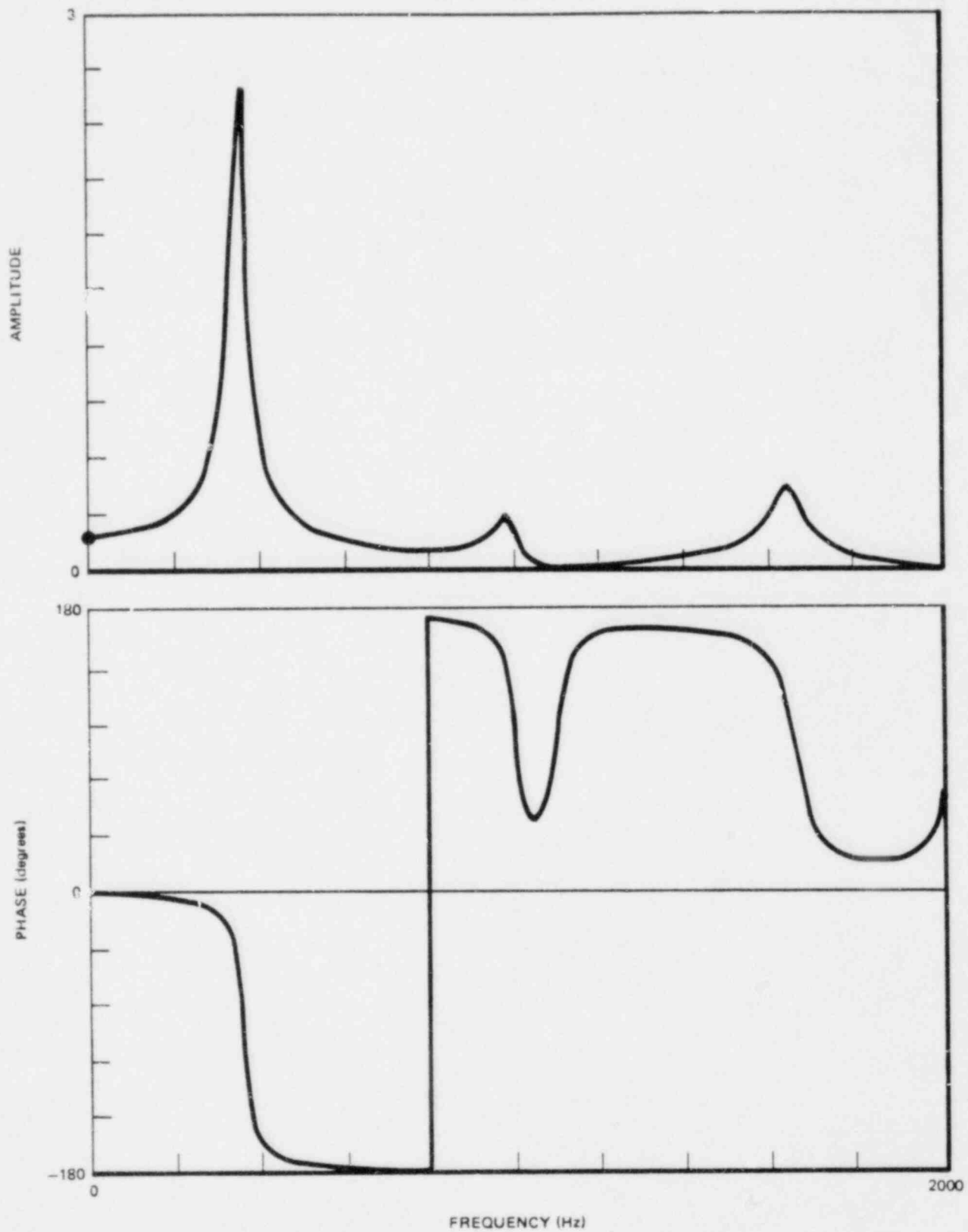
Creare 30-in. Measured

Figure B3-1. Frequency Response for Rigid 30-in. Cylindrical
Acoustic Cavity

The following Figures are General Electric Company Proprietary
and have been removed from this document in their entirety.

Section B4 "Conclusions" is General Electric Company Proprietary and has been removed from this document in its entirety.